High Pulse Energy Near-Infrared Ultrafast Optical Parametric Oscillators

MSc Tobias Paul Lamour (né Müller)

Submitted for the degree of Doctor of Philosophy

Heriot-Watt University

School of Engineering and Physical Science

December 2011

ABSTRACT

A source-demand in the near- and mid-IR wavelength spectrum exists for various applications such as waveguide inscription, multiphoton imaging, and nonlinear spectroscopy. All of the applications seek for higher repetitions rates for faster processing speed, better signal to noise ratios or to improve the results for applications like laser waveguide inscription. This is in contrast to the high pulse energies, required to drive the nonlinear processes involved with these applications. Available systems are either based on low-energy, high-repetition-rate optical parametric oscillators or high-energy, low-repetition-rate optical parametric amplifiers. In this thesis a sources was developed that can bridge the wide gap between these two extremes, providing sufficient energy to drive nonlinear processes, with repetition rates in the MHz domain.

This was achieved by introducing three techniques previously employed for energy scaling in laser cavities. Firstly an exchange from the conventionally used Ti:sapphire pump to a commercial high power Yb:fibre laser system readily scaled the usable pump energy. This was combined with a technique known as cavity-length extension, which allows a lowering of the cavity roundtrip time offering the build-up of pulses with increased energy. In a final stage, cavity-dumping on basis of an acousto-optic modulator was introduced into the a redesigned cavity. The combination of these three techniques, novel to synchronously pumped optical parametric oscillators, enabled the extraction of record-high pulse energies and peak powers.

DEDICATION

For my wife Aline and our son Liam!

ACKNOWLEDGEMENT

This work would have been impossible without the generous and patient support of so many people. Therefore, I am going to use this space to dedicate my gratitude. This is for:

Professor Derryck Reid, my supervisor; the mastermind who guided me day in, day out. You are a profuse and never ending source of ultrafast and nonlinear wisdom. The way you introduced me into the ultrafast world mesmerized me and drew me into a great adventure that I never could have imagined. You are the broad-minded figure with the great gift of unlimited patience behind all this. Derryck, where I come from, a PhD supervisor is called a 'Doctor Father' and I had the extraordinary fortune to exactly experience why a PhD's supervisor is called a Doctor Father. Beyond your professional mentoring, I would like to thank you and your wife Nicola for the warmth and generous support you have shown to my family and me.

My beloved wife Aline who held my hand through countless valleys full of desperation, moroseness, and exhaustion. I am very grateful that you are still with me and that you on top of all gave birth to our greatest gift Liam. I will never forget that you were there, putting your needs aside when I needed support.

To Professor Ajoy Kar who supported me as my second supervisor. I am thankful for all your help and support during the three and a half years. Your humour and warmth was very much appreciated.

My parents for their endless support, which goes far beyond what I could expect. It is comforting to have an open door whatever may be and it has been always nice and warm to come home.

Beyond this support, I had the preference to get to know several brilliant colleagues who have accompanied me along my way. Foremost are the current and previous members of the Ultrafast Optics Group: Dr Christopher Leburn, Dr Jinghua Sun, Teresa Ferreiro, Richard McCracken, Dr Zhaowei Zhang, Cristtel Ramirez, Thomas Schratwieser, Dr Carl Farrell, Dr Keith Serrels, Dr Lukasz Kornaszewski and Dr Euan

Ramsay. Alongside the group members, there were a handful of very special people I would like to thank. Those are Dr Ian Thompson, Stephen Beecher, Dr Reiner Beck, and Dr Christopher Kuklewicz. You all have been outstanding supportive, be it in the lab, while borrowing equipment, getting a hand while setting things up or through countless discussions where crucial and valuable knowledge was exchanged. Working with you has been extraordinary and I would like to thank you all for your time and support.

Beyond this, a very special thanks goes to Christopher and Ruth Leburn who were unbelievable generous and supportive during the last year. I hope we can find numerous occasions to return all the favours in the coming years and we can foster the friendship between our families for a very long time.

Euan Ramsay deserves a thank you for his warmth and wisdom at all times. I have learned a lot from you and I still look up to your enthusiasm you put into the physics teaching labs and I will never forget the presentation exercise in the hotel room in San Jose where you helped me to survive during CLEO'10.

Very important are the people in the workshop (Mark, Peter, Ian, Tony) without whom nothing in the lab would have happen and the secretaries (Janice, Alex, Linda, Sheila) who were always concerned about all my needs.

My external examiner Professor David Shepherd and internal examiner Dr Robert Thomson receive my grateful acknowledgment for their time they spend correcting my thesis as well as being extremely supportive and flexible during a tense period of submission and the viva preparation.

My sincere thanks to all of you!

ACADEMIC REGISTRY

Research Thesis Submission Form

Name:	Tobias Paul Lamour		
School/PGI:	School of Engineering and Physical Science		
Version: (*i.e. First, Resubmission, Final*)	Final	Degree Sought (*Award **and** Subject area*)	Doctor of Philosophy in Laser Physics

Declaration

In accordance with the appropriate regulations, I hereby submit my thesis and I declare that:

1) the thesis embodies the results of my own work and has been composed by myself.
2) where appropriate, I have made acknowledgement of the work of others and have made reference to work carried out in collaboration with other persons.
3) the thesis is the correct version of the thesis for submission and is the same version as any electronic versions submitted*.
4) my thesis for the award referred to, deposited in the Heriot-Watt University Library, should be made available for loan or photocopying and be available via the Institutional Repository, subject to such conditions as the Librarian may require.
5) I understand that as a student of the University I am required to abide by the Regulations of the University and to conform to its discipline.

* Please note that it is the responsibility of the candidate to ensure that the correct version of the thesis is submitted.

Signature of Candidate:		Date:	

Submission

Submitted By (*name in capitals*):	Tobias P Lamour
Signature of Individual Submitting:	
Date Submitted:	

For Completion in the Student Service Centre (SSC)

Received in the SSC by (*name in capitals*):			
Method of Submission (*Handed in to SSC; posted through internal/external mail*):			
E-thesis Submitted (***mandatory for final theses***):			
Signature:		Date:	

Table of Contents

LISTS OF FIGURES

LISTS OF TABLES

LISTS OF PUBLICATIONS BY THE CANDIDATE

Peer reviewed journal publication:

1. **T. P. Lamour** and D. Reid, "650-nJ pulses from a cavity-dumped Yb: fiber-pumped ultrafast optical parametric oscillator.," Optics Express **19**, 17557-62 (2011).

2. D. T. Reid, J. Sun, **T. P. Lamour** and T. Ferreiro, "Advances in ultrafast optical parametric oscillators", Laser Physics Letters, **8**, 8–15 (2011).

3. **T. P. Lamour**, J. Sun, and D. T. Reid, "Wavelength stabilization of a synchronously pumped optical parametric oscillator: Optimizing proportional-integral control", Review of Scientific Instruments **81**, 053101 (2010).

4. **T. P. Lamour**, L. Kornaszewski, J. H. Sun and D. T. Reid, "Yb:fiber-laser-pumped high-energy picosecond optical parametric oscillator", Optics Express **17** 14229 (2009).

Conference submissions:

1. **T. P. Lamour** and D. T. Reid, "650-nJ pulses from a cavity-dumped Yb: fiber-pumped ultrafast optical parametric oscillator," The European Conference on Lasers and Electro-Optics (2011).

2. **T. P. Lamour**, J. H. Sun and D. T. Reid, "High-pulse-energy cavity-dumped optical parametric oscillator in the near- and mid-infrared", presented at the International Summer School in Ultrafast Nonlinear Optics, SUSSP 66, Edinburgh, Scotland, (2010).

3. **T. P. Lamour**, J. Sun and D. T. Reid., "Proportional-integral control for wavelength stabilization of a synchronously-pumped optical parametric oscillator", Conference on Lasers and Electro-Optics (2010).

4. L. Kornaszewski, **T. P. Lamour**, J. Sun and D. T. Reid, "High-pulse-energy optical parametric oscillator in the near- and mid-infrared", Conference on Lasers and Electro-Optics (2009).

5. **T. P. Lamour**, J. Sun and D. T. Reid, "High-Pulse-Energy Optical Parametric Oscillator", Mini-Symposium on Ultrashort Pulse Sources, The Rank Prize Funds, UK, 17- 20 August (2009) (INVITED).

6. D. T. Reid, L. W. Kornaszewski, **T. P. Müller**, N. Gayraud, W. N. MacPherson, D. P. Hand, J. M. Stone, and J. C. Knight, "Ultrafast optical parametric oscillators for spectroscopy," Society of Photo-Optical Instrumentation Engineers (SPIE) Conference Series **7193**, 719325 (2009).

Patents:

1. U.S. Patent Application No. US20100790000, Publication No.US2010328761 (A1) (published Dec. 30, 2010)(Heriot-Watt University, D. T. Reid, L. Kornaszewski, **T. P. Lamour**, applicants).

2. G.B. Patent Application No. WO2010GB01047, Publication No.WO2010136761 (A1) (published Dec. 02, 2010)(Heriot-Watt University, D. T. Reid, L. Kornaszewski, **T. P. Lamour**, applicants).

Chapter 1 - Introduction

1.1 Introduction

High-energy ultrafast infrared (1.5 - 4.0μm) laser sources are needed for optical waveguide writing, free-space spectroscopy for environmental monitoring and chemical detection, 3D ranging, multiphoton imaging, nonlinear spectroscopy, and in various medical applications. Reported systems are either based on low-energy, high-repetition-rate optical parametric oscillators (OPOs) or high-energy, low-repetition-rate optical parametric amplifiers (OPAs). A demand exists for sources that can bridge the wide technology gap between these two extremes, providing sufficient energy to drive nonlinear processes, but delivering pulses at the high repetition rates that improve processing speed, signal-to-noise ratio, waveguide quality and more. The aim of this thesis is to overcome the existing limitations experienced associated with synchronously pumped ultrafast OPOs by demonstrating an increase in pulse energy over existing ultrafast OPOs by two to three orders of magnitude, while providing a scientifically and commercially attractive solution with the potential to fill the existing gap.

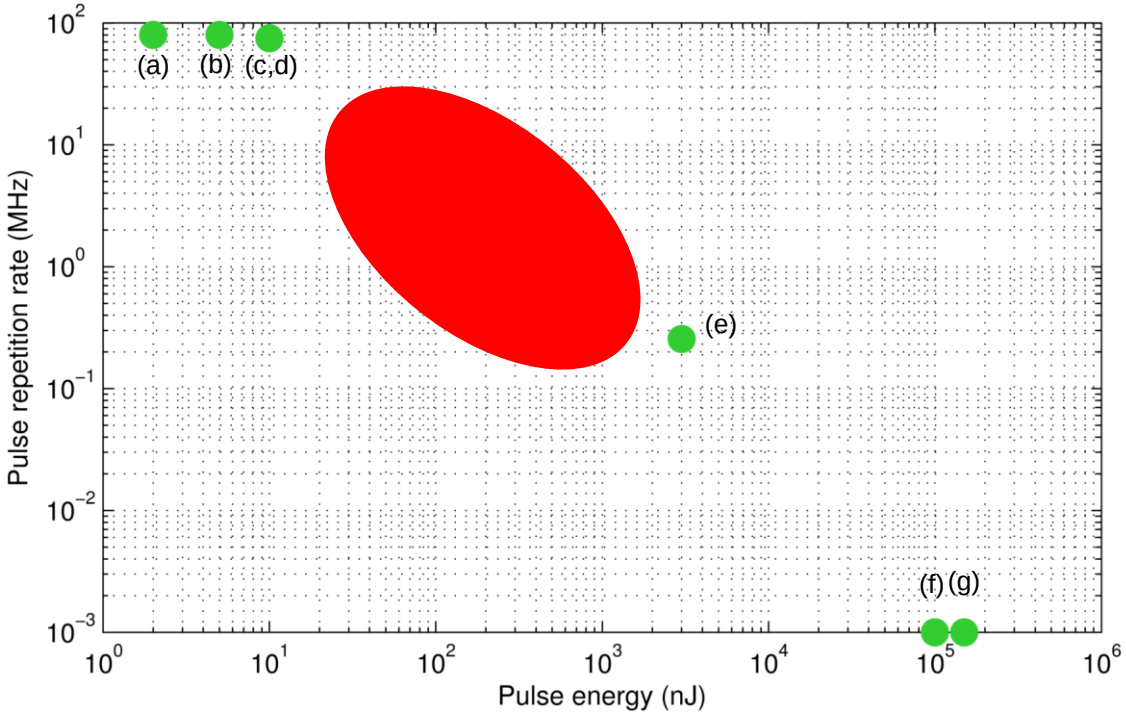

Figure 1.1. Shows the existing gap between low-energy, high-repetition-rate OPOs and high-energy, low-repetition-rate optical parametric amplifiers OPAs. The green markers correspond to: (a) [1], (b) [2], (c) [3], (d) [4], (e) [5], (f) [6], (g) [7]. The red area shows the gap this project intended to fill.

In Figure 1.1 the existing gap of available intermediate pulse energies in the region of 1 to 10 MHz is indicated as a red area. The green markers indicated available systems which are separated into the two extremes. The references are provided in the figure caption. This thesis addresses an uncovered region within ultrashort-pulse lasers, represented by a performance gap ranging over two orders of magnitudes in the repetition rate and pulse energy domain. In chapter three, we describe a novel energy-scaling concept that allowed us to generate 72 nJ pulses directly from a high-repetition-rate (15.3 MHz) ultrafast OPO. This result exceeds the performance of current OPO systems by one to two orders-of-magnitude. By combining this novel system with a further energy-scaling technique, we demonstrate a factor of up to 500 in energy increase from a synchronously-pumped ultrafast OPO, corresponding to the generation of MHz-repetition-rate, 650 nJ energy pulses in the 1.5 µm band. The remarkable increase in energies, repetition rates and tunability addresses in a single system the needs of applications such as nonlinear spectroscopy and optical waveguide writing, which are optimised at pulse energies exceeding those of ultrafast OPOs but at pulse repetition frequencies above those from ultrafast OPAs.

The demonstrated performance represents a new class of OPOs with unprecedented capabilities, combining highly flexible repetition rates, pulse energy and the potential to cover a wavelength range in the near to mid IR from 1.5 µm to 4 µm. This offers scientists in other areas a versatile tool which can provide better sensitivity, higher throughput, as well as to address entirely new experiments which were not accessible due to the required pulse energy necessary in nonlinear applications.

1.2 Energy-scaling strategies

In this thesis, three separate energy-scaling strategies will be introduced which were required to achieve the desired performance improvement. A summary of each of the three schemes, which were combined in the OPO resonator, is described in the following subsections.

1.2.1 Pump power scaling

Pump power scaling was only reported once where a home-build thin-disc laser was used to pump a fibre-feedback OPO [8]. Most OPOs are pumped by Ti:sapphire lasers which are limited to average powers <3 W. Higher energies were immediately available by substituting Ti:sapphire with an ultrafast Yb:fibre laser, delivering up to 10 W with pulse energies of >400 nJ. This approach increased the energy over conventional OPO systems by a factor of 10.

1.2.2 Cavity length extension via relay-imaging

This is the main novelty of the presented systems in which by increasing the pulse roundtrip time, the pulse energy is increased for a fixed average output power. Relay imaging based on 4f mirror system preserves the cavity stability but extends its length. Although relay imaging is previously known as a method for scaling the cavity length of modelocked laser oscillators, it has not before been applied to synchronously pumped OPOs. By employing an Yb-based master oscillator fiber amplifier with a 15 MHz roundtrip frequency and synchronous pumping provided a 20 to 30 fold increase in energy over previous systems. A different technique for extending the cavity-length in OPOs is available through a technique known as fibre-feedback where a OPO cavity feedback path is passed partially through a fibre [8,9].

1.2.3 Cavity dumping using a high-finesse cavity

The combination of cavity-dumping with relay-imaging is another key innovative step, and represents the main extension of the earlier presented research. A high-finesse relay-imaged cavity exhibits very high intracavity energies. Cavity-dumping using an AOM provides direct access to these pulses, at a dumping frequency around 10 - 150 times lower than the cavity roundtrip frequency. With the cavity-dumped OPO configured in a way that allowed efficient oscillation at the shorter signal wavelength the full energy scaling potential was used to access the resonant near-infrared pulses with the highest energy. This allowed us the extraction of pulse energies exceeding the highest reported energies from an OPO [8] by almost a factor of two.

1.3 Former reports of cavity-dumped OPOs

Cavity dumping is employed to extract individual pulses with much higher energies at a sub-harmonic of the fundamental laser repetition rate, at the expense of average power and repetition rate, where usually the cavity is operated in a low-loss regime allowing a build-up of very high intracavity powers.

Despite the broad implementation in many different laser systems, cavity dumping of OPOs was previously only reported for two systems. The first cavity-dumped OPO was reported by Potma in 1998 [10], delivering 13 nJ at a wavelength of 630 nm and a dumping rate of 400 kHz. In 2005, Min and Joo reported an OPO based on a PPLN-crystal, which was pumped with 9.8 nJ pulses and were able to extract pulse with up to 90 nJ [11] at a wavelength of 1.2 µm.

For OPOs, cavity dumping has great potential because it offers pulse energies that are an order of magnitude higher than available with conventional output-coupling and still provides a broad tuning range, for instance from 1.0 to 1.5 µm [11].

1.4 Applications of ultrafast optical pulses in the MID-IR

This new operating regime opens domains previously not addressable with OPOs within semiconductor research, chemistry, metrology, biological imaging, direct laser waveguide writing, spectroscopy, THz generation, and other research applications. The examples below highlight the need for sources entering the performance gap identified earlier.

In ultrafast laser waveguide inscription, high pulse repetition-rates reduce the modification threshold and improve waveguide quality [12], but no suitable sources exist beyond 1040 nm, despite genuine demand.

Nonlinear spectroscopy like CARS, 2D spectroscopy, Raman spectroscopy and others require high- energy IR pulses to generate a signal, while requireing high repetition rates to enable rapid, low-noise measurements [13].

Multi-photon imaging cover techniques such as video-rate imaging require high repetition rates. IR pulses give better tissue penetration, lower scattering, and less photo-chemical damage. High pulse energies give the same nonlinear signal at lower average powers, reducing the thermal load on samples, which is challenging scientists who study sensitive cells and other organisms in the domain of nonlinear bio-microscopy.

The broad bandwidth and spatial coherence of the system directly enables remote sensing and IR spectroscopy over long distances, useful for explosives sensing and environmental monitoring. With high energies in the atmospheric transmission bands at 1.5, 3.8 and 4.2 μm, the system has potential applications in active hyper-spectral imaging.

1.5 Conclusions

The core motivation to access the existing performance gap was introduced. This was followed by a short introduction of the key schemes and techniques used to achieve the results subject in the thesis. Several possible application areas were identified in which the demonstrated system could readily be employed, and offer the potential to address novel experiments due to the performance increase. In Chapter 2 the fundamental physics behind the processes is presented to the reader. In Chapter 3, the first two energy-scaling techniques, followed by their characterisation and discussion are introduced. A detailed implementation and the involved numerical optimisation of the wavelength-locking scheme for OPO cavity stabilisation is introduced in Chapter 4. Combining the results of Chapter 3 and Chapter 4 with a re-design of the existing cavity to comprise a cavity-dumper is the subject to Chapter 5, leading to the extraction of the highest reported pulse energy and peak power reported for a synchronously pumped ultrafast OPO to date. In Chapter 6 the very recently formulated nonlinear envelope equation is used to study numerically the dynamics of cavity-dumped OPOs. The

obtained results are presented and their general indications are discussed to support improvements for a next-generation cavity dumped OPO design.

Chapter 2 - Fundamentals of ultrafast optical parametric oscillators

2.1 Introduction

Starting with the basic principles of nonlinear optics, fundamental concepts and processes are explained which are essential to the operation of an ultrafast optical parametric oscillator as well as to understand results discussed in the following chapters. The reader is provided with a brief introduction into nonlinear optics, concentrating on $\chi^{(2)}$ processes. Phasematching conditions and parametric amplification are covered, and the propagation of ultrafast pulses and their temporal and spectral shaping through dispersion is explained. The last part of the chapter introduces the concept of self-phase modulation, as well as interferometric autocorrelation as a method to characterise the temporal shape of pulses experimentally.

2.2 Basic principles of nonlinear optics

When light is propagating in a medium other than vacuum, its electric field causes an electric polarization of the medium. The electric polarization sensitivity of a medium in proportion to an applied electric field is the electric susceptibility χ_e. In the case where a field of typical electric strength (e.g. incandescent light bulb or an unfocused low power laser beam) is present, the electric polarization $P(\omega)$ depends linearly on the electric field strength $E(\omega)$ expressed as

$$P(\omega) = \epsilon_0 \chi^{(1)} E(\omega)\,, \qquad 2.1$$

where $\chi^{(1)}$ is known as the linear susceptibility and ϵ_0 the vacuum permittivity. With the presence of highly intense fields, predominantly the case in ultrafast systems, a nonlinear polarization of the medium takes place, which is often described by extending equation 2.1 into a power series [14] as

$$P(\omega) = \epsilon_0\chi^{(1)}E(\omega) + \epsilon_0\chi^{(2)}E^2(\omega) + \epsilon_0\chi^{(3)}E^3(\omega)+\dots\ , \qquad 2.2$$

where $\chi^{(2)}$ and $\chi^{(3)}$ are measures of the second-order and the third-order nonlinear optical susceptibilities respectively.

The real and imaginary parts of each of the susceptibilities deal with different physical effects and can be generally separated by the equation

$$\chi^{(n)} = \chi^{(n)\prime} - i\chi^{(n)\prime\prime}\ . \qquad 2.3$$

The real part of the linear susceptibility $\chi^{(1)\prime}$ is associated with the frequency dependent linear refractive index by

$$n_0(\omega) = \sqrt{1 + Re\{\chi^{(1)}\}}\,, \qquad 2.4$$

also linked to linear dispersion and birefringence. The imaginary part of the linear susceptibility $-i\chi^{(1)\prime\prime}$ describes the dissipative effect of linear absorption of photon energy by the medium and the re-emission (gain) at longer wavelengths.

The real part of the second-order nonlinear susceptibility $\chi^{(2)\prime}$ is linked to frequency interactions such as three-wave mixing (second-harmonic generation (SHG), sum- and difference-frequency generation (SFG and DFG), and parametric oscillation and amplification), as well as optical rectification and the electro-optic effect while the imaginary part $-i\chi^{(2)\prime\prime}$ is zero, meaning that $\chi^{(2)}$ processes do not show any photon energy absorption in the interacting medium.

$\chi^{(3)\prime}$, the real part of the third-order nonlinear susceptibility is connected to four-wave mixing (third-harmonic generation (THG) and frequency conversion) and the Kerr effect (self-focusing, self-phase modulation, cross-phase modulation). Nonlinear effects where a photon-to-medium energy exchange takes place are associated with the

imaginary part of the third-order nonlinearity $-i\chi^{(3)\prime\prime}$, and are responsible for Raman scattering, Brillouin-scattering, and multi-photon absorption processes.

2.2.1 The nonlinear optical susceptibility $\chi^{(2)}$ and its properties

The fact that all $\chi^{(2)}$ nonlinear interactions involve only phase interactions between the optical fields, with no energy dissipation in the medium, makes this nonlinear process particular appealing because it can reach high efficiency and requires no cooling, necessary for classical laser gain materials or high-power Raman systems. Consequently, $\chi^{(2)}$ nonlinear interactions processes are power-scalable, limited only by the damage-threshold and photo-refraction (a statistical process where impurity electrons are photo-excited into the conduction band with the tendency to diffuse into the less exposed zones, resulting in locally positively charged holes and a negatively charged surrounding resulting in localised change in the refractive index due to the electro-optic effect), determined by the material properties of a specific nonlinear crystal.

All transparent materials exhibit linear and third-order nonlinearity, while second-order $\chi^{(2)}$ effects can only be observed in non-centrosymmetric crystals. This can be explained with a simple example: If a crystal possesses a symmetric lattice structure, any oscillating electric field applied to it causes an equal polarisation for the positive and the negative amplitude parts, leaving a zero net contribution to the quadratic term in equation 2.2.

2.2.2 A qualitative description of nonlinear optical processes

Based on the previously introduced second-order nonlinearity a qualitative description of the range of nonlinear optical phenomena that can occur is provided in the following section. The origin of frequency mixing from a second-harmonic polarisation response lies in the quadratic nature of the effect. Let us assume that two waves given in the form

$$E = E_1\, cos(\omega_1 t) + E_2\, cos(\omega_2 t)\,, \tag{2.5}$$

building an interfering field E acting on a material with the response defined by the linear and quadratic term of equation 2.2

$$P = \epsilon_0 \chi^{(1)} E + \epsilon_0 \chi^{(2)} E^2. \tag{2.6}$$

This leads to a polarisation response of,

$$\begin{aligned} P = \epsilon_0 \chi^{(1)} [E_1 \cos(\omega_1 t) + E_2 \cos(\omega_2 t)] \\ + \epsilon_0 \chi^{(2)} [2E_1 E_2 \cos(\omega_1 t) \cos(\omega_2 t) \\ + E_1^2 \cos^2(\omega_1 t) + E_2^2 \cos^2(\omega_2 t)]. \end{aligned} \tag{2.7}$$

By taking advantage of the trigonometric identity, $\cos(\mathrm{x} \pm \mathrm{y}) = \cos(\mathrm{x})\cos(\mathrm{y}) \mp \sin(\mathrm{x})\sin(\mathrm{y})$ it is possible to simplify equation 2.7 and separate the following terms [15],

$$P = \epsilon_0 \chi^{(1)} [\mathrm{E}_1 \cos(\omega_1 t) + E_2 \cos(\omega_2 t)] \tag{2.8}$$

$$+\epsilon_0 \chi^{(2)} E_1 E_2 \cos(\omega_1 + \omega_2)\mathrm{t} \quad (\mathrm{SFG}) \tag{2.9}$$

$$+\epsilon_0 \chi^{(2)} E_1 E_2 \cos(\omega_1 - \omega_2) t \quad (\mathrm{DFG}) \tag{2.10}$$

$$+\frac{1}{2}\epsilon_0 \chi^{(2)} E_1^2 \cos(2\omega_1 t) \quad (\mathrm{SHG}) \tag{2.11}$$

$$+\frac{1}{2}\epsilon_0 \chi^{(2)} E_2^2 \cos(2\omega_2 t) \quad (\mathrm{SHG}) \tag{2.12}$$

$$+\frac{1}{2}\epsilon_0 \chi^{(2)} E_1^2 + \frac{1}{2}\epsilon_0 \chi^{(2)} E_2^2 \quad (\mathrm{EOR})\,. \tag{2.13}$$

The expression in 2.8 represents the linear polarisation response, analogous to the incident interference field. Parts 2.9 and 2.10 correspond to the sum-frequency generation and the difference-frequency generation respectively, while 2.11 and 2.12 are the polarisations for the second harmonic interactions for each of the incident frequencies ω_1 and ω_2. Part 2.13 represents a DC-polarization term known as electro-optical rectification (EOR) which is the inverse process of the electro-optic effect [14].

2.2.3 Coupled wave equations

After the introduction of the nonlinear polarization response of the medium to an intense field, acting as the source of new frequency components we can now apply Maxwell's equations to describe the generation of these new components of the electromagnetic field. This allows one to show how the interacting frequency fields become coupled by the nonlinear interaction and what conditions are required to make it efficient. An extension of the standard wave equation is necessary to address the additional second-order nonlinear polarisation and can be expressed by [14]

$$\nabla^2 E - \frac{1}{c^2}\frac{\partial^2 E}{\partial t^2} = \frac{1}{\epsilon_0 c^2}\frac{\partial^2 P}{\partial t^2}, \qquad 2.14$$

The derivation of the wave equations is elaborated even with the consideration limited to three frequencies $\omega_1, \omega_2, \omega_3$, and the propagation direction to z. The solution [14,15] provides three coupled wave equations, which describe any second-order frequency mixing process by,

$$\frac{dE_{1i}}{dz} = -\frac{i\omega_1}{cn_1} d'_{ijk} E_{3j} E^*_{2k} e^{(-i\Delta kz)},$$

$$\frac{dE^*_{2k}}{dz} = \frac{i\omega_2}{cn_2} d'_{kij} E_{1i} E^*_{3j} e^{(+i\Delta kz)}, \text{ and} \qquad 2.15$$

$$\frac{dE_{3j}}{dz} = -\frac{i\omega_3}{cn_3} d'_{jik} E_{1i} E_{2k} e^{(+i\Delta kz)},$$

where convention designates the frequencies in the order

$$\omega_1 \leq \omega_2 < \omega_3 ,$$

and with

$$\Delta k = k_3 - k_2 - k_1$$

defined as the *wave-vector mismatch*. An efficient exchange between the interacting waves is possible only if $\Delta k = 0$. The condition $\Delta k = 0$ can be achieved by using a careful choice of propagation directions inside a dispersive and birefringent medium. The work in this thesis exclusively employs an alternative approach known as quasi-phasematching, in which $\Delta k \neq 0$.

2.2.4 Quasi-phase-matching

In the case where the three interacting waves propagate in a dispersive medium (which all $\chi^{(2)}$ possessing materials are), the relative phase between them after some certain propagation length accumulates to π as

$$\Delta\phi = \phi_3 - \phi_2 - \phi_1 = \pi . \qquad 2.16$$

For the propagation distance where the phase difference remains in the range from zero to π, the conversion intensity builds up to a maximum and this length is known as the coherence length,

$$L_{coherence} = \frac{\pi}{\Delta k} . \qquad 2.17$$

Beyond the coherence length, the converted intensity decreases again because the phasematching condition is now such that *back conversion* occurs from the generated frequencies back into the fundamental frequency. In order to avoid back conversion and to increase the efficiency of the forward conversion by extending the available interaction length, a process is required to return to the phasematching condition. This

is possible by adding a phase step $+i\pi$ to all three fields after they have propagated for one coherence length:

$$\frac{dE_{1i}}{dz} = -\frac{i\omega_1}{cn_1} d'_{ijk} E_3 E_2^* e^{(-i\Delta kz + i\pi)},$$

$$\frac{dE_{2k}^*}{dz} = \frac{i\omega_2}{cn_2} d'_{kij} E_1 E_3^* e^{(+i\Delta kz + i\pi)}, \text{ and} \qquad 2.18$$

$$\frac{dE_{3j}}{dz} = -\frac{i\omega_3}{cn_3} d'_{jik} E_i E_2 e^{(+i\Delta kz + i\pi)}.$$

Physically this is achieved by periodically flipping the polarity of the nonlinear tensor d_{ijk} with a period of twice the coherence length, called the *quasi-phasematching period*:

$$\Lambda_g = 2L_{coherence} = \frac{2\pi}{\Delta k}. \qquad 2.19$$

Therefore, the condition for quasi-phasematching (QPM) can be stated as

$$\Delta k_{qp} = k_3 - k_2 - k_1 - \frac{2\pi}{\Lambda_g} = 0. \qquad 2.20$$

Tuning of the phasematching is possible simply by varying the phasematching period, which must satisfy the two former expressions, giving:

$$\Lambda_g = \left[\frac{n(\lambda_3)}{\lambda_3} - \frac{n(\lambda_2)}{\lambda_2} - \frac{n(\lambda_1)}{\lambda_1}\right]^{-1}. \qquad 2.21$$

Although the quasi-phasematching approach introduces a non-zero phase condition through most of a conversion cycle, it is superior to birefringent phasematching, where the refractive index mismatch between ordinary and extraordinary rays is utilised, to achieve true phasematching where $\Delta k = 0$. The reason for this is that for birefringent phasematching the individual waves require a combination of perpendicular and parallel

polarisation directions (Type I or Type II interaction) whereas for QPM all three interacting waves are allowed to have the same polarisation direction (Type 0 interaction) and therefore able to exploit the d_{ijk} tensor component yielding the strongest nonlinear interaction in a specific crystal. Such a "Type 0" interaction can be up to an order of magnitude stronger and so QPM therefore yields much higher efficiencies.

Periodic inversion of the polarity inside a crystal can be achieved by using a technique known as *periodic poling*. In a crystal like $LiNbO_3$, which is ferroelectric, a strong electric field can be used to alter the position of the Li and Nb ions inside the unit cells, leading to the desired effect. By extending the technique a whole grating of inversely poled domains can be built by using many small electrodes attached to the outside of a crystal, allowing manufacturing of crystals with domain lengths down to sub-10 µm (required for SHG) and with several centimetres of QPM interaction length. In addition, QPM can be achieved by physical cut and bonding, epitaxial growth, as well as by periodic destruction of the $\chi^{(2)}$-nonlinearity by turning the medium amorphous.

2.2.4.1 Second- harmonic generation

Solving the coupled-wave equations analytically is often very difficult. In some cases, it is possible to obtain a solution, which leads to useful analytic expressions by making some simplifications. Studying the coupled-wave equations for the instance of second-harmonic generation is possible by assuming a process with low conversion efficiency where, $\frac{dE_1}{dz} \approx \frac{dE_2}{dz} \approx 0$, which allows us to reduce the problem so that only one equation remains to be solved:

$$\frac{dE_{3j}}{dz} = -\frac{i\omega_3}{cn_3} d'_{jik} E_1 E_2 e^{(+i\Delta kz)} . \qquad 2.22$$

with $\omega_1 = \omega_2 = \omega_3/2$ and the electric field component of frequency ω_3 to be

$$E_3 = ae^{(+i\Delta kz)} + b, \tag{2.23}$$

where by differentiation we can obtain

$$\frac{dE_3}{dz} = ai\Delta ke^{(+i\Delta kz)}. \tag{2.24}$$

By setting equation 2.22 equal with 2.24 we acquire

$$a = -\frac{\omega_3 d'_{jik} E_1 E_2}{cn_2 \Delta k}. \tag{2.25}$$

Because no coupling has taken place on the beginning of the process, we can apply the boundary condition $E_3(z = 0) = 0$ and solve for b gaining,

$$b = -a = \frac{\omega_3 d'_{jik} E_1 E_2}{cn_2 \Delta k}. \tag{2.26}$$

With ω as the input (pump) frequency the analytic expression for the electric field of the SHG is,

$$E_3 = \frac{2\omega d'_{jik} E_1 E_2}{cn_3 \Delta k} \left(1 - i\Delta ke^{(+i\Delta kz)}\right). \tag{2.27}$$

In order to obtain the intensity of the electric field of equation 2.27 one applies $I_3 = nc\epsilon_0 E_3 E_3^* /2$ to obtain,

$$I_{2\omega}(z) = \frac{8\omega^2 d'^2_{jik} I_\omega^2 z^2}{c^3 n_1 n_2 n_3 \epsilon_0} \mathrm{sinc}^2\left(\frac{\Delta kz}{2}\right). \tag{2.28}$$

If the phasematching condition is $\Delta k \neq 0$, the second-harmonic intensity follows $\mathrm{sinc}^2(\Delta kz/2)$ with its maximum conversion over one coherence length. For the situation where $\Delta k = 0$, the second harmonic increases quadratically with propagation

length z as well as with incident intensity I. The analytic result indicates also a quadratic decrease with increasing wavelength [16].

2.2.4.2 *Sum- and difference frequency generation*

Again, the coupled-wave equations for sum-and difference-frequency generation can only be analytically solved with the assumption for low pump depletion (or constant (undepleted) pump intensity through the crystal). For sum-frequency generation the waves ω_1 and ω_2 are mixed to generate a wave $\omega_3 = \omega_1 + \omega_2$ with the shortest wavelength.

With perfect phase matching and operation in the low conversion regime, sum-frequency generation can be analytically expressed by ,

$$E_1(z) = E_1(0)\cos(\Gamma' z), \tag{2.29}$$

and

$$E_3(z) = iE_1(0)\sqrt{\left(\frac{\omega_3 n_1}{\omega_1 n_3}\right)}\sin(\Gamma' z). \tag{2.30}$$

while Γ' represents the gain and coupling coefficient for SFG. A detailed treatment can be found in Chapter 2 of Nonlinear Optics by Boyd [14]. The two solutions describe how energy is exchanged forward and backward between the input wave ω_1 and output wave ω_3 during their propagation through the crystal.

For difference-frequency generation, with a high frequency pump wave ω_3 and low frequency wave ω_1 incident on the nonlinear crystal, the same simplifications implied for SFG give the analytical expression,

$$E_1(z) = E_1(0)\cosh(\Gamma' z)\,, \qquad 2.31$$

and

$$E_2^*(z) = -iE_1(0)\sqrt{\frac{n_1\omega_2}{n_2\omega_1}}\sinh(\Gamma' z)\,. \qquad 2.32$$

The incident long wave ω_1 and the generated wave $\omega_2 = \omega_1 - \omega_3$ both increase in intensity while they propagate along z, following a monotonic growing function at the expense of the pump wave ω_3.

2.2.4.3 Optical parametric oscillation

The fact that the difference-frequency generation yields amplification indicates that a further application of the χ^2 gain is possible. A resonant cavity, similar to a classical laser resonator can be employed to enhance the parametric optical amplification, where such a resonator is known as an optical parametric oscillator (OPO). For OPOs, the frequencies of the three interacting waves $\omega_1 \leq \omega_2 < \omega_3$ are conventionally denoted as $idler\ (\omega_i) \leq signal\ (\omega_s) \leq pump\ (\omega_p)$ respectively. A resonator where the mirrors used are highly reflective for either the signal or the idler wave is described as a *singly resonant* oscillator. A cavity where the reflectivity extends over both, signal and idler wavelength is called a *doubly resonant* oscillator. The OPO-operation where the phasematching conditions are such, that signal and idler wavelength are overlapping and resonant at double of the pump wavelength (the inverse process of SHG) is known as *degeneracy*.

Solving the coupled-wave equations for the case of an oscillator requires the consideration of all three waves. Employing the coupled-amplitude equations and assuming the special case of perfect phase matching where $\Delta k = 0$ and that the idler wave ω_i is not resonant and therefore is zero at the start of the process ($A_i(0) = 0$), leads to a simplified solution [14] with

$$A_s(z) = A_s(0)\cosh gz \quad \text{and} \tag{2.33}$$

$$A_i(z) = \sqrt{\frac{n_1\omega_2}{n_2\omega_1}}\frac{A_p}{|A_p|}A_i^*(0)\sinh gz, \tag{2.34}$$

where $g = \sqrt{\kappa_1\kappa_2^* - (\Delta k/2)^2}$ is the gain coefficient and the coupling coefficient is defined as $\kappa_i = 2i\omega_i^2 d_{eff}A_p/k_i c^2$. Very similar to the solution of DFG, the idler and signal wave experience asymptotic growth with propagation distance. The optical parametric oscillator has proven to be a versatile source comprising a wide tunability mostly limited by the reflectivity of the available mirror coatings. OPOs can be operated either in a CW-mode or in a pulsed regime with pulse durations from nanoseconds to femtoseconds, depending on the pump source and phasematching geometry. A special requirement of its pulsed operation is synchronous pumping where the cavity length of the OPO needs to be perfectly matched to the repetition rate of the pump laser. The synchronicity is crucial because, in contrary to a pulsed laser where absorption and gain storage is present, the underlying $\chi^{(2)}$ process and therefore the inherent gain is instantaneous and only builds up if a generated pulse coherently overlaps after one roundtrip in the resonator with the next incident pump pulse inside the crystal.

2.3 Ultrafast pulse dynamics

Once an ultrafast pulse is generated, for instance by the processes described in the previous section, it is continuously reshaped in its temporal and spectral profile by linear and nonlinear mechanisms related to the medium in which it propagates. In addition, geometrical dispersion and mirror dispersion can influence the shape, which is in some cases deliberately used to counteract the intrinsic distortion for instance caused by a gain medium inside a cavity. In order to understand these dynamics, a description of some of the involved processes is given in this section.

2.3.1 Definition of an ultrafast pulse

A pulse with a centre frequency given at ω_0 can be represented by a complex envelope function with the real electric field as,

$$E(t) \propto \mathrm{Re}\{A(t)e^{(i\omega_0 t)}\}, \qquad 2.35$$

where $A(t)$ is defined as the normalized electric field amplitude with the instantaneous optical power defined as $|A(t)|^2$, detected for instance with a photodiode. By performing a Fourier transform of the complex temporal field, we are able to derive its equivalent in the spectral domain analytically as

$$A(\omega) = \frac{1}{\sqrt{2\pi}} \int_{-\infty}^{\infty} A(t)e^{(-i\omega_0 t)} dt\,. \qquad 2.36$$

Due to our previous normalisation of the electric field amplitude in the time domain, we can equivalently obtain the real power spectrum of the pulse by $|A(\omega)|^2$.

The relationship between the temporal width of a pulse and its spectral bandwidth is known as the time-bandwidth product $\Delta\tau_p\Delta\nu_p$. Both the spectral and temporal widths of a pulse are measured at the full width at half-maximum (FWHM). Two important temporal shapes are: i) The Gaussian temporal shape $\left(e^{(-2\ln 2\, t^2/\Delta\tau_p^2)}\right)$ with a minimum time-bandwidth product $\Delta\tau_p\Delta\nu_p$ of 0.441; ii) The Hyperbolic secant temporal shape $\left(\mathrm{sech}\left(1.763t/\Delta\tau_p\right)\right)$ with a minimum time-bandwidth product $\Delta\tau_p\Delta\nu_p$ of 0.315. Any positive or negative chirping of the pulse, for instance by dispersion, increases the minimum time-bandwidth product.

2.3.2 Definition of dispersion

Any medium other than a vacuum introduces dispersion, an effect arising from the fact that the refractive index is frequency dependent, which implies that different spectral components of the pulse travel at different velocities introducing a phase delay. This can be accounted for by introducing a frequency dependent phase term with

$$A(\omega)' = A(\omega)e^{(i\varphi(\omega))}, \qquad 2.37$$

which is transformed into the time domain by an inverse Fourier transformation

$$A(t)' = \frac{1}{\sqrt{2\pi}} \int_{-\infty}^{\infty} A(\omega)' e^{(-i\omega t)} d\omega \,. \qquad 2.38$$

This spectral phase variation corresponding to first, second, and higher order dispersion is commonly defined via the Taylor expansion of the wave vector k, representing the spectral phase change per unit length as a function of the angular frequency ω relative to the mean frequency of the pulse ω_0:

$$\begin{aligned} \varphi(\omega) = \varphi(\omega_0) &+ (\omega - \omega_0) \left(\frac{\partial \varphi}{\partial \omega}\right)\Big|_{\omega_0} \\ &+ \frac{1}{2}(\omega - \omega_0)^2 \left(\frac{\partial^2 \varphi}{\partial \omega^2}\right)\Big|_{\omega_0} \\ &+ \frac{1}{6}(\omega - \omega_0)^3 \left(\frac{\partial^3 \varphi}{\partial \omega^3}\right)\Big|_{\omega_0} + \ldots \end{aligned} \qquad 2.39$$

The zero-order term (the first part) in equation 2.39 represents a common phase shift of the carrier wave and has no effect on the pulse shape. The second part contains a first-order term introducing a linear change of the phase in the frequency domain corresponding in the time domain to a delay known as the group delay τ_g.

The relation between group delay and group velocity for a certain physical length z is simply defined by:

$$v_g = \frac{z}{\tau_g}, \qquad 2.40$$

and is the velocity at which the envelope of the pulse travels through the medium.

All higher terms are a measure of the change of the group delay with respect to the wavelength and have an influence on how the shape of the pulse changes during propagation. The rate how the delay changes during propagation inside a dispersive medium is described by the group-delay dispersion (GDD):

$$GDD = \left.\frac{\partial \tau_g}{\partial \omega}\right|_{\omega_0} = \left.\frac{\partial^2 \varphi}{\partial \omega^2}\right|_{\omega_0}, \qquad 2.41$$

and is usually given in units of fs^2.

The term $(\omega - \omega_0)^3$ is associated with cubic spectral phase variations leading to steepening of one edge of the pulse and stretching of the other, eventually resulting in separation of the pulse, a process known as pulse break-up. The quantity known as third-order dispersion (TOD) has units of fs^3, given by,

$$TOD = \left.\frac{\partial^3 \varphi}{\partial \omega^3}\right|_{\omega_0}. \qquad 2.42$$

Controlling the net intracavity dispersion is crucial for achieving ultrashort pulses (few cycle regime). This is achieved once the quadratic and higher-order spectral phase terms associated with one cavity roundtrip are negligible across the entire spectral bandwidth of the pulse. The dispersion accumulated during a roundtrip inside a cavity may originate from a number of sources.

2.3.3 Material dispersion

Material dispersion is associated with the wavelength-dependent refractive index of dielectric media, which is introduced in an OPO by the nonlinear crystal. For propagation in bulk dielectric media, the material dispersion can be determined in terms of the rate of change of the wavelength-dependent refractive index, $n(\lambda)$ in respect to wavelength. The wavelength dependent refractive index for many materials is readily accessible by a Sellmeier equation. Therefore, it is more practical to provide equations 2.41 and 2.42 in a form ready to accept the refractive index and wavelength by,

$$GDD = \frac{\lambda^3 z}{2\pi c^2}\frac{d^2 n}{d\lambda^2}, \qquad 2.43$$

and

$$TOD = -\frac{\lambda^4 z}{4\,\pi^2 c^3}\left(3\frac{d^2n}{d\lambda^2} + \lambda\frac{d^3n}{d\lambda^3}\right). \qquad 2.44$$

2.3.3.1 A pair of prisms for dispersion compensation

In contrast to material dispersion, geometrical dispersion arises from the wavelength-dependent path lengths that can be observed in optical systems exhibiting angular dispersion, such as prisms or diffraction gratings. The GDD and TOD of cavities containing angular dispersive elements may be controllable by a careful combination of materials and geometrical layouts used for net dispersion compensation.

Using a prism pair to implement dispersion compensation in a resonator requires a careful calculation of the separation l between the two tips of the prisms to achieve the required dispersion while accounting the material dispersion introduced by the additional glass path. This can be calculated using the following expression [17]:

$$GDD = \frac{d^2\varphi}{d\omega} = \frac{\lambda^3}{2\pi c^2}\frac{d^2P}{d\lambda^2}, \qquad 2.45$$

with

$$\frac{d^2P}{d\lambda^2} = 4l\sin\beta\left(\frac{d^2n}{d\lambda^2} + \left(2n - \frac{1}{n^3}\right)\left(\frac{dn}{d\lambda}\right)^2\right) - 8l\cos\beta\left(\frac{dn}{d\lambda}\right)^2.$$

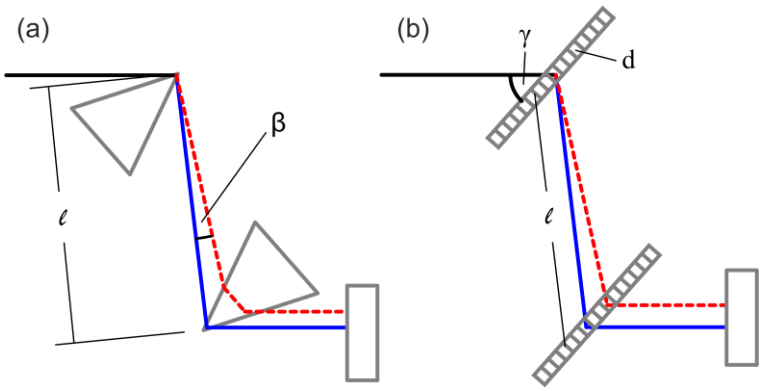

Figure 2.1. a) Schematic for double-pass prims compressor with the apex separation l and angular deviation β b) Schematic for double-pass grating compressor with separation l, angle of incidence γ and line spacing d.

2.3.3.2 *A pair of gratings for dispersion compensation*

A further common way to achieve geometrical dispersion is the implementation of a intracavity pair of diffraction gratings. Similar to the requirements for prisms, it is necessary to calculate the distance and diffraction angle in order to obtain a flat cavity dispersion characteristic. This is maybe calculated with the equation [18,19]:

$$GDD = \frac{d^2\varphi}{d\omega} = l\frac{\lambda^3}{\pi c^2 d^2}\left(1-\left(\frac{\lambda}{d}-\sin\gamma\right)^2\right)^{-3/2}. \qquad 2.46$$

2.3.3.3 *Dielectric mirror coatings*

Mirror dispersion results from interference effects from a dielectric Bragg mirror coatings. All dielectric coated mirrors show GDD with an increase towards the upper and lower reflectivity edges. This can be explained due to the effect where, for instance, at the long wavelength edge the longer wavelengths gradually penetrate deeper into the Bragg layers until they are reflected, introducing an increasing delay as the wavelengths become longer. Its application to achieve femtosecond pulses was first reported in [20].

A chirping of the Bragg period [21] allows the design of mirrors with very specific GDDs over a certain wavelength range. For chirped mirror coatings, an implementation

of pairs with matched coatings is required due to unavoidable modulations in the GDD characteristics.

Gires-Tournois interferometer (GTI) mirrors [22] offer an alternative means of introducing GDDs several times those of a chirped mirror coating, where the coating comprises an embedded etalon-like structure with the benefit that a matched pair is not required anymore, but with the disadvantage that the reflectivity bandwidth is narrower.

2.4 Self-phase modulation

The optical Kerr effect describes the intensity dependence of a materials refractive index according to:

$$n = n_0 + n_2 I(t)\,. \qquad 2.47$$

The time-varying intensity profile of a pulse introduces a larger nonlinear refractive index change at the peak and therefore the more intense part experiences a greater phase shift than the weaker components of the propagating pulse.

The resulting frequency shift of the spectral self-phase-modulation (SPM) can be expressed by:

$$\omega'(t) = -\frac{d\phi(t)}{dt} = -\frac{\omega n_2 L}{c}\frac{dI(t)}{dt}\,, \qquad 2.48$$

where n_2 is the nonlinear refractive index of the medium. SPM is a $\chi^{(3)}$process where the leading edge of an intense pulse is red-shifted while the trailing edge experiences a blueshift. For SPM the centre of the pulse undergoes a nearly linear positive chirp, which can be compensated with an equal but opposite amount of negative GDD. SPM is commonly used to spectrally broaden pulses, which allows one to achieve very short

pulses by subsequently compressing a broadened pulse with the correct amount of linear dispersion.

2.5 Pulse characterisation techniques

Ultrafast optical pulses are not accessible with any direct electric measurement technique. Since the advent of pulses with pico- and femtosecond durations, many techniques have been established in order to estimate or precisely acquire the temporal shape of a pulse. Because electronics is not able to examine directly an ultrashort pulse, the pulses have to be sampled with the use of a second ultrafast pulse and their temporal shape measured indirectly. One way to obtain a duration estimate of an ultrafast pulse is with the technique known as temporal autocorrelation. The interferometric autocorrelation function is the correlation of the electric field with itself [23]:

$$g_2(\tau) = \frac{\int_{-\infty}^{\infty} \left| \left(E(t) + E(t-\tau) \right)^2 \right|^2 dt}{2\int_{-\infty}^{\infty} |E^2(t)|^2 dt}, \qquad 2.49$$

and requires two identical pulse-replicas with a variable delay τ between them. The preferred experimental setup is a classical Michelson interferometer with a beam splitter in the centre providing a 50/50 distribution of the identical pulse into each arm. One arm in the setup is mounted on a linear transducer to create a repetitive delay ranging from $-\tau$ to τ. In the experiment, the SHG signal of the two identical pulses interfering with each other inside a nonlinear material is recorded. Either a nonlinear crystal or a two–photon absorption process inside a photodiode can be conveniently exploited where it is important to use a suitable diode sensitive only at the second harmonic signal but not at fundamental wavelength. If the detector does not provide enough bandwidth, the autocorrelation fringes smear out into an averaged trace known as an intensity autocorrelation analytically described by,

$$s(\tau) = \frac{2\int_{-\infty}^{\infty} I(t)I(t-\tau)dt}{\int_{-\infty}^{\infty} I^2 dt}. \qquad 2.50$$

Synchronous to the autocorrelation measurement, the spectrum of a pulse is acquired. Once both traces have been processed, the spectrum can be inverse Fourier transformed in order to calculate the shortest possible pulse. The generated pulse is then numerically autocorrelated with itself to generate a trace similar to the one recorded with the experiment. By adding quadratic and cubic phase to the recorded spectrum, a best fit between simulated and measured autocorrelation trace is achieved. A quicker estimate of the pulse duration can be obtained by using the autocorrelation FWHM that is proportional to the pulse FWHM but pulse–shape dependent. Due to this it is necessary to assume, one of the standard shapes and apply for a Gaussian pulse a factor of $\sqrt{2}$ and for a $\mathrm{sech}^2(t)$ temporal shape 1.543 respectively.

Because the spectral phase cannot be extracted in this experimental setup, it is impossible to retrieve the exact pulse shape. However, for a well-behaved pulse and spectrum, this provides a good estimate of the real pulse shape. As soon as the pulse is spectrally broadened by SPM it is impossible to estimate the pulse shape because the fitting allows no distinction between linear and nonlinear accumulated phase.

For pulses containing structured spectra and more complex phase profiles, frequency-resolved optical gating (FROG) or spectral phase interferometry for direct electric-field reconstruction (SPIDER) offer a much more systematic way to obtain the full spectral and temporal shape of a pulse allowing the formation of the true picture of the pulse profile.

2.6 Conclusions

Although far from complete, this chapter's aim was to provide the reader with necessary fundamentals of nonlinear processes as well as ultrafast pulse shaping and characterisation in order to understand the experimental results provided in the following chapters. The techniques discussed (quasi-phasematching, pulse compression and autocorrelation) are used extensively throughout the work described in the following chapters.

Chapter 3- Yb:fibre-laser pumped high-energy picosecond optical parametric oscillator

3.1 Introduction

The recent emphasis on developing ultrafast oscillators that can directly provide high-energy pulses at multi-MHz repetition rates has been driven by their potential to replace more complex and expensive ultrafast amplifier systems in certain applications. In particular, refractive index modification in common dielectric materials has been shown to be possible using pulse energies of only a few nJ, with a 25-MHz Ti:sapphire laser oscillator being used to write waveguides inside borosilicate glass, with a modification threshold of only 5 nJ [12]. Systematic studies now provide strong support for implementing laser waveguide writing at repetition rates above 1 MHz [24], where a reduction of the modification threshold energy from 750 nJ to 80 nJ has been shown to be possible simply by increasing the repetition rate from 200 kHz to 2 MHz [24]. High-energy multi-MHz repetition-rate ultrafast oscillators, some including cavity-dumping elements [25], are the sources of choice for waveguide inscription in this regime, and their development has been technically enabled by designs incorporating an extended cavity scheme using an intracavity Herriott-cell [26,27] or relay-imaging mirror sequence [28]. Such laser systems have been limited to wavelengths below 1250 nm, relying either on Ti:sapphire [24,25], Nd-doped [29], Yb-doped [25] or Cr^{4+}-doped [26] gain materials.

Many infrared materials, which are interesting candidates for ultrafast waveguide inscription, cannot be inscribed at short wavelengths, and require irradiation at wavelengths considerably longer than 1 µm. For example, inscription in silicon requires pulses longer than 1.1 µm, germanium 1.8 µm and chalcogenide glasses range from 0.6 to 1.5 µm. High-energy near-infrared oscillators are therefore required for this application, particularly those with diffraction-limited outputs that permit the lowest modification threshold to be achieved by using high-numerical-aperture focusing [12]. Synchronously pumped optical parametric oscillators (OPOs) offer a route to extending the wavelength coverage of high-energy ultrafast oscillators to the near and mid-infrared, and a cavity-dumped high-repetition-rate (82 MHz) OPO has been reported

which produced 1 MHz, 90 nJ pulses at 1200 nm [11]. A fibre-feedback OPO, synchronously pumped by a 58 W thin-disc laser [8], achieved 56 MHz, 339 nJ at 1450 nm, although the weak cavity feedback associated with this geometry led to a non-diffraction-limited (M^2 =1.6) output beam.

In this chapter, an extended-cavity OPO operating at 15.3 MHz and pumped by a femtosecond Yb:fibre master-oscillator fibre-amplifier (MOFA) is introduced. An Yb:fibre MOFA represents an inexpensive high-energy source, where the repetition rate can be readily reduced to frequencies as low as 10 MHz by changing the cavity length of the oscillator. Previous work reported an Yb-fibre-amplifier-pumped femtosecond OPO that produced 1.7 nJ pulses at 1550 nm [30]. The work described in this chapter demonstrates how, by using intracavity relay-imaging in a conventional free-space resonator, energy scaling up to 72 nJ is possible, corresponding to the highest energies directly produced from a free-space ultrafast OPO, and representing a promising new source for waveguide inscription in infrared materials.

3.2 Yb:fibre pump laser

3.2.1 Overview of Yb:fibre laser

The OPO was pumped by a commercial sub-picosecond Yb:fibre laser (Fianium FemtoPower 1060-10), which operated at a centre wavelength of 1064 nm with a pulse-repetition frequency of 15.3 MHz. The laser was a simple architecture based on a picosecond master oscillator followed by a power amplifier stage as schematised in Figure 3.1. The amplification scheme consisted of an ytterbium-doped fibre amplifier (YDFA) and a second cladding-pumped high-power amplifier similar to references [31,32]. The pump-diodes (PD), which are coupled into the fibre cladding (PC), operated at 975 nm. Optical isolators were present between each stage and at the output of the laser. This is an essential requirement since fibre amplifiers are very sensitive to feedback reflections at their own laser wavelength due to their high gain.

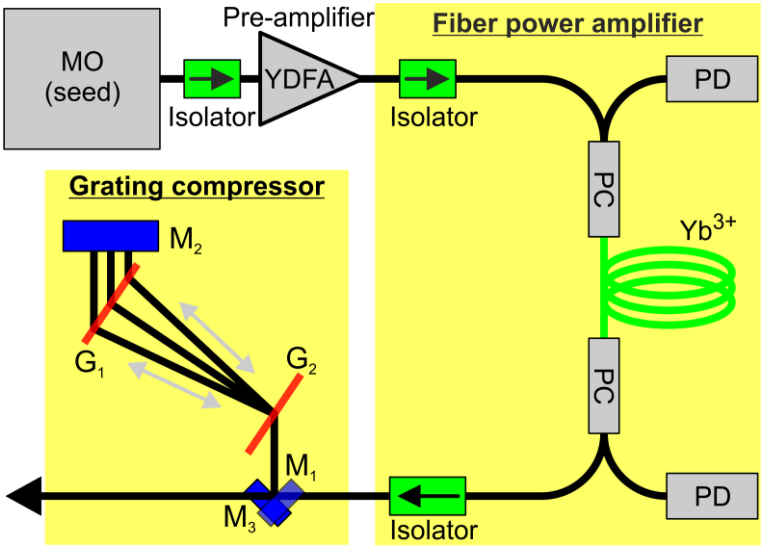

Figure 3.1. Fianium FemtoPower Yb:fibre master oscillator fibre amplifier (MOFA) schematic followed by the home-build transmission-grating compressor. The master oscillator (MO) was a diode pumped fibre oscillator.

The picosecond pulses produced by the master oscillator acquire a broad bandwidth through self-phase modulation during amplification in the final stage. The resulting chirped pulses had a duration of 7 ps with a bandwidth of approximately 25 nm and an average power of 10.1 W corresponding to energies of around 660 nJ.

3.2.2 Pump laser pulse measurement and compression

The pulses were compressed using a grating compressor comprising a pair of fused-silica transmission gratings (Ibsen Photonics) as indicated in Figure 3.1(compressor section). The compression factor could be optimized by adjusting the distance between grating G_1 and G_2 [19]. Although the chirp on the output pulses was not fully compressible, the grating compressor achieved pulse durations of approximately 440 fs (FWHM) with an efficiency of 63.5% leading to a pulse energy of 420 nJ. The compressor efficiency was optimised and was determined by the ratio of available power measured before and after the section. The pulse duration was limited due to the strongly SPM-modulated spectrum to a time bandwidth product of 2.3 (λ_c = 1066 nm, $\Delta\lambda$ = 20 nm, and $\Delta\tau$ = 440 fs).

Figure 3.2 shows the interferometric autocorrelation trace acquired using two-photon absorption in a GaAsP photodiode [33] and the spectrum of the Yb:fibre laser both

measured at the same instance after the compressor. The spectra of the pulses showed substantial structure due to the above-mentioned nonlinear spectral broadening. The measurements were performed at the maximum pump current available from the Fianium fibre laser to ensure a consistent spectral and temporal shape of the provided laser pulses during operation.

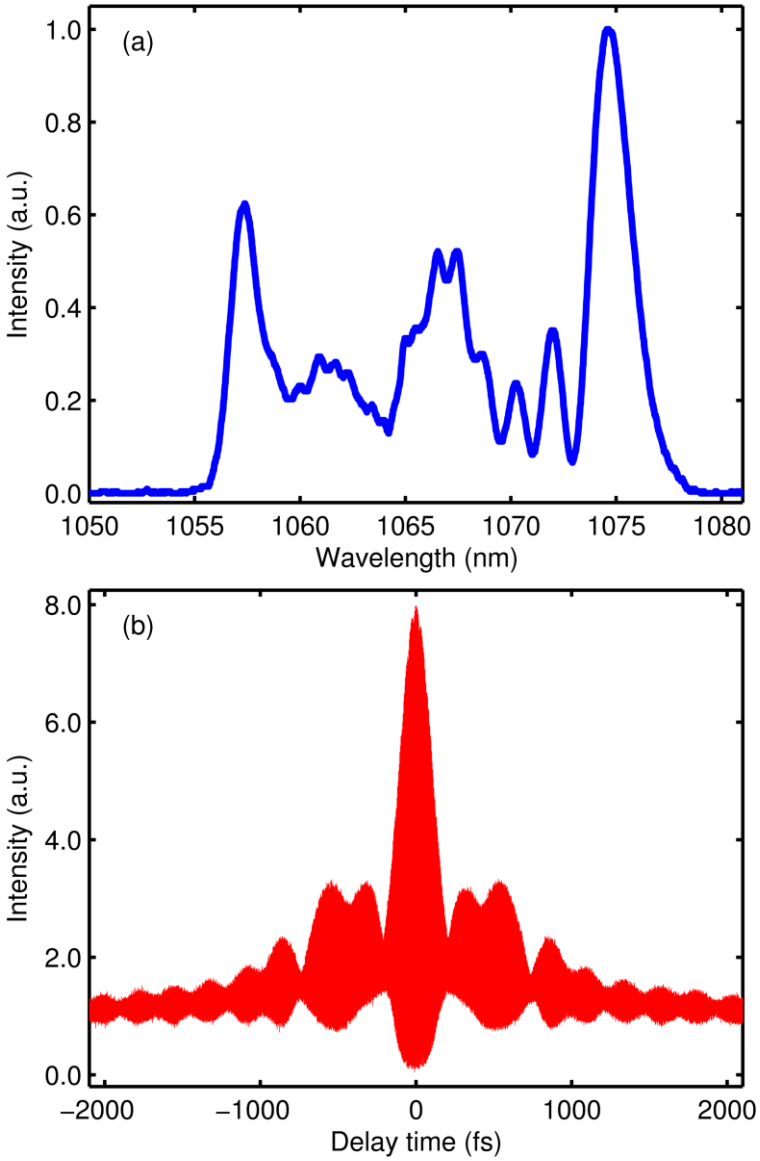

Figure 3.2. (a) Spectrum measured from the Fianium Yb:fibre laser; (b) Interferometric autocorrelation measurement after the grating compressor optimised for best compression. Both plots show considerable modulation due to self-phase modulation.

Due to the strong modulation of the spectra, the Gaussian or $\mathrm{sech}^2(t)$ intensity profiles commonly used to infer pulse durations from autocorrelation measurements, are not suitable. The plotted interferometric autocorrelation in Figure 3.2(b) reflects these

strong spectral modulations as deep time-domain modulations. A best-fit to the obtained experimental autocorrelation by optimizing the amount of quadratic and cubic phase added to the spectrum did not provide satisfactory agreement. Adding an additional nonlinear phase shift to the spectrum has proven to be beyond the scope of the used measurement technique. The two measurements of the spectrum and the interferometric autocorrelation profile do not provide sufficient information to fit unambiguous profiles. Employing a technique like FROG or SPIDER would be necessary to allow a full recovery of the temporal intensity and phase profiles of the pulses.

3.2.3 PPLN crystal design

The OPO was based on a 5%MgO-doped periodically poled $LiNbO_3$ (MgO:PPLN) crystal consisting of eight uniform gratings with quasi phase-matched (QPM) periods ranging from 23 – 32 µm. However, only four gratings, 28 - 31 µm yielded successful OPO operation within the active length of 1.04 mm. The crystal layout is shown in Figure 3.3 indicating the position of the individual cells and their dimensions.

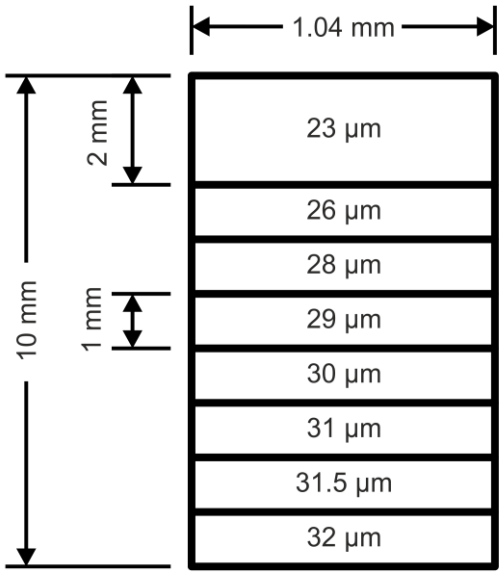

Figure 3.3. MgO:PPLN crystal dimensions are 1.04 mm(L) x 10.0 mm(W) x 0.5 mm(D).

Adding a doping concentration of 5% Magnesium Oxide (MgO) to a PPLN increases the optical and photorefractive resistance significantly compared to a pure Lithium Niobate crystal while preserving its high nonlinear coefficient. This allows more stable

operation at lower temperature operation. To permit temperature tuning, and as an added precaution against photorefractive damage, the crystal was mounted in an oven and its temperature was maintained at 85°C. In Figure 3.4 the phasematching bandwidth is plotted in relation of grating period and wavelength for this crystal.

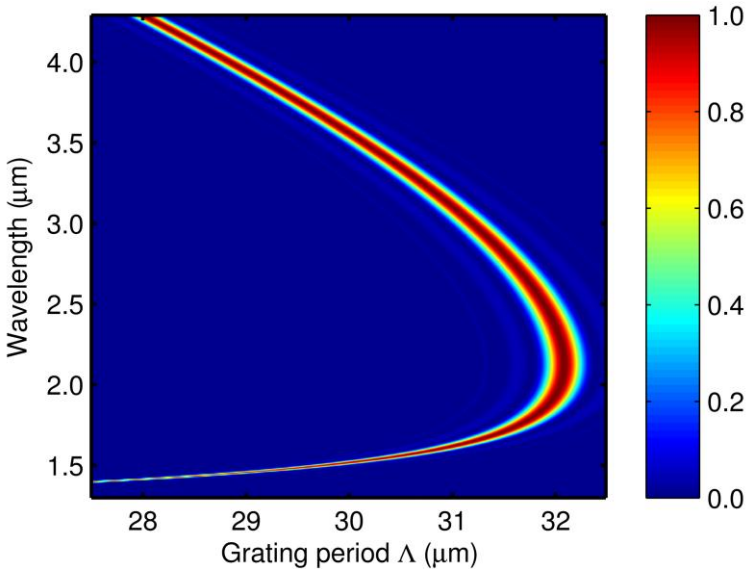

Figure 3.4. MgO:PPLN phase matching efficiency map for a pump wavelength of 1064 nm, a crystal length of 1040 µm, and covering grating periods from 27.5 to 32.5 µm with a bulk temperature of 85°C.

The crystal was fabricated with plane-parallel faces which were anti-reflection coated over a wavelength range from 0.8 - 1.55 µm. The measured coating performance can be seen in Figure 3.5 showing approximately 1% reflection per surface at 1064 nm and 1500 nm. The idler reflectivity can be approximated by the Fresnel losses of MgO:PPLN at 3 to 4 µm to be about 12.5%.

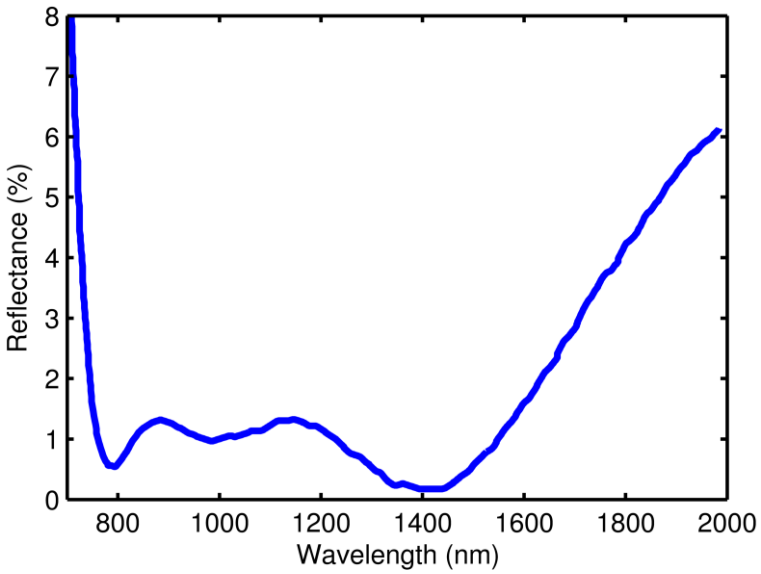

Figure 3.5. MgO:PPLN crystal anti reflection coating curve as measured by the supplier HCP.

3.3 Optical parametric oscillator design

3.3.1 Cavity design

Several factors influenced the choice of focusing into the crystal. To minimize the risk of surface damage to the MgO:PPLN crystal we chose a pump beam radius of 40 µm (defined at $1/e^2$ intensity point) which represented a compromise between parametric gain and damage considerations [34]. This focal spot radius was also readily compatible with the minimum spot size to which the pump pulses could be focused. The pump laser exhibited a beam quality factor of $M^2 \sim 1.3$, which originates from its use of 50 µm-diameter large-mode-area fibre within the Yb:fibre amplifier, and is poorer than that obtained from solid-state lasers such as Ti:sapphire that are more commonly used as pump sources for femtosecond OPOs. By characterizing the pump beam diameter, we achieved the required focal diameter by using a single 100 mm-focal-length lens placed 750 mm after the laser head.

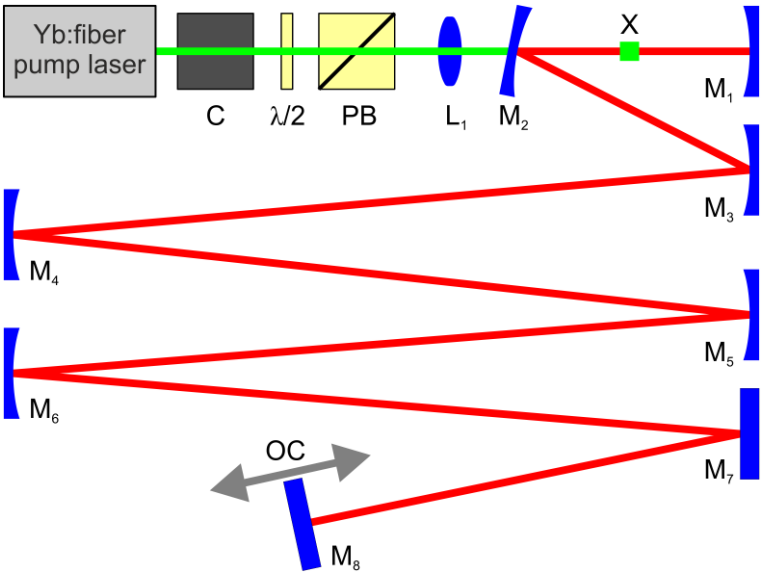

Figure 3.6. The OPO and pump optics, including a compressor (C), a variable attenuator, comprising a half-wave plate (λ/2) and polarizing beam splitter cube (PB), and a focusing lens (L_1). X marks the MgO:PPLN crystal; M_1 and M_2, concave focusing mirrors of radii 150 mm and 200 mm respectively; M_3 - M_6, concave relay-imaging mirrors with radii of 2000 mm; M_7 and M_8, plane high-reflectivity and output coupling mirrors respectively.

The pump beam was introduced into the OPO cavity by pumping through one of the OPO focusing mirrors, as illustrated in Figure 3.6. The OPO resonator was based on an asymmetric "V-cavity" design, with the focusing section around the crystal comprising a concave end-mirror with a radius of 150 mm and a turning mirror with a radius of 200 mm, which collimated the intracavity beam into an arm of length 9.55 m. The beam profile through the focusing section of the crystal is presented in Figure 3.7.

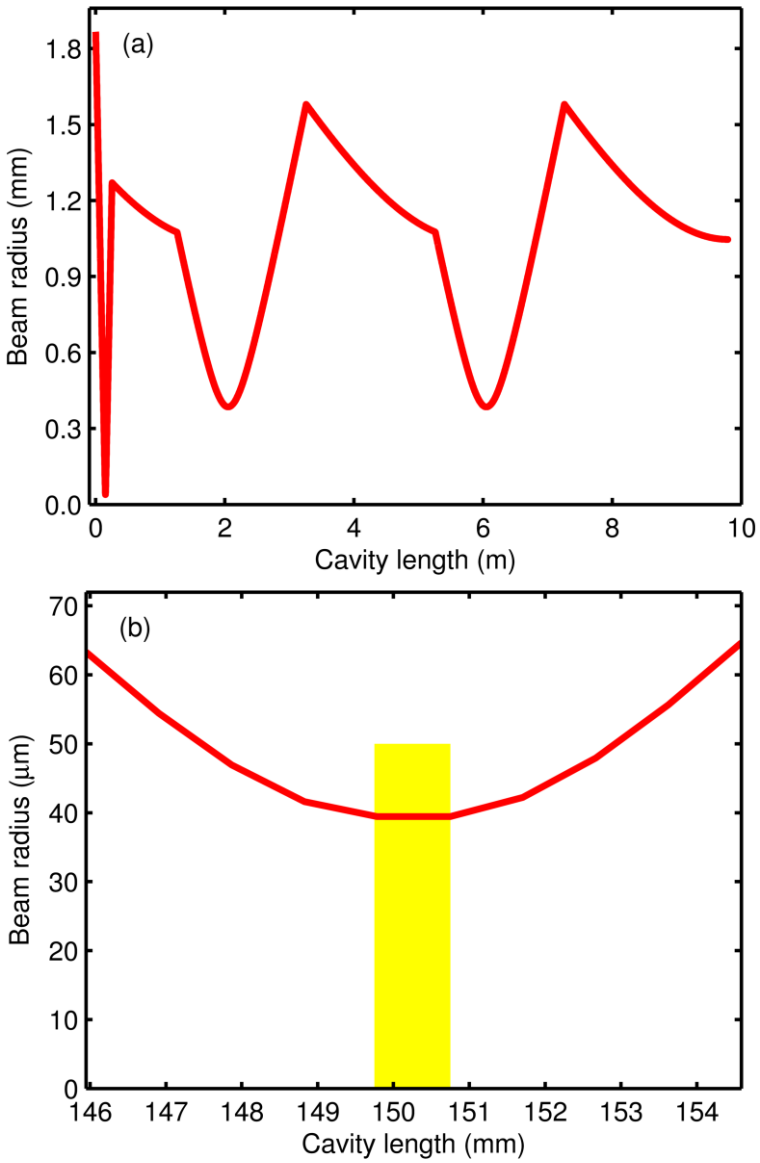

Figure 3.7. (a) Beam profile of the extended OPO cavity with 9.8 m length; c) Close-up into the focusing section through the PPLN crystal. The yellow bar represents the physical crystal position and size.

Synchronous pumping required the OPO cavity length to be matched to the pulse repetition rate of 15.3 MHz, resulting in a total length of 9.8 m, measured between the curved end-mirror (M_1) and the output coupler (M_8). Following the extended-cavity strategies used successfully to scale the pulse energies obtained from Ti:sapphire laser oscillators [26–28], relay imaging was employed similarly. This was implemented using two pairs of 2000 mm radius concave mirrors ($M_{3/4}$ and $M_{5/6}$) to achieve a long resonator, which was stable and produced an intracavity beam with a diameter not exceeding 3.6 mm at any point in the cavity. The calculated beam profile is outlined in Figure 3.7 a). All mirror-folding angles were small ($< 2°$), minimizing astigmatism caused by the curved mirrors.

The mirrors used for the resonator were obtained from Quality Thin Films (QTF) with a custom-made coating offering good transmission of approximately > 98% at the pump wavelength combined with excellent reflectivity at the signal wavelength covering 1250 to 1530 nm. The measured transmission curve is shown in Figure 3.8.

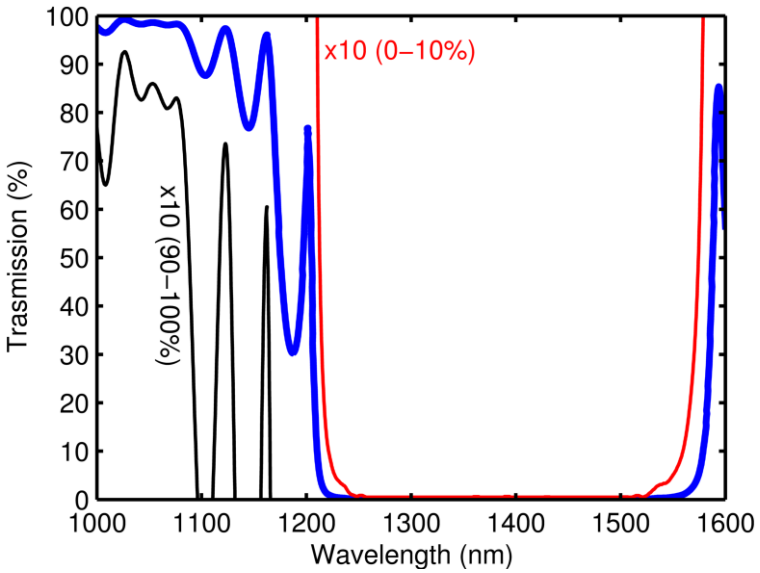

Figure 3.8. OPO cavity mirror high reflection coating curve. The blue curve belongs to the 0 - 100% scale. The black and red curves show a resolution enhancement of a factor 10 covering 90 – 100% and 0 – 10% respectively.

3.4 Optical parametric oscillator performance characterizations

3.4.1 Pump depletion and efficiency

The optimal output coupling was examined by recording the maximum extractable average power for output coupler transmissions of 10%, 22%, 35%, and 40%, which led to output powers of 980 mW, 1080 mW, 1040 mW, and 982 mW, respectively. These values were used for a Rigrod analysis [35], which allowed us to determine the output coupling value for maximum power extraction. Following the Rigrod analysis in Siegman [36], the total output power P_{out} is related to the unsaturated single-pass gain G_0 and the cavity losses $1 - R_1$ by the analytical expression

$$P_{out} = \frac{T_2 P_{sat}}{(1 + r_2/r_1)(1 + r_2 r_1)} \left(ln\, G_0 - ln\left(\frac{1}{r_1 r_2}\right)\right), \qquad 3.1$$

where $r_1 = \sqrt{R_1}$ and $r_2 = \sqrt{R_2}$ are the amplitude reflection coefficients and $T_2 = 1 - R_2$ is the output coupler transmission. The analytical expression was used to obtain a best-fit between the experimental and analytical results using an algorithm based on the Nelder-Mead simplex method [37] (*fminsearch* function in Matlab).

From the fit, we obtained for P_{sat} = 2.165 W, and G_0 = 2.262, while the residual cavity losses of 7.4% are in satisfactory agreement with the estimated 11% losses implied by the pump depletion and extraction efficiency results presented in Figure 3.10. From these values, optimum output coupling was inferred to be at 24.3%, which is close to the 22% used for the measurements presented in this chapter.

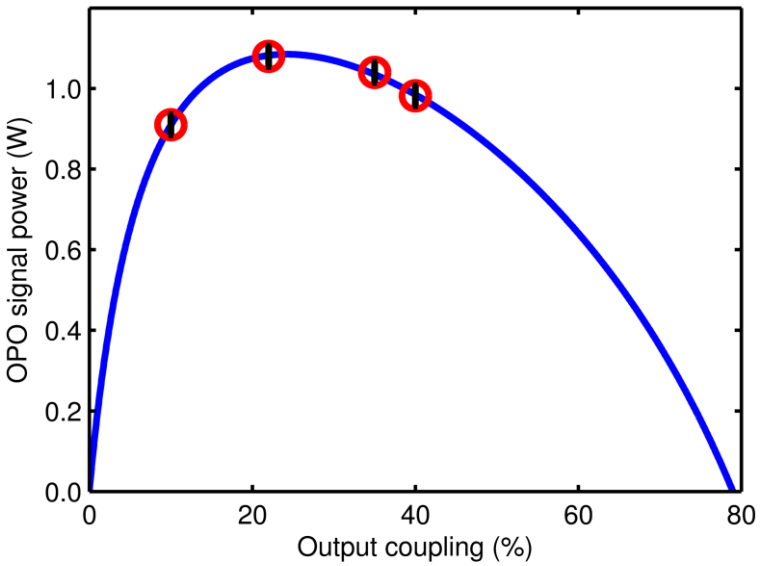

Figure 3.9. Output coupler optimisation based on four different coupling results with the maxima at 24.3%. The error markers indicate a range of ±2%, representing the uncertainty of the power meter used for the measurements.

The pump depletion was investigated under maximum output power and 22% output coupling, and a comparison of the pump spectra measured after the crystal with the OPO oscillating and blocked is shown in Figure 3.10. Strong depletion was observed between 1057 nm and 1067 nm, with evidence of back-conversion from the signal to the pump at 1056 nm. This back-conversion can be understood as resulting from uncompressible chirp in the wings of the pulse spectrum caused by the self-phase modulation that occurs in the Yb:fibre amplifier. A conversion efficiency based on the difference in the areas under both spectra was calculated to be 36%.

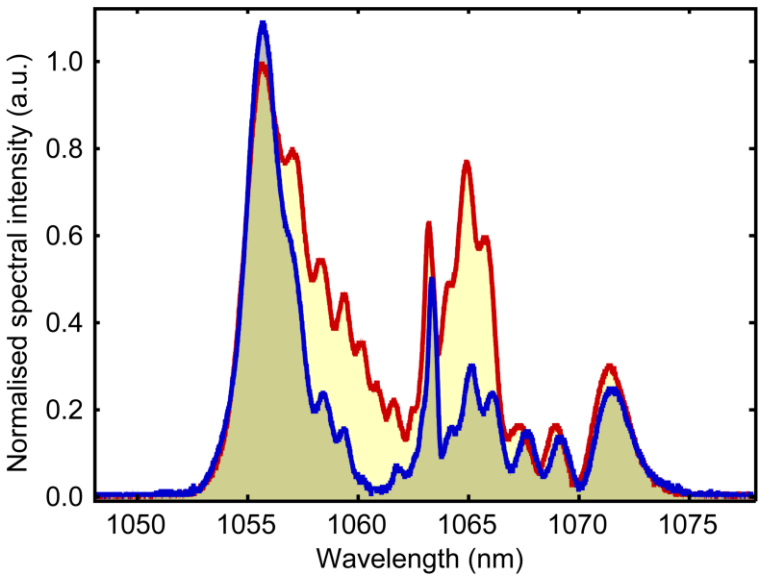

Figure 3.10. Spectra of the depleted pump (grey fill, blue outline) and undepleted pump (yellow fill, red outline). The intensity scale is normalized to the maximum of the undepleted spectrum.

When the OPO was operated with a 22% output coupler, the maximum output power at a centre wavelength of 1535 nm was 1.09 W for a pump power of 6.4 W, implying a signal extraction efficiency of 17.0% and an idler extraction efficiency of 7.6%. The idler efficiency was inferred using the Manley-Rowe relations, taking an idler wavelength of 3.42 µm. The difference in the pump depletion and the total extraction efficiency of 11% indicates the parasitic loss in the cavity. By taking the reflectivity of the cavity mirrors to be 99.7% (due to their operation close to the long wavelength edge), a reflectivity loss for each cavity roundtrip of 4.5% was obtained and a 2% loss at the MgO:PPLN crystal, which can be explained by a 0.5% residual reflectivity at the antireflection-coated faces presented in Figure 3.5. The residual 5.5% losses could be introduced by atmospheric absorption at that wavelength and scattering inside the crystal.

The slope efficiency, measured with a 22% output coupler was determined to 22.2% with an estimated pump threshold of 1.25 W, as indicated in Figure 3.11.

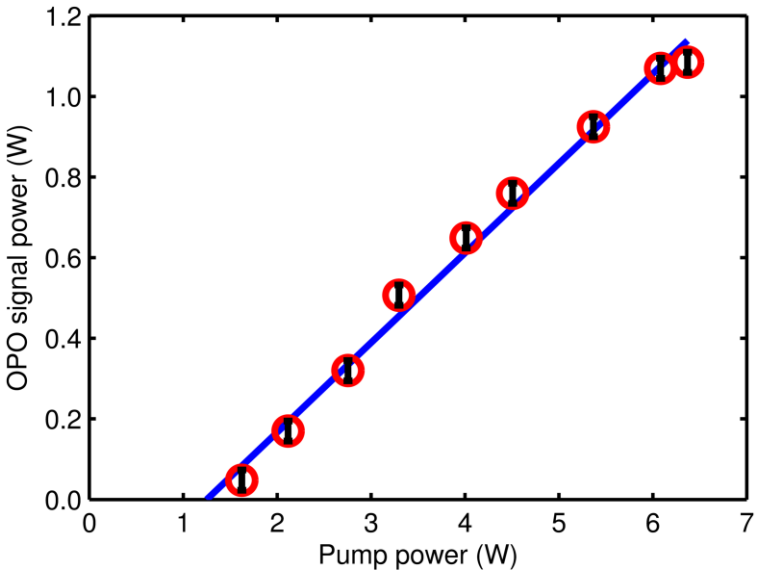

Figure 3.11. Signal output power (solid circles) as a function of pump power for a 22% output coupler, and a linear fit through the data (blue line), extended to cross the abscissa. The slope efficiency was determined to be 22% and the pump threshold was estimated to be 1.25 W.

3.4.2 Intensity noise

The use of an extended cavity for a synchronously pumped OPO raises the question of whether the system may be vulnerable to environmental noise because of the greater number of mirror mounts and longer free-space path travelled by the intracavity beam. By using silicon and InGaAs photodiodes, the intensity noise present on the pump pulses (Si) and the OPO signal pulses (InGaAs) was monitored. Figure 3.12(a) shows the measured power signal and the derived spectral densities of the intensity noise present on both outputs, with the frequency range from 1 Hz to 100 kHz being sufficient to include noise arising from acoustic sources and atmospheric turbulence along the beam path in the cavity. The data in Figure 3.12(a) were recorded without any active cavity-length stabilization, and three independent measurements led to very similar results.

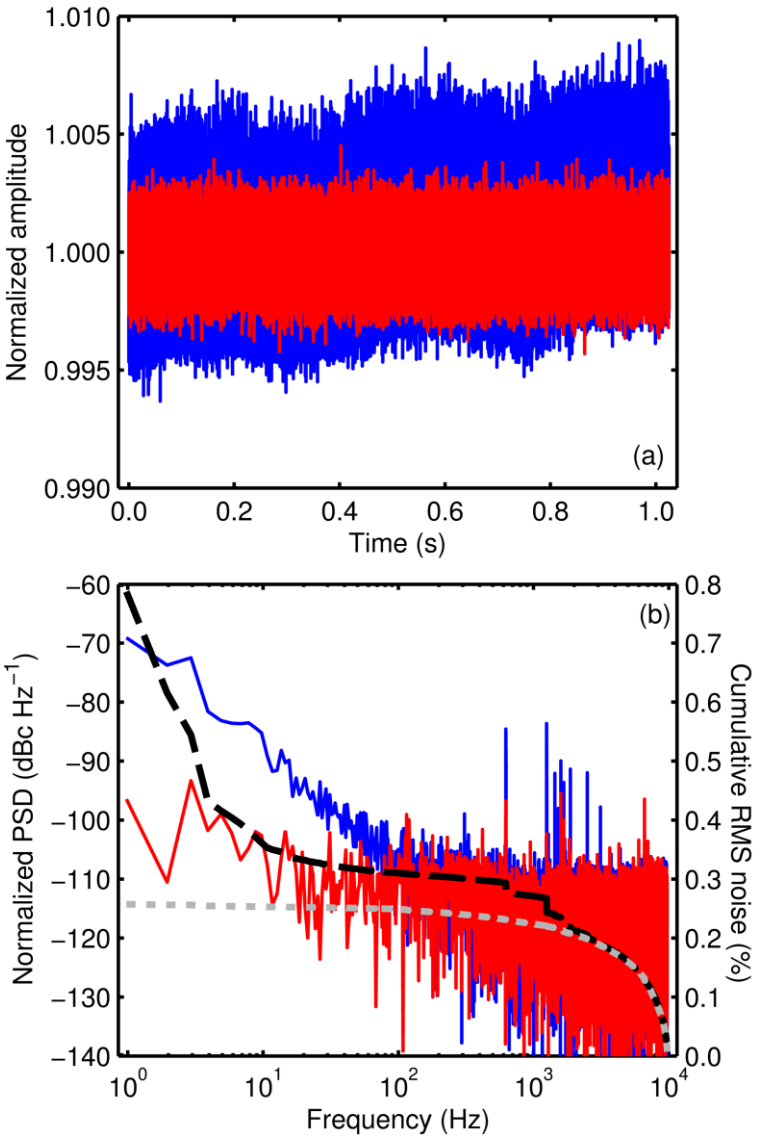

Figure 3.12. (a) The measured pump (red) and OPO signal (blue) outputs, measured with Si and InGaAs photodiodes respectively with their mean output levels normalised to 1 V. (b) Power spectral densities of the intensity noise on the pump (red) and the OPO signal (blue). The right axis shows the cumulative RMS noise for the pump (dotted grey) and the OPO signal (dashed black).

While the noise measurement shows that the OPO pulses possess greater intensity noise than those from the pump laser, the absolute value of the noise is at a low level (<0.1%), and indistinguishable from the pump laser at frequencies higher than those typically associated with acoustic vibrations. Comparison of the cumulative RMS noise shows a division at 1 kHz, increasing at lower frequencies. An implementation of active cavity-length stabilization [38] with a bandwidth of at least 1 kHz is therefore expected to reduce the noise in the acoustic region significantly and such a system is described in

Chapter 4. In a boxed configuration, the output power of the OPO was very stable and only exhibited a slow drift as the lab temperature changed.

3.4.3 Signal pulse characterizations

Characterisation of the signal pulses was performed using interferometric autocorrelation using two-photon absorption in a silicon photodiode [33], while recording the signal spectrum simultaneously with the autocorrelation traces. The spectra of the OPO signal pulses showed significant structure, indicating that their shapes could not be described by the Gaussian or $\mathrm{sech}^2(t)$ intensity profiles commonly used to infer pulse durations from autocorrelation measurements. For this reason, the signal pulse durations were estimated from a fit to the interferometric autocorrelation, based on adding quadratic and cubic spectral phase to the measured spectrum. Figure 3.13(a) presents an interferometric autocorrelation recorded at a signal energy of 72 nJ and corresponding to the spectrum shown in Figure 3.13(d). The autocorrelation shown in Figure 3.13(b) represents the best fit to the experimental autocorrelation obtained by optimizing the amount of quadratic and cubic phase added to the spectrum in Figure 3.13(d). The temporal intensity of the corresponding pulse is shown in Figure 3.13(c), and the red line in Figure 3.13(d) shows the spectral phase of this pulse (where the best fit returned a quadratic phase of -80469 and cubic phase of -1.268×10^8). The duration of the signal pulses inferred using this method was 1.47 ps, which was 1.75 times the transform-limited duration of 840 fs. Although this approach is not fully unambiguous, it allows a better estimate of the pulse duration than can be obtained by a naive assumption of a standard analytic pulse shape.

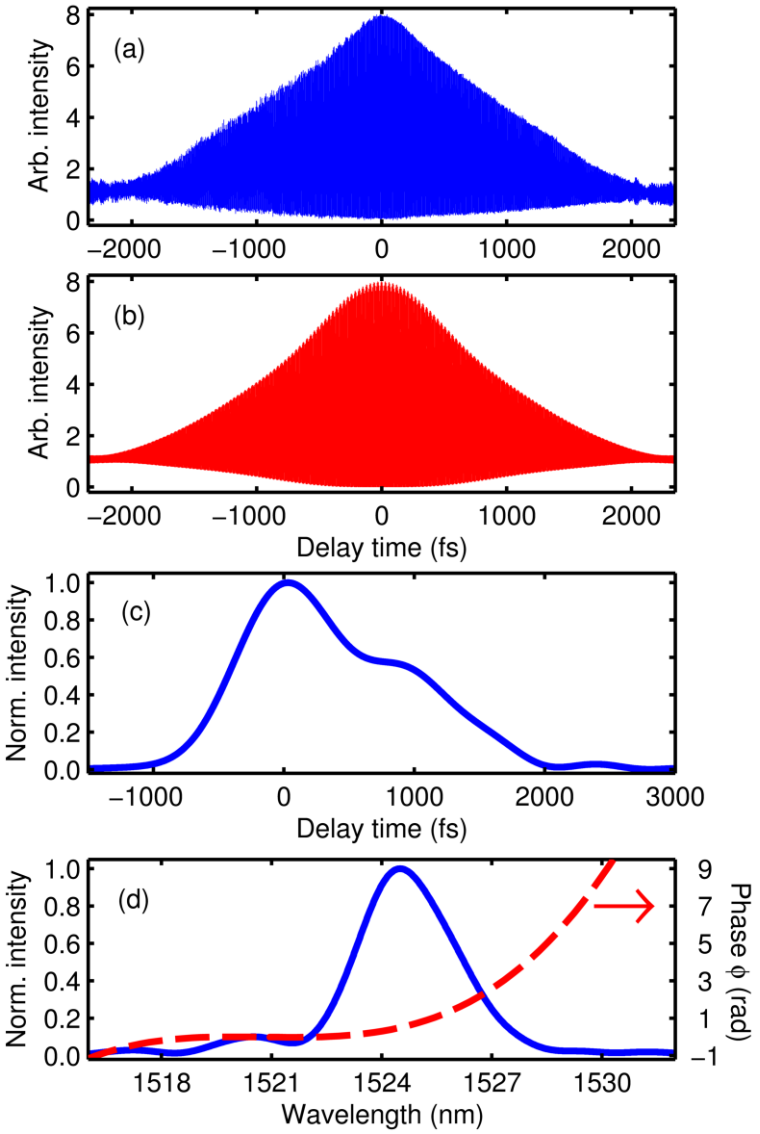

Figure 3.13. (a) Experimental and (b) fitted interferometric autocorrelation, indicating a pulse duration of 1.47 ps. (c) The temporal intensity of the pulse calculated from the measured spectral intensity and fitted phase in (d). Data were obtained at 1080 mW signal power.

The operating regime in which the results of Figure 3.13 were recorded corresponded to one that produced narrowband pulses with a modest amount of chirp, indicated by the fringe coherence prevailing into the wings of the autocorrelation. A second regime was accessible at a longer wavelength by adjusting the cavity length by a small amount. In this configuration, the OPO produced signal pulse energies of 62 nJ, and the corresponding signal autocorrelation and spectrum are shown in Figure 3.14. A broadening of the spectrum was visible (Figure 3.14(d)) with an intensity drop at 1533 nm between two local maxima around 1528 nm and 1537 nm. A similar analysis to that used for the shorter-wavelength signal data implied signal durations of 1.68 ps, a

factor of 4.2 times the transform-limited duration of 400 fs (where the best fit returned a quadratic phase of 1.8776×10^5 and cubic phase of 28653).

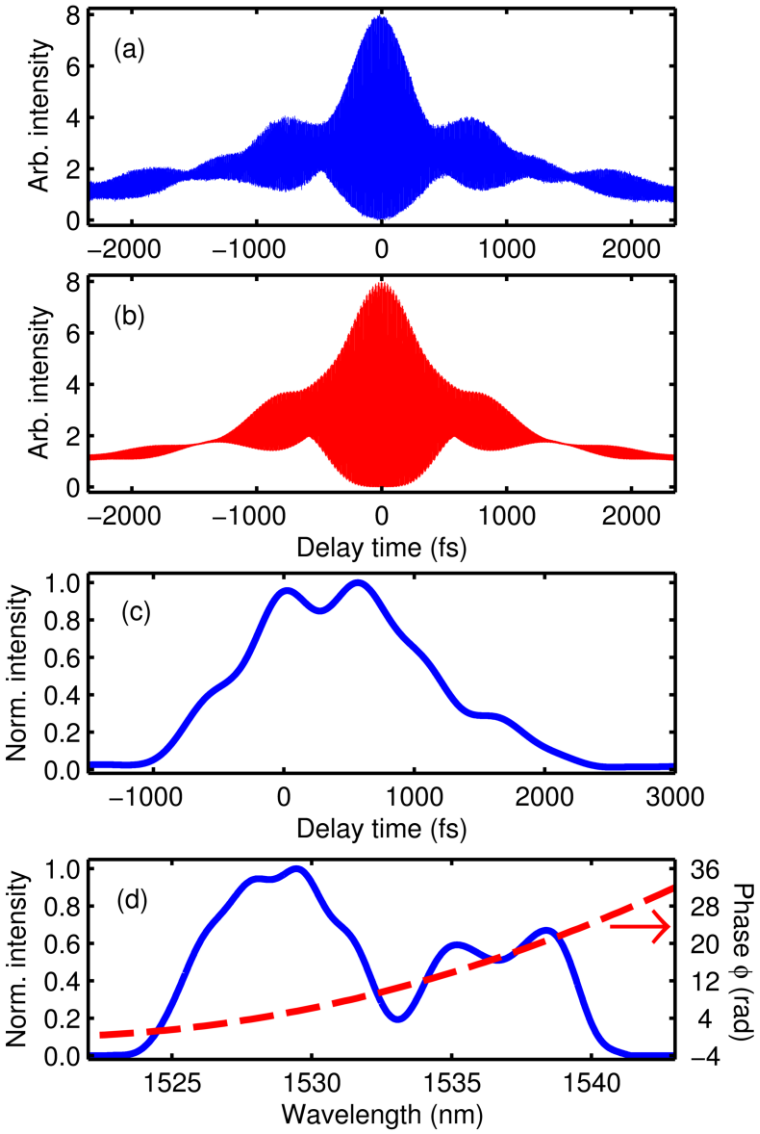

Figure 3.14. (a) Experimental and (b) fitted interferometric autocorrelation, indicating a pulse duration of 1.67 ps. (c) The temporal intensity of the pulse calculated from the measured spectral intensity and fitted phase in (d). These data were obtained at 980 mW signal power.

3.4.4 Beam-quality factor characterisation

The high finesse of the resonator suggests an intrinsic beam quality close to diffraction limit. To quantify these potentials, the beam-quality parameters of the output-coupled beam were measured in both the horizontal (X) and vertical (Y) plane.

The data were acquired by using the scanning knife-edge technique to measure the $1/e^2$ beam radius at regular intervals after a 200-mm focal-length lens. Scanning the knife-edge through the beam in a stepwise fashion produced the data shown in Figure 3.15 where the green symbols indicate remaining powers recorded at positions across the beam. The entire process was performed with an automated stage where several hundred points per plane were taken. The intensities were detected with a bolometric power-meter. Normalization of the acquired trace was most accurate if the measurement process was initiated with obscured beam, moving the knife out of the beam. This approach ensured that low-intensity readings were more accurate since the calorimetric detection scheme of the power meter suffered from a long time constant in order to dissipate the heat accumulated during the previous taken measurements. For both, the x and y planes, 21 knife-edge scans were recorded, at positions from 50 mm before the focus to 50 mm after the focus. Figure 3.15 shows an example of one knife-edge measurement, indicating an excellent overlap of the measure d data and the fitted error-function. All measurements were recorded at maximum output power.

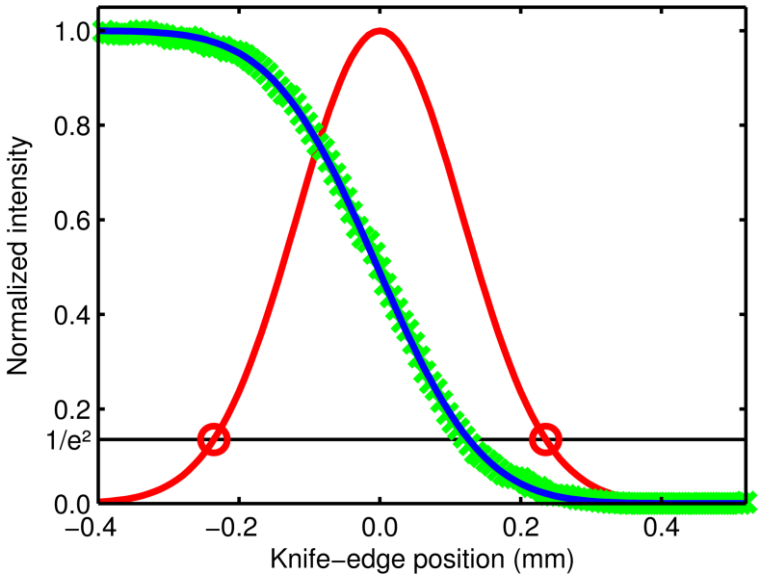

Figure 3.15. Example of a single knife-edge measurement (green X) and the fitted error-function (blue line) used to determine the Gaussian intensity distribution (red line) and the $1/e^2$-beam radius.

Figure 3.16 presents the experimentally acquired beam-radii data (red circles) and a Gaussian beam propagation (blue line) fitted with an M^2-value giving the minimum

RMS error with the data. The beam propagation fit showed the expected nearly diffraction limited beam quality of $M_X^2 = 1.13$ and $M_Y^2 = 1.07$.

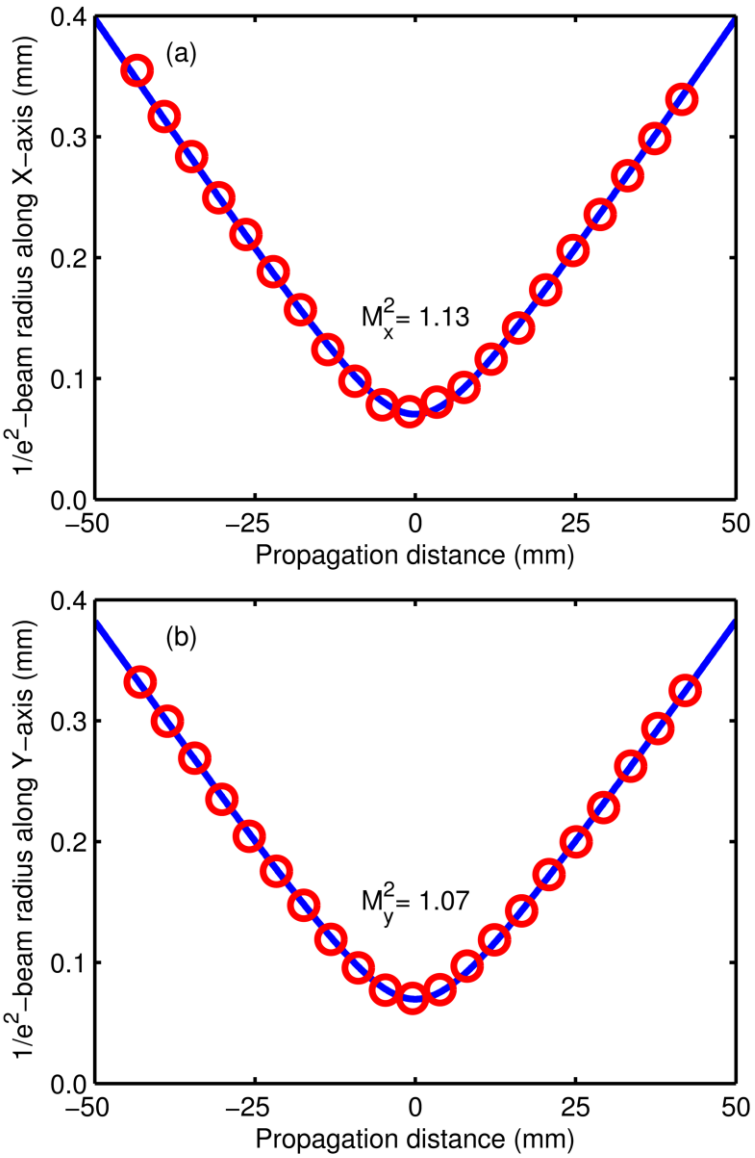

Figure 3.16. (a) Horizontal and (b) vertical beam radius measurements (red circles) and fit to an M^2-corrected Gaussian-beam propagation equation (blue lines), with M^2 = 1.13 (horizontal) and M^2 = 1.07 (vertical).

3.5 Conclusions

A high-energy extended-cavity MgO:PPLN optical parametric oscillator, synchronously pumped by a femtosecond Yb:fibre laser was demonstrated and characterised. The oscillator operated at a signal wavelength of 1530 nm with a repetition-frequency of 15.3 MHz (9.8 m length) achieved using intracavity relay-imaging optics. The signal

pulses had an average power above 1.0 W, durations of around 1.5 ps and energies greater than 70 nJ, which represents the highest directly output coupled pulse energy from an OPO to date. A novel aspect of the OPO is the incorporation of relay imaging, enabling a stable resonator at very low repetition rates, which opens up the use of very high pump pulse energies for energy and power scaling.

The combination of the pump-source and the cavity design presented in this chapter, created severe stability problems due to back reflections into the fibre laser, causing the pump source to fail frequently even with optical isolators in place. This problem motivated a redesign of the OPO cavity to reduce the back reflected power to a minimum.

The OPO design presented in Chapter 5 shows the implementation of this improvement in a redesigned cavity, which also included the active cavity stabilisation introduced in the next chapter.

Chapter 4 - Wavelength stabilization of a synchronously-pumped optical parametric oscillator: optimizing proportional-integral

4.1 Introduction

This chapter describes a formal approach on how to implement wavelength stabilization of a synchronously pumped ultrafast optical parametric oscillator using proportional-integral feedback control. Closed-loop wavelength stabilization was implemented by using a position-sensitive detector as a sensor and a piezoelectric transducer to modify the cavity-length of the oscillator. By characterizing the frequency response of the loop components, a predictive model of the controller was found, which showed formally that a proportional-only feedback was insufficient to eliminate the steady-state error, consistent with experimental observations. The optimal proportional and integral gain coefficients were obtained from a numerical optimization of the controller model that minimized the settling time while also limiting the overshoot to an acceptable value. Results are presented showing effective wavelength and power stabilization to levels limited only by the relative intensity noise of the pump laser. The final part of the chapter evaluates the principles of dither-locking as a further means of cavity stabilization. After this alternative technique has been considered in depth, a comparison between the two approaches is given.

4.2 Cavity-length stabilization in ultrafast optical parametric oscillators

Synchronously pumped ultrafast optical parametric oscillators (OPOs) are increasingly finding uses in applications like broadband spectroscopy [39], chemical and biological studies [40] remote sensing [41], multi-photon microscopy [42], and nonlinear material analysis [43]. In many such applications, the stability of the pulse duration, wavelength, repetition frequency, and the output power are of critical importance. In comparison to a conventional synchronously-pumped laser (e.g. dye laser), the output of a synchronously-pumped OPO responds differently to changes in the cavity-length mismatch with the pump laser. The gain storage intrinsic in a synchronously-pumped

laser allows it to tolerate a small repetition frequency mismatch, but typically at the expense of an increase in the pulse duration. In contrast, a synchronously pumped OPO responds to a cavity-length mismatch by adjusting the wavelength of the resonant pulses to maintain synchronism by utilizing the group-delay dispersion in the cavity. The wavelength-dependent gain and loss characteristics of the OPO cavity can mean that such a wavelength change, in turn, modifies the output power of the system. Therefore, changes in the pump-pulse repetition frequency, or environmental fluctuations that modify the optical path length of either the pump or OPO cavities, lead directly to output power instability.

In a synchronously pumped OPO, the fluctuations of the pulse timing, pulse duration, wavelength, and power are strongly correlated to each other, coupled by the intracavity group-delay dispersion and nonlinear effects like self-phase-modulation. Actively stabilizing a cavity to suppress any one of these fluctuations leads to a corresponding reduction in the correlated fluctuations, limited ultimately by the shot noise level.

In general, an active feedback scheme pre-supposes a linear and stable error signal. A direct way to stabilize the power level of any source could be to monitor the output power and adjust the cavity to maintain this power level, for example using a dither-locking approach. This technique is explained in more detail at the end of this chapter.

In synchronously-pumped lasers, the sensitivity of the pulse repetition frequency (PRF) to cavity length can be exploited to provide an error signal, either by comparing the PRF to an electronic oscillator [44,45] or to the PRF of a reference cavity [46]. Such a scheme has been successfully implemented to reduce the jitter in a mode-locked Nd:YAG laser [44] and to reduce the amplitude noise of a coupled-cavity colour-centre laser [46].

An alternative cavity stabilization approach based on wavelength fluctuations was reported for a synchronously-pumped dye laser in 1986 [47], in which a cavity length change leads to a small wavelength shift. Two photodiodes were used to monitor the intensity on both sides of a spectrally-dispersed beam, and the difference in their voltages was used, via a simple electronic circuit, to adjust the cavity length

accordingly. Figure 4.1 (a) illustrates the basic idea of this approach further. Ultimately, this approach is limited by the fact that the spectral intensity distribution of the circulating pulses often contains fine structure that misleads the controller [48] and indicated with the red trace in Figure 4.1(b). The technique was successfully adapted from dye laser cavities into a femtosecond OPO, in which feedback based on output wavelength was used to operate the system reliably in the regime of the shortest pulse durations [13].

Nevertheless, the dual photodiode approach implemented in an OPO was also problematic in situations where the spectral shape of the pulses was irregular. A solution to this issue was presented by Butterworth et al [38], who replaced the two balanced photodiodes with a one-dimensional position-sensitive detector (PSD). Rather than only considering the slopes on either side of the pulse spectrum, the first order moment of the entire spectrum provided the error signal. This embodiment provided a continuous monitor of the OPO wavelength, independent of the incident power level and the shape of the pulse spectrum. In addition, it offered a simple implementation into an existing system and a convenient means of controlling the OPO wavelength via a feedback circuit, which actuated a piezoelectric transducer (PZT), attached to one of the cavity mirrors. Figure 4.1 (b) shows the principles of continuous detection of the spectrum by taking its first order moment. The blue line represents a continuous Gaussian intensity distribution centred at 1520 nm. In contrast, the red trace was recorded with an OPO operating close to zero cavity net dispersion, showing a heavily modulated spectrum due to self-phase modulation with its centre wavelength at 1520 nm.

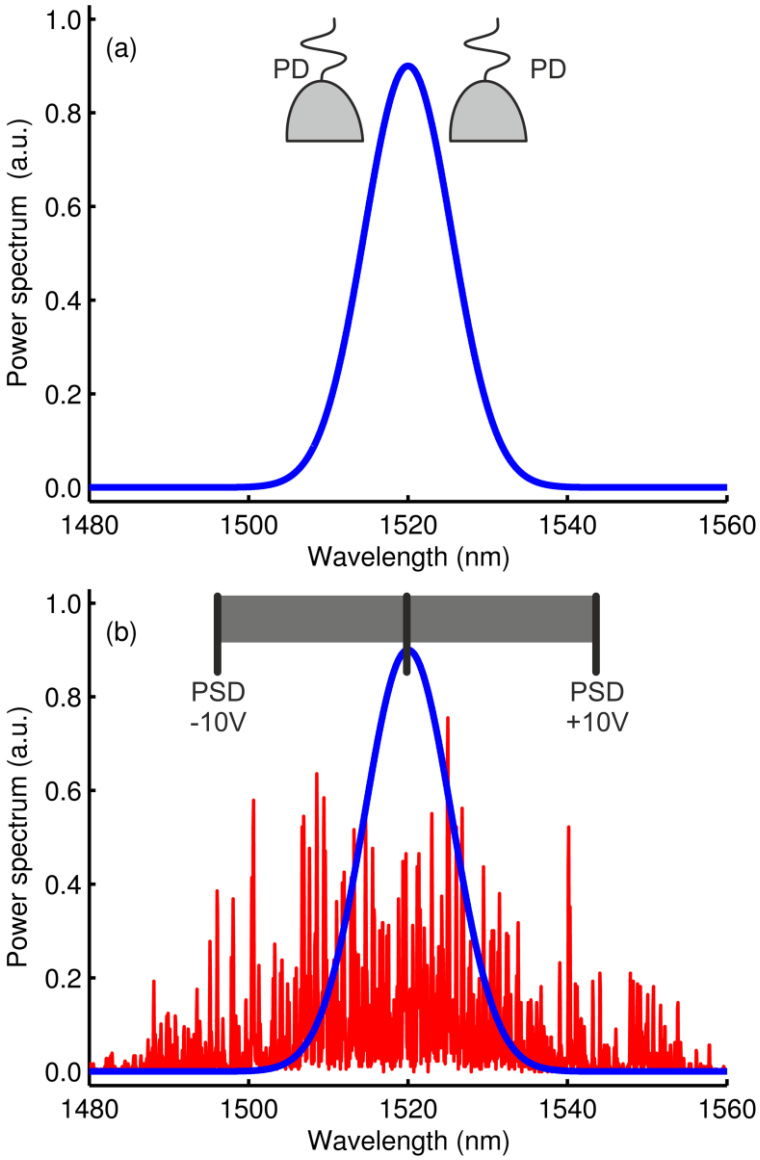

Figure 4.1. Principles for (a) a 'balanced detector' approach monitoring the edges of a Gaussian intensity spectrum (blue line). (b) a continuous evaluation with a 'position sensitive detector' scheme offering a more robust feedback signal for distorted or noisy spectra (red trace).

In the following chapter, a formal approach is described as to constructing and optimizing the wavelength stabilization of a synchronously-pumped OPO, based on the method described in [38]. The description shows how, by characterizing the tuning behaviour of the OPO and the frequency response of the components forming the feedback circuit, it is possible to optimize the design of the control system.

4.3 Optical parametric oscillator configuration

The OPO layout is presented in Figure 4.2. It was based on an MgO-doped periodically-poled lithium niobate (MgO:PPLN) crystal (X) with a length of 1 mm and pumped by a commercial Yb:fibre laser (P) operating at a centre wavelength of 1064 nm with a pulse-repetition frequency of 15.3 MHz. The pump beam was focused into the OPO cavity by a 100 mm-focal-length lens (L_1). The OPO resonator was based on an asymmetric "V-cavity" design, with the focusing section around the crystal. Further details of the setup were previously provided in chapter 3.3 on page 49.

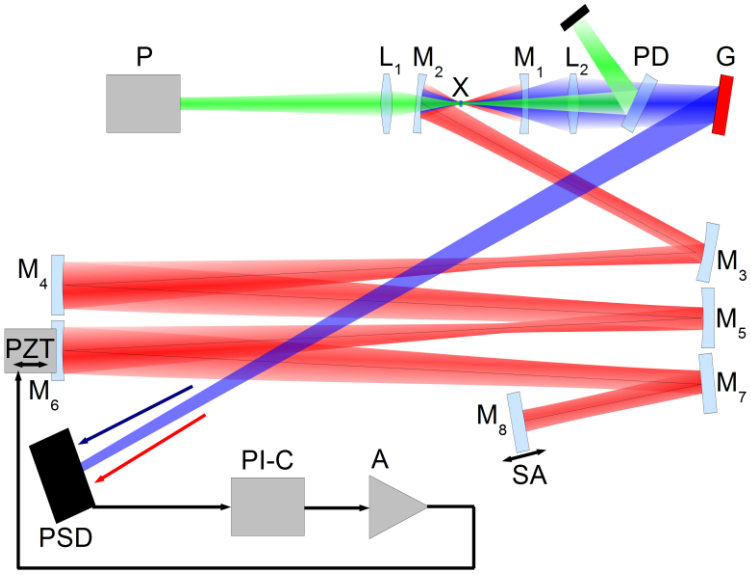

Figure 4.2. Schematic of the OPO cavity, illustrating the collection of the second-harmonic beam used for wavelength stabilization (blue). The green beam represents the pump and the red beam shows the OPO signal (optical components are explained in the text).

To operate a cavity with such a free-space length in a stable fashion, active compensation of changes caused by temperature fluctuations or acousto-mechanical disturbances is essential. By introducing the cavity stabilization into the existing OPO cavity, we followed an approach similar to that reported by Butterworth [38], in which the output beam is spectrally resolved on the surface of a PSD. The PSD used in our work (Hamamatsu S3932) was silicon based and was therefore limited to a wavelength range of 320 - 1100 nm [49], which made direct detection of the 1.5 µm OPO signal pulses impossible. A solution was found by taking advantage of the non-phase matched second-harmonic generation light at 765 nm. This light leaked through the end mirror

M1 as a divergent beam that was readily collected by using a 250-mm-focal-length lens (L_2) 100 mm after the cavity mirror M_1. The light was spectrally dispersed using a 1200 lines/mm grating (G), and the lens L_2 was adjusted to form a line-spectrum on the PSD after a propagation distance of 2.2 m. To dump the residual pump power an additional dielectric mirror (PD) with high reflectivity at 1064 nm was used as a filter.

The horizontal displacement of the diffracted beam was detected by combining the PSD with a signal processing circuit (Hamamatsu C3683-1), which provided a monotonic output voltage from -10 V to +10 V in respect to a displacement across the 12 mm-wide silicon sensor. This voltage was directly utilized as the error signal for the locking circuit. The incident light level was maintained within the recommended limits (1VDC < Vrec < 10VDC) through a neutral density filter (ND1) attached to the front of the sensor. In addition, this reduced the ambient light signal to a suitably level (~10 mV). The integrated power incident over the entire sensor was accessible via a dedicated pin on the processing circuit. Furthermore, this output was used to monitor whether the OPO was oscillating or not.

To adjust the cavity length, one of the mirrors (M_6) was mounted to a PZT (Piezomechanik, STr-25/150/6). The displacement of the transducer was limited to 6 µm for 150 V. To drive the device a high-power amplifier (Newport µDrive) with the high-bandwidth mode enabled was used.

4.4 Wavelength stabilization and feedback control

Following the approach of [38], the error signal provided by the PSD unit was returned to the PZT using an ordinary proportional-gain circuit, however the closed loop either induced oscillation or settled at a value far from the target set-point (a large steady-state error, SSE). Using only proportional gain, it was found to be impossible to achieve active cavity-length stabilization with performance similar to the arrangements previously reported [13,38,47].

A proportional-integral (PI)-controller was implemented to overcome the observed problems. In this scheme, the integral part is used to force the controlled system to the

desired value by cumulating the residual error between set-point and actual value. The disadvantage of this error accumulation approach is that it can result in unstable behaviour or poor dynamic response if the parameters are not carefully chosen. For these reasons, a model of the entire feedback loop was created to provide a better understanding of the overall system behaviour and to facilitate the choice of parameters needed to give stable operation. The model required, as input parameters, the frequency-dependent responses of the components used in the optoelectronic feedback loop. Once configured, a final optimization procedure of the closed-loop circuit enabled the optimal gain values of the PI-amplifier to be found, resulting in a stable and rapid feedback response and an understanding of the previously observed problems caused by using only proportional gain.

The gain of the feedback loop can be defined as the change in the PSD output voltage in response to a change in the voltage applied to the PZT. We obtained this parameter by applying a constant saw-tooth signal (frequency 1 Hz, and peak-to-peak amplitude of 40 V about a mean voltage of 75 V) to the PZT. The direct signal obtained from the PSD was observed to follow closely the saw-tooth signal, with a peak-to-peak value of 4 V over the corresponding wavelength range, despite the shape and bandwidth of the OPO spectrum experiencing significant changes across this range. This measurement confirmed the robustness of the PSD-derived error signal and implied a low-frequency sensor gain of S = 0.1 dB. In Figure 4.3 the two acquired signals are overlaid with each other. The falling slope shows a mismatch between applied voltage and physical response of the PZT, which can be contributed to the intrinsic hysteresis of the transducer. Due to the optical feedback loop, any hysteresis was cancelled through the integral part of the controller and introduced therefore no additional error.

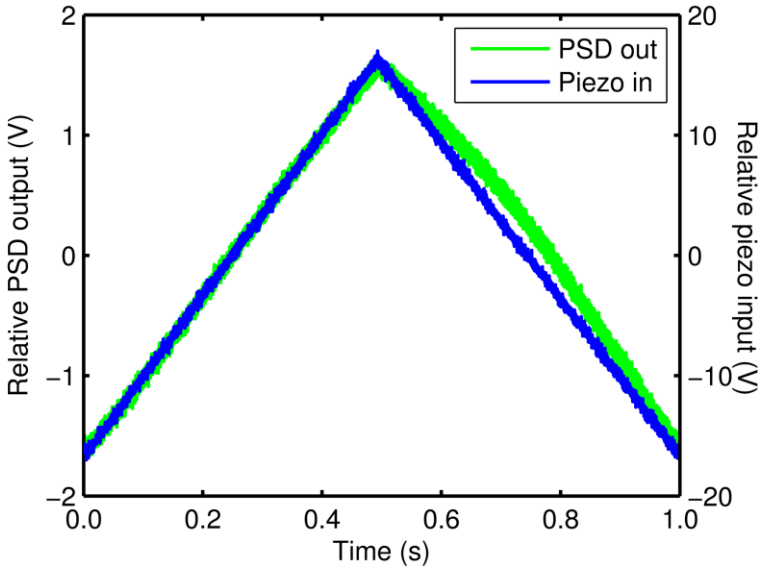

Figure 4.3. Comparison between position sensitive detector read out (green, left ordinate) and the applied piezo voltage (blue, right ordinate) to characterise the open-loop gain and linearity. The plot clearly highlights the mismatch caused due to piezo hysteresis.

Physically, the sensor gain is a measure of the rate of cavity-length tuning and is inversely proportional to the intra-cavity group-delay dispersion according to [50],

$$\frac{d\lambda}{\mathrm{dL}} = \frac{\lambda^2}{2\pi c^2}\left(\frac{d^2\phi}{d\omega^2}\right)^{-1}, \qquad 4.1$$

where L is the cavity length, λ is the centre wavelength of the resonant pulses, c is the speed of light in vacuum and $\frac{d^2\phi}{d\omega^2}$ is the intra-cavity group-delay dispersion. The polarity of the sensor gain indicates whether the net intra-cavity group-delay dispersion is normal or anomalous, and its absolute value reflects the magnitude of the intra-cavity group-delay dispersion. For example, an OPO containing a long crystal and no dispersion compensating optics would be likely to have a large value of intra-cavity group-delay dispersion, which would lead to slow cavity-length tuning and a low sensor gain. In this case, a large value of P (proportional gain) would be required for stable locking, which is illustrating that P is approximately proportional to the intra-cavity group-delay dispersion.

The frequency-dependent contributions to the loop gain arise from two sources: the high-frequency roll-off of the PSD sensor, and the resonance and high-frequency roll-off of the PZT. Dealing first with the PSD, the sensor was subject to a first-order frequency response with a cut off at $f_c = 1$ kHz. After including this, the sensor response could be represented in Laplace notation as,

$$\frac{F(s)}{Y(s)} = \frac{S_g}{1 + \frac{s}{2\pi f_c}}, \qquad 4.2$$

where $F(s)$ is the feedback signal, $Y(s)$ is the piezo voltage and S_g is the steady state gain. The frequency behaviour was influenced by the denominator where a rising frequency results in a decreasing amplitude.

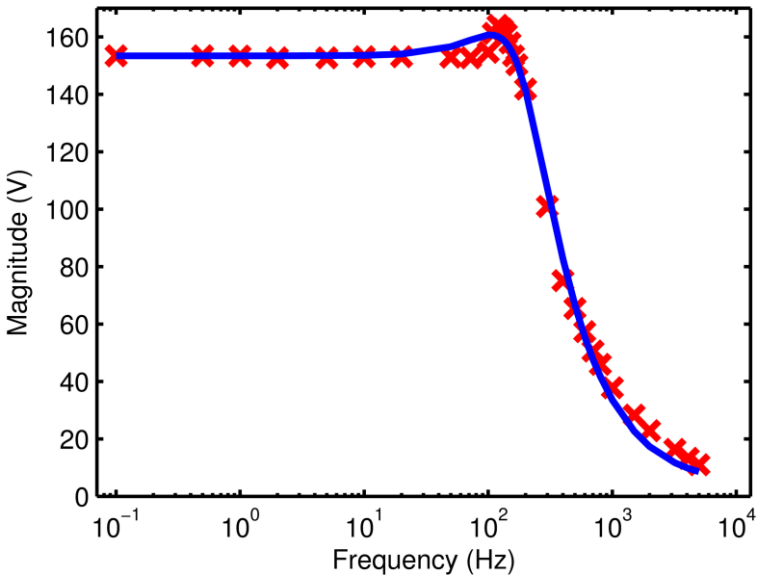

Figure 4.4. Experimentally obtained Bode plot (X-symbols) showing the combined frequency response of the Newport µDrive amplifier, PZT and attached mirror. The solid curve is a least-squares fit to the BVD-model with the equivalent circuit shown in Figure 4.5.

In order to generate a frequency-dependent model for the combination of the high-voltage amplifier, piezo transducer, and the OPO mirror, a measurement of the peak-to-peak voltage magnitude across the PZT was performed for frequencies from 0.1 Hz to 5 kHz. The experimental values are depicted as red crosses in Figure 4.4. The standard

IEEE PZT equivalent circuit – also known as the Butterworth-Van-Dyke (BVD) model [51] – provided a satisfactory fit to the experimental values (Figure 4.4, blue line). The model is outlined in Figure 4.5 where the amplifier is represented as a source of constant gain G (30.1 dB), with a frequency-dependent output impedance of R_i (32.2 Ω) and L_i (56.3 mH). The oscilloscope used for the measurement is represented by the resistor R_p (1 MΩ). All components inside the grey shaded area represent the PZT equivalent circuit (BVD) model. This part of the model consisted of C_p (244.9 nF), representing the parallel capacitance of the PZT, and R_s (79 Ω), L_s (1.4 mH), and C_s (12.1 µF) as an electrical proxy for the mechanical resonant frequency.

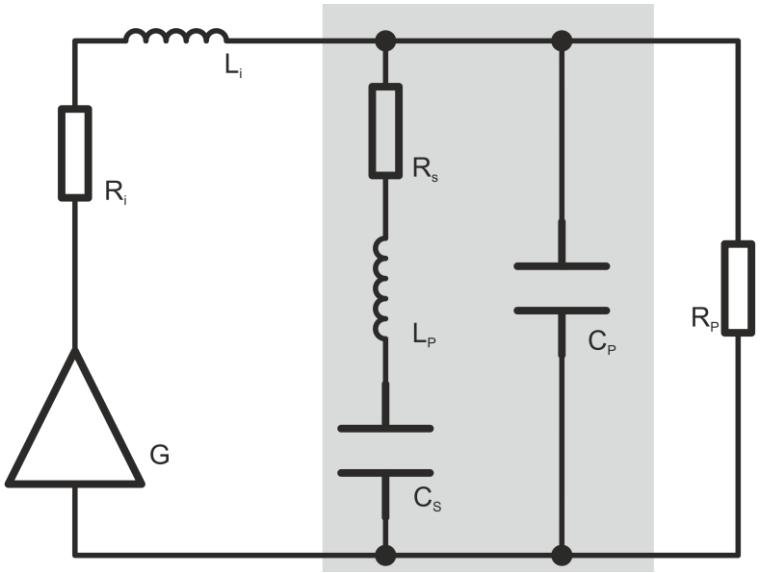

Figure 4.5. Equivalent circuit schematic of: amplifier (G, R_i, L_i); BVD-model (R_s, L_p, C_s, C_p) for the Piezo transducer; the Oscilloscope input impedance R_p.

This resonance is responsible for an effective increase in the mirror displacement for constant input amplitude. The PZT voltage can be obtained by considering the circuit in Figure 4.5 as a voltage divider, in which the output of the idealized amplifier is presented across an internal impedance, Z_i, and an external load (the PZT) of Z_{out}:

$$|V_{out}| = \left| \frac{Z_{out}}{Z_i + Z_{out}} G \right|. \qquad 4.3$$

The impedance of the PZT is given by the BVD model as,

$$Z_{out} = \left[\frac{1}{R_s + i\omega L_s + \frac{1}{1\omega C_s}} + i\omega C_p + \frac{1}{R_P} \right]^{-1} , \qquad 4.4$$

in addition, the amplifier output impedance is,

$$Z_i = R_i + i\omega L_i \, . \qquad 4.5$$

The values for the components previously mentioned were obtained by a least-squares fit of Equation 4.3 to the experimental data, and resulted in the blue curve shown in Figure 4.5. These values were used in the loop model to represent the response of the PZT in combination with the amplifier. The entire system is denoted as the plant in Figure 4.6.

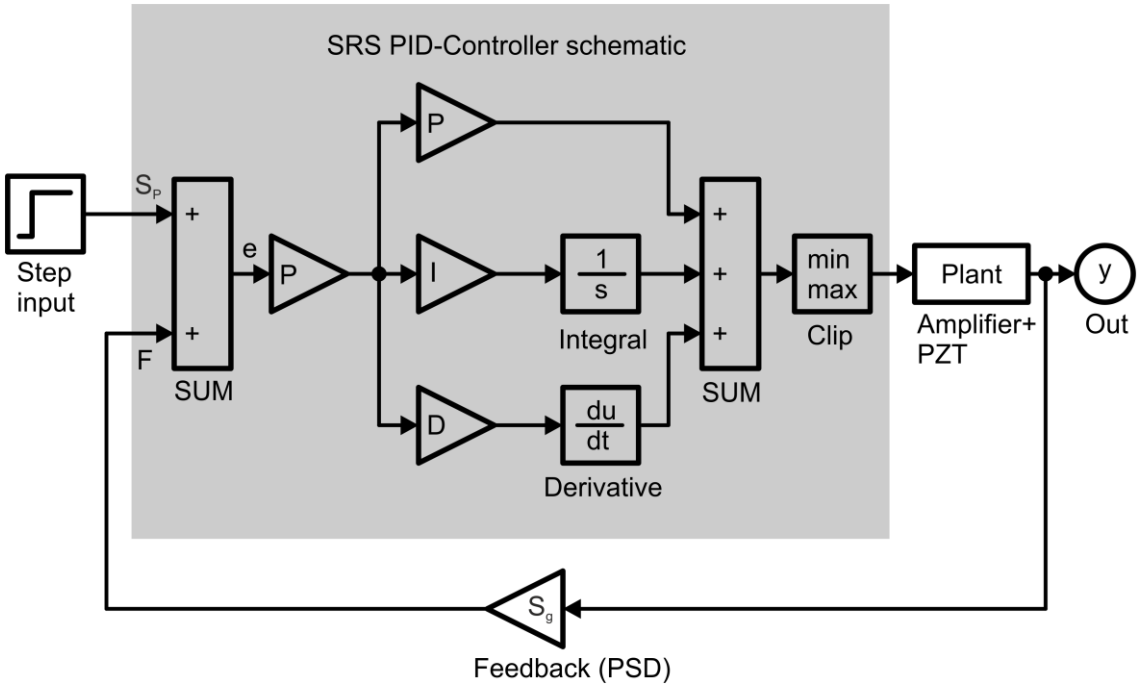

Figure 4.6. Model used for the PID-controller simulation and optimization. The components inside the grey area represent the controller, while the values for P, I, and D correspond to the real values applied to the device. The plant represents the amplifier and PZT-model with the Bode-response as depicted in Figure 4.4.

As the core of the loop, a proportion-integral-differential (PID) controller was introduced in the model, and corresponded to an equivalent experimental PID-

Controller (Stanford Research Systems, SRS SIM960). The experimental parameters, adjustable on the controller front panel, were represented in the model as P (proportional gain), I (integral gain) and D (derivative gain) and related the error signal e with the PZT voltage u(t) according to,

$$u(t) = P\left[e + I\int e\,dt + D\frac{de}{dt}\right]. \qquad 4.6$$

The error signal e is derived from the difference between the desired set point S_P and the feedback signal F obtained from the PSD sensor as:

$$e(t) = S_P(t) - F(t). \qquad 4.7$$

This error becomes zero as soon as the PSD sensor provides the same value as some pre-defined set point. The bandwidth of the experimentally used controller was limited to a frequency of 100 kHz. This frequency was considered in the model by setting the algorithm sampling step width dt to a corresponding rate.

The error between a desired set point and the actual final value of the controlled system is referred to the steady state error (SSE). This is used as a measure of how well a feedback loop corrects a constant input disturbance (e.g. how close it matches a unit step response (S_P)). For instance, if the response to a unit step is 0.8 than the error is 0.2 and the system is said to have a 20% SSE. Deriving the SSE of a closed loop system can be done in the frequency domain [52]. By considering a closed loop, the output value $Y(s)$ is given by the residual error $E(s)$, controller gain P, and the gain of the controlled system $G(s)$ as,

$$Y(s) = E(s)P\,G(s), \qquad 4.8$$

and applying the gain of the feedback sensor $S_g(s)$ with $Y(s)$, the error is now defined by

$$E(s) = S_P(s) - Y(s)S_g(s) \ . \qquad 4.9$$

By substituting Equation 4.8 into Equation 4.9 and considering only the steady-state gain values by applying the final value theorem($\lim_{s\to 0} E(s)$), the SSE can be expressed as,

$$SSE = \frac{S_P}{1 + PGS_g} \ . \qquad 4.10$$

For a constant set-point input of $SP = 1$, and system constants given as $P = 0.3, G = 30.1$, and $S = 0.1$, a SSE of 52.5% was calculated. This was in good agreement with the experimentally observed response obtained in the absence of integral gain and with a proportional gain of 0.3. The simulated response settled on the same steady state value and presented in Figure 4.4 by the dashed red line. Experimentally, increasing the gain further caused the system to oscillate. This oscillatory behaviour of the system was not observed in the simulation but can be attributed to the incomplete model of amplifier and PZT. As a simplified approach for maximum proportional gain, the net-gain, hence the product of P, G and S, must stay below 125%, and for a robust system should be not above 100% [52]. Since the controller allows gain adjustment between 0.3, 0.4 or 0.5 as smallest intermediate steps, 0.3 (90%) was considered as a suitable compromise.

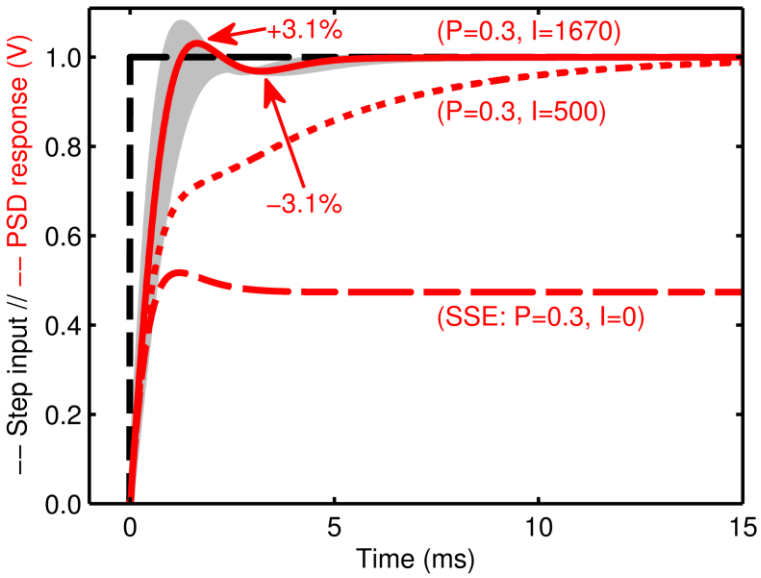

Figure 4.7. Simulated responses of: Optimized PID-controller values (red solid line); with a third of the ideal I value (red dotted line); and the steady state error corresponding to using only a P-controller (red dashed line). The grey area represents the response obtained for $0.2 < P < 0.45$.

To optimize the controller parameters, a maximum system overshoot of 125% was used as an acceptable limit. The optimization of the controller parameters was performed by finding the first point where the measured value remained in a band of ±3.1% of the desired value, and led to an integrative parameter of $I = 1670$. The optimized system response is plotted as solid red line in Figure 4.7, while the grey band corresponds to a variation of proportional gain between 0.2 for the lower edge and 0.45 for the upper edge. The dotted line corresponds to a system response with a third of the optimum integral gain only and led to settling-time a factor of three slower than the best value.

The additional derivative gain was not found to improve the system response due to limited gain adjustment and was therefore set to zero (D = 0). In general, adding a derivative gain allows a certain increase for the proportional gain. Accordingly, if the P, I, and D values are chosen carefully, a further improvement of the response can be possible in some systems.

4.5 Performance characterizations

4.5.1 Wavelength stabilization

To assess the improvement of the closed-loop stabilization, a direct measurement of the feedback signal from the PSD was used. This corresponded to directly assessing the quality of the stabilization of the OPO output wavelength. We tuned the desired wavelength to its maximum output power (the set point) and recorded the error signal in the time domain over a period of 200 s with a sampling resolution of 256 kilosamples. The measurement was performed twice, once with the feedback loop open (OPO free running) and once closed (wavelength maintained) as plotted in Figure 4.8.

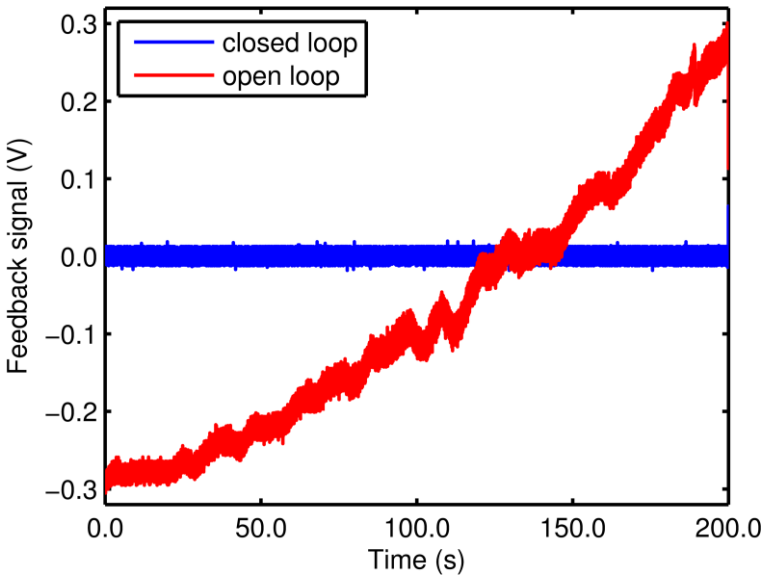

Figure 4.8. Signals directly obtained from the PSD presenting the fluctuating unlocked case (red signal) and the constant signal corresponding to a closed feedback loop (blue signal).

The power spectral density (PSpD) refers to the averaged power level of the noise frequency in the measured interval. In Figure 4.9, measurements for the stabilised loop (red) and the open loop (blue) are presented. The left abscissa is the power density in dB relative to the set point (wavelength) over the measured bandwidth in Hz. The power spectrum was normalized to the power of the time domain signal in respect of the Nyquist–Shannon sampling theorem. The value of the integrated power error (right ordinate) was used as a relative measure of the power stabilization between the closed loop (red line) and open loop (black line). The residual noise floor at -80 dB is the result of the quantization error from the oscilloscope. By comparing the two cumulative

signal errors, a 40-fold improvement in the wavelength stability between the stabilized and free running OPO was achieved over an observation time of 200 s. The measurable improvement is limited to a frequency at around 100 Hz where the residual noise levels make the two signals indistinguishable.

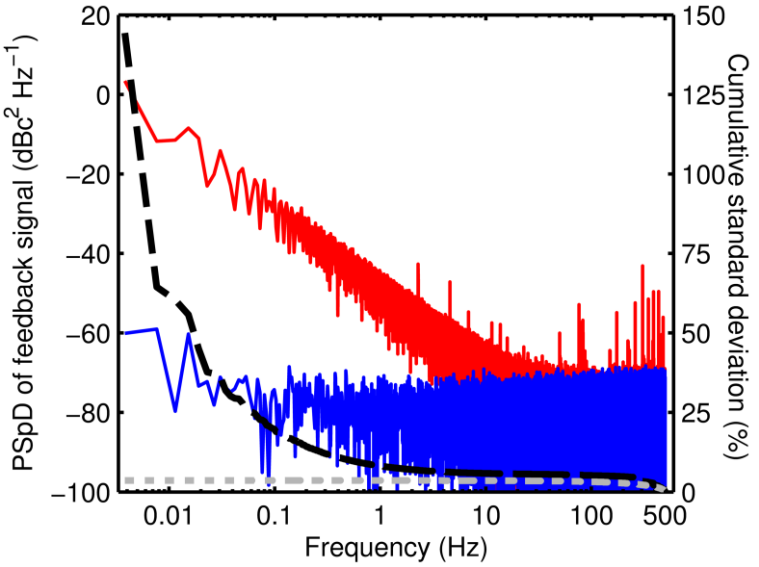

Figure 4.9. Power spectral density of the feedback signal from the position-sensitive detector shown in Figure 4.8. The blue curve was acquired while the feedback loop was closed and the controller set point (target wavelength) was maintained. The red curve was obtained without feedback. The dotted grey and dashed black lines (right ordinate) indicate the cumulative fluctuations for closed-loop and open-loop performance respectively.

4.5.2 Power stabilization

While the wavelength of the OPO is directly controlled by the feedback loop, the output power is only a correlated quantity which is not directly controlled, but whose fluctuations are expected to be reduced by implementing wavelength stabilization. Power stabilization can therefore be considered as a test of the residual passive stability of the system when the wavelength is controlled. During wavelength stabilization, the feedback serves to maintain oscillation at some chosen wavelength, and the remaining power fluctuations originate from uncontrolled parameters such as instabilities in the pump laser power. We recorded the power fluctuations of the pump laser and the OPO output simultaneously with silicon and InGaAs photodiodes, respectively. The relative intensity fluctuations were measured twice, once with the feedback loop open (OPO free running) Figure 4.10(a) and once closed (wavelength maintained) Figure 4.10(b).

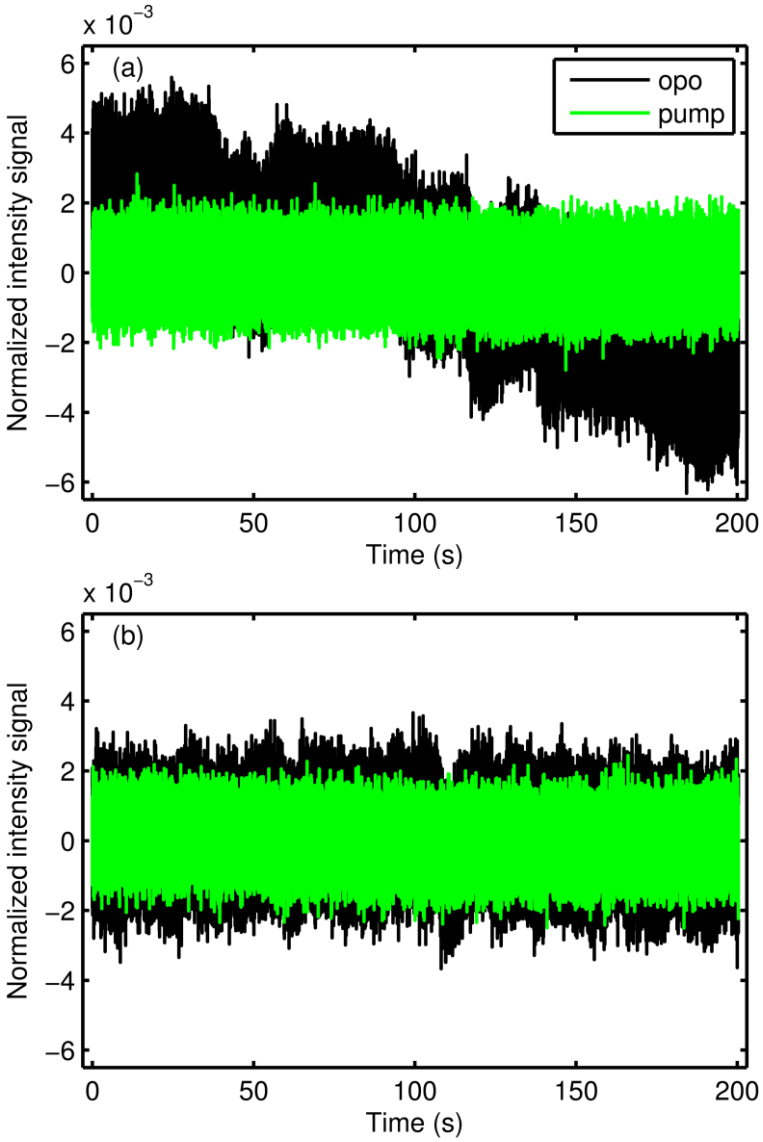

Figure 4.10. (a) Relative intensity signal of the pump laser (green) and of the OPO (black) with the system free running (no wavelength stabilization enabled). (b) Relative intensity noise with cavity stabilization enabled.

The relative intensity noise (RIN) of both optical signals was calculated by normalizing the mean time-domain level to unity and considering the fluctuations about this normalized level. The RIN for open-loop operation (wavelength stabilization off) is plotted in Figure 4.11(a), where the green line corresponds to the pump noise and the black line to the open-loop OPO signal. The cumulative power error for each plot (right ordinate) indicates the instability of the power recorded over 200 s. During the measurement, ambient disturbances were avoided and the entire OPO cavity was protected inside a box. The plot indicates only minor temperature fluctuations and low-frequency acoustical disturbance. It can be seen from the data that the OPO drifted over

its entire power range during the observation time and had tuned out of its working range within a few minutes. This behaviour is attributed to small changes in the room temperature causing and effective change in the OPO cavity length.

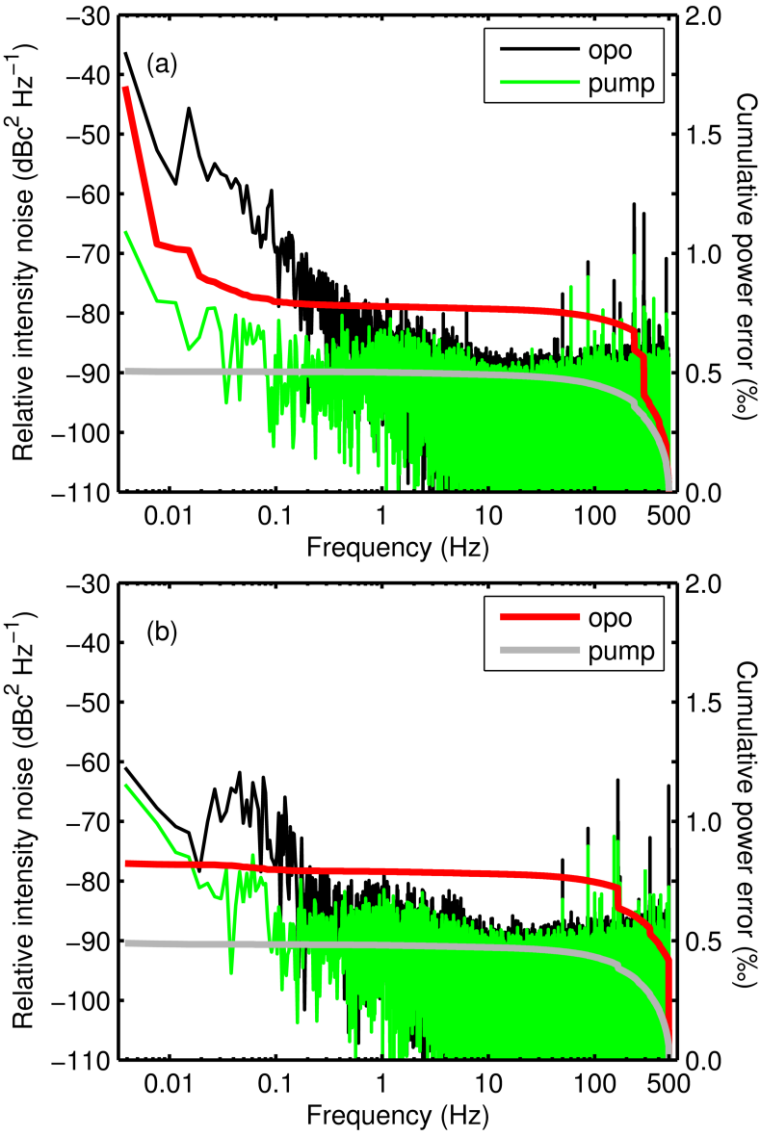

Figure 4.11. (a) The relative intensity noise of the pump laser (green) and of the OPO (black) with the system free running (no wavelength stabilization enabled). (b) Relative intensity noise with cavity stabilization enabled. The cumulative power error of the pump (grey) and OPO (red) are plotted in (a) and (b) on the right ordinate respectively.

Figure 4.11(b) presents the pump laser and OPO RIN with an identical arrangement as before, except now with the wavelength stabilization active. A comparison of the two

plots indicates that the OPO RIN is now limited only by the noise introduced by the pump source. Such limitations arise from disturbances that affect the power, but leave the signal wavelength unchanged, so are not suppressed with the wavelength stabilization approach. Nevertheless, with wavelength stabilization active, the accumulated power fluctuations are nearly identical for the OPO and its pump laser across a 5 mHz - 100 Hz bandwidth, indicating that wavelength stabilization can raise the stability level of the OPO to close to that of its pump laser.

4.5.3 Long-term stability

Daily temperature cycling of the system, resulting in the expansion of the pump and OPO cavities, can lead to an effective cavity length change of a few hundred µm, significantly exceeding the 6-µm range of the PZT used for wavelength stabilization, and normally requiring manual intervention. In particular, in our system, the first hour of operation, which included the warm-up phase of the pump laser, required a large change in the cavity length to be applied in order to maintain a constant wavelength. To keep the PZT operating in the centre of its displacement range, a controllable stepper motor was used to actuate the cavity end mirror (M8), accordingly. A software loop used to control the long-term stability is presented in Figure 4.12. A start-up sequence was included in the loop, which automatically started the OPO. This also enabled software-based tuning over the whole wavelength range simply by changing the controller set point.

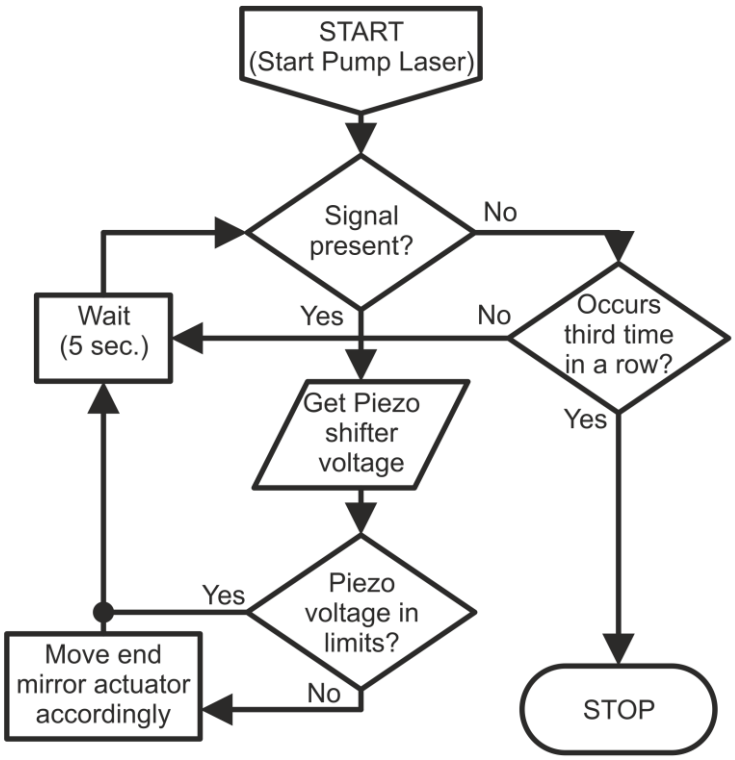

Figure 4.12. Flow chart of the software loop used to provide long-term stability by maintaining the PZT in its centre position.

As a test of this approach to long-term stabilization, the displacement of the end mirror was recorded over a period of 8.3 hours, and is presented in Figure 4.13. The entire displacement of the stepper-controlled mirror covered around 130 μm, a factor of more than 20 times the displacement range of the PZT. The source of this shift was attributed to changes in the pump laser during its warm-up period, because repeating the measurement once the pump laser was warmed up (~2h) reduced the necessary end-mirror displacement significantly. The most possible explanation is that a temperature change of the gain medium in the Yb:fibre master-oscillator caused a length change and therefore, the pulse repetition rate of the pump laser was shifted.

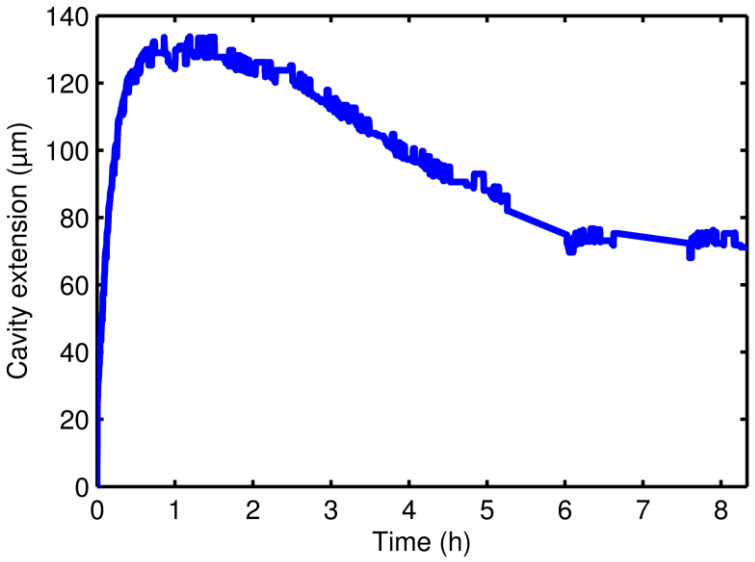

Figure 4.13. Measurement of the relative end mirror position resulting in a cavity extension recorded over a period of 8.3 hours.

4.6 Dither-locking as an alternative method of power stabilisation

Dither-and-lock offers an alternative route to maintain the laser output power at a desired level. With this method, the power is a directly monitored and controlled parameter. There have been early reports of power locking in a pulsed CO_2 [53], and very recently in doubly-resonant OPOs [54–56]. The majority of dither locking work has focused on providing wavelength stability by utilising certain laser transitions, used in frequency stabilised sources [57].

Commonly, any laser or nonlinear source exhibits a Gaussian-like or parabolic shaped intensity versus cavity length output profile. On a first glance, such a response provides an ambiguous error signal where the peak, and hence the point of maximum power, is inaccessible due to power fluctuations. A real world example of such a profile is shown in Figure 4.14, and was recorded from the OPO cavity introduced in Chapter 3.

In general, the dither-and-lock implementation is based on a modulation of an accessible system boundary by a constant signal of known amplitude, frequency, and phase. In turn, this modulation is directly transferred into the output signal sought to be stabilised, and therefore should only be introduced with the smallest necessary amplitudes. In OPOs, such a modulation can be achieved by cavity-length modulation.

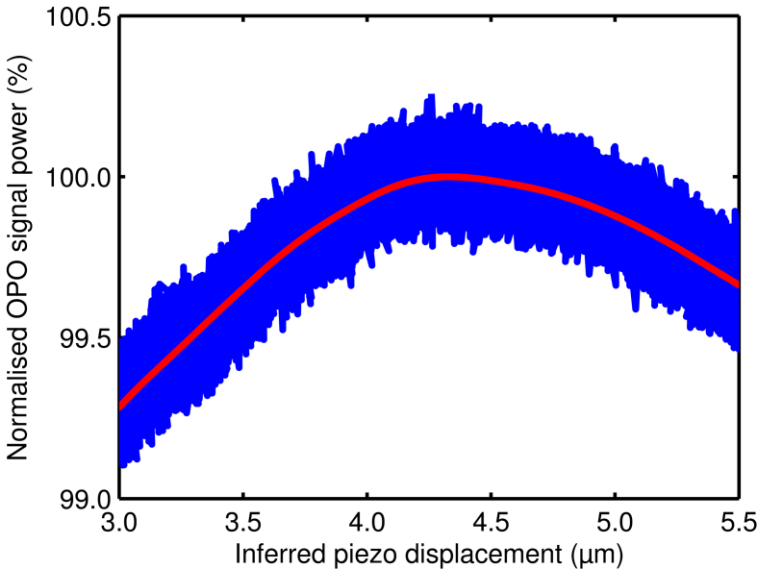

Figure 4.14. Measurement of the OPO output power relative to cavity-length detuning. The blue signal is the raw data, the red line is the averaged data and used for normalisation.

An example of the technique is presented in Figure 4.15, in which a four-mirror ring cavity is laid out showing the mirror attached to the piezo transducer (PZT) and a frequency generator (FG) providing the modulation signal. The altered intracavity signal is sampled with a photo detector (PD) aligned behind a partially transparent cavity mirror.

In order to be able to investigate the dither-locking technique through a formal approach we followed the layout shown in Figure 4.15. In addition, the cavity output power over cavity length distribution $P(z)$ was assumed to be of the Gaussian form,

$$P(z) = e^{-\frac{(z-z_{off})^2}{2v^2}}, \qquad 4.11$$

where z is the cavity length, z_{off} the offset of the power peak away from zero position (centre of nominal modulation stroke of transducer), and v the variance. This simplified distribution is depicted as the solid black line in Figure 4.16 (a-c) covering a range of $-1\ \mu m \leq z \leq +1\ \mu m$ and with $v = 0.22$. The Figure presents three cases where z_{off} was set to (a) 0 µm, (b) -0.125 µm, and (c) 0.0125 µm. The modulation signal supplied by the frequency generator was represented as,

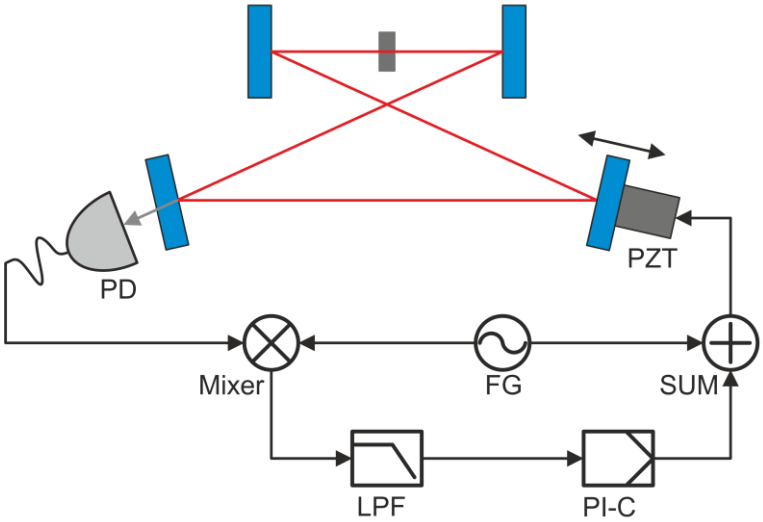

Figure 4.15. Schematic of a possible setup used for direct power stabilisation of an OPO cavity. The summer (SUM) adds the signal from the frequency generator (FG) with the mixed, low-pass filtered (LPF), and amplified (PI-C) signal. The sum is applied to the piezo transducer (PZT) in order to adjust the cavity length according to the feedback signal from the photodiode (PD).

$$S(t) = A\,sin(\omega t)\,, \qquad 4.12$$

where ω is the angular frequency $\omega = 2\pi f$ in rad, A the amplitude in volts, and t the time in seconds. For simplicity, the modulation amplitude in volts was assumed to be converted proportionally into a cavity length variation in µm described by $B = 1$ µm/V.

The cavity modulation signal is plotted (blue dotted line) along the ordinate in Figure 4.16 (a-c) using a normalised frequency scale and an amplitude B of 0.125 µm. In order to derive the modulated signal sampled by the photo detector, z in equation 4.11 was replaced by $S(t)$ (equation 4.12) leading to

$$Y\big(z(t)\big) = e^{-\frac{\left(B\,sin(\omega t) - z_{off}\right)^2}{2v^2}}\,. \qquad 4.13$$

$Y(z(t))$ corresponds to the red dashed lines in Figure 4.16 (a-c) with its base time again normalised.

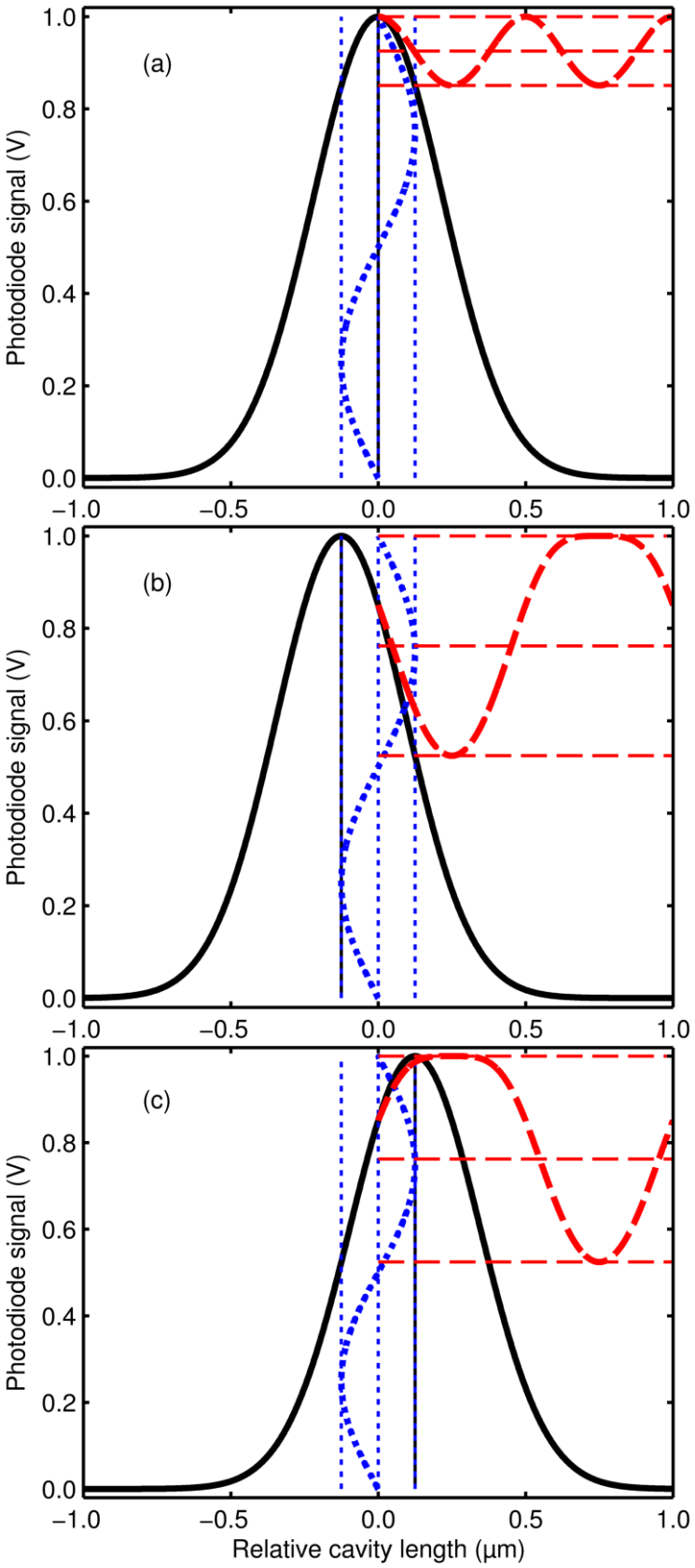

Figure 4.16. Black: Indicates the output power variations as a function of cavity length; Blue: The cavity length modulation (physical dither); Red: The modulated power when: (a) the mean of intensity and modulation are coincident; (b) intensity mean shifted right; (c) intensity mean shifted left.

Once the signal has been picked up by the detector, it is fed into the mixer and multiplied with the initial modulation signal $S(t)$. The mixer output $M(z,t)$ is therefore

$$M(z,t) = Y\big(z(t)\big)S(t)$$
$$= A\sin(\omega t)\; e^{-\frac{\left(B\sin(\omega t)-z_{off}\right)^2}{2v^2}}. \qquad 4.14$$

The output of the mixer is visualised in Figure 4.17, showing the outcome for the three different scenarios presented in Figure 4.16 (a-c).

In practice, the modulation frequency is in the range of several kHz (5 to 20 kHz) and the amplitude kept to a few nm of physical displacement. In addition, a low pass filter (LPF) with a cut-off frequency much smaller than the modulation frequency (3 to 30 Hz) is placed after the mixer to prevent the feedback loop from getting into resonance, as well as to supress noise otherwise fed back into the system originating from the electrical devices.

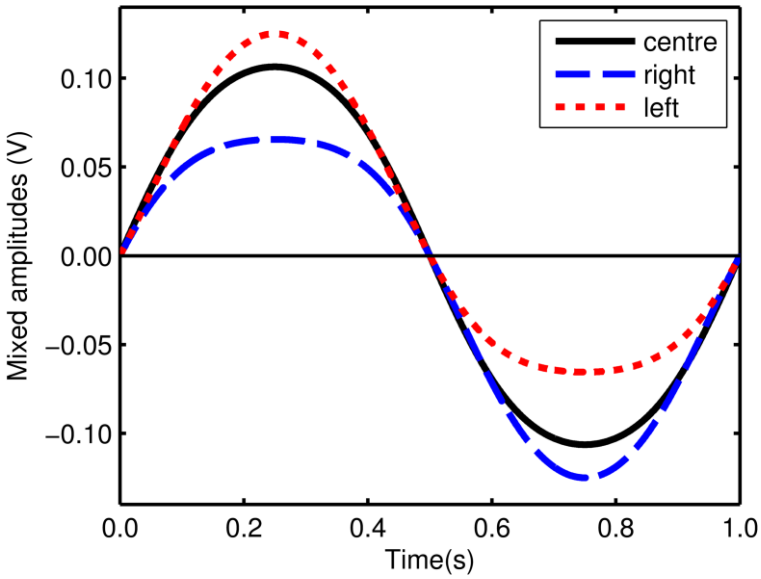

Figure 4.17. Result of the mixing process between the modulation signal (Sine) and the intensity-modulated signal detected with a photodiode corresponding to Figure 4.16 (a) centre, (b) right, and (c) left. These results are true for zero phase delay.

Once the high-frequency content of the mixer has been removed using the LPF it can be used as an input signal to a PI-Controller. For the presented results, the P gain value of the controller was held at 1 leading to the following expression:

$$E(t) = \int_0^{\tau} A\,sin(\omega t)\; e^{-\frac{\left(B\,sin(\omega t) - z_{off}\right)^2}{2v^2}}\,dt\,. \qquad 4.15$$

Integrating for different z_{off} ranging from -0.125 to 0.125 µm, led to a range of error signals depicted with the red continuous line in Figure 4.18. Contrary to intuition, the error signal is a monotonic function, crossing zero at the point of maximum power and almost linear over the simulated range. By treating the whole chain with normalised amplitudes, the intrinsic gain factor was revealed to be about 0.12 with an output of 0.015 V for a mismatch of 0.125 µm. This is true for the applied Gaussian variants of 0.22 and growing with declining variance.

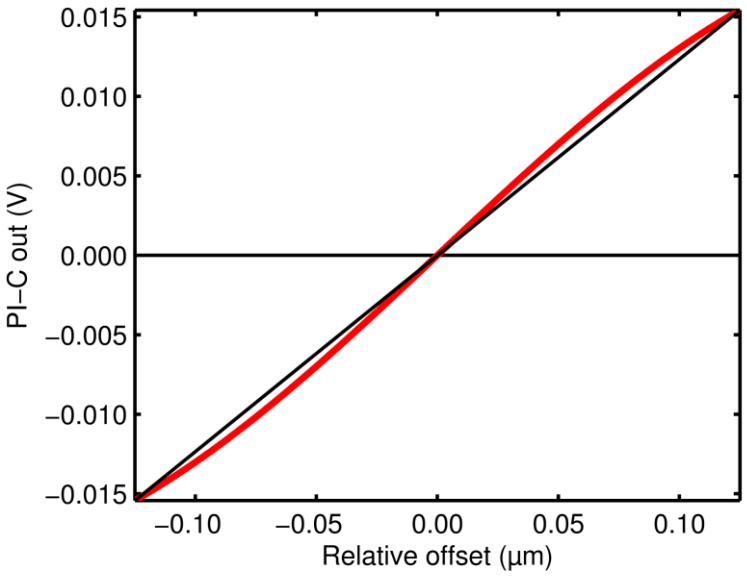

Figure 4.18. Graph of the integrated signal from the PI-controller covering a relative displacement of the intensity mean as indicated in Figure 4.16 (b - c). These results are true for zero phase delay. The black slope was determined through the minimal and maximal points in the curve.

Until now, the signals were assumed to be perfectly in phase until they both reach the mixer, however the signal used to modulate the cavity will see a significant phase shift. The degree of phase shift depends on the frequency and amplitude applied to the PZT.

In order to reflect this in equation 4.15, a phase shift term θ in the cavity modulation part is introduced as,

$$E(t) = \int_0^{\tau} A\,sin(\omega t)\; e^{-\frac{\left(B\,sin(\omega t-\theta)-z_{off}\right)^2}{2v^2}}\,dt\,. \qquad 4.16$$

Calculating the slope of the error signal as indicated by the black line in Figure 4.18 for a range of phase shifts from zero to 2π was plotted in Figure 4.19. The result shows the significance of phase between the two mixed signals clearly. In order to tune the phase shift to π, the amplitude and frequency of the signal from the FG can be altered where the phase is physically introduced through the PZT.

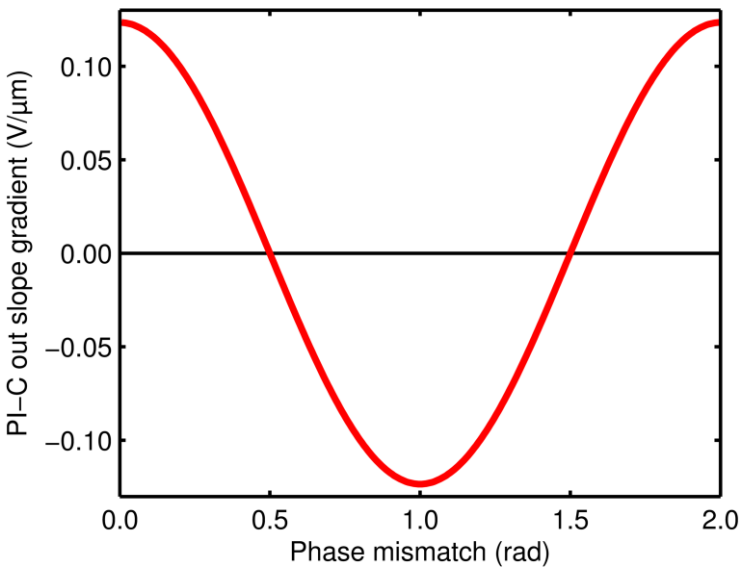

Figure 4.19. Plot of a variable phase shift introduced between the two mixed signals from 0 to 2π.

Setting up a second mixer where one of the signals is constantly phase shifted by a factor of $\theta = \pi/2$ could be used to adjust this loop to zero, while ensuring that the initial feedback signal is adjusted to its maximum amplitude.

Comparing dither locking with wavelength stabilisation, a continuous, monotonic curve either side of the maxima peak is required for the dither locking because local maxima

cannot be overcome if the dither stroke does not reach beyond the peak and the dip in order to access regions of higher power. Furthermore, any temporal or spectral fluctuation in the pump intensity, pump repetition rate (pump jitter), or temperature fluctuations of the OPO crystal are compensated to maintain maximal possible output power, however the drift of the OPO output wavelength could remain uncontrolled. As mentioned in the introduction, the signal intended to be stabilised is also modulated and, therefore this modulation, is transferred into the output of the stabilized source.

Reflecting the special case where an OPO is cavity-dumped, such as the one introduced in Chapter 5, a dither-locking approach could mislead the controller loop to lock-in away from the maximum peak. The reason for this lies in the fact that cavity dumping based on an acousto-optic modulator is wavelength selective, since the Bragg condition is only fulfilled for the centre wavelength, preferably at maximum power, and less efficiently at longer and shorter wavelengths. Therefore, a Gaussian power characteristic and a similar spectral shape would compete with each other, eventually leading to two side peaks of higher intracavity power (but less output power) where the loop would lock into one or the other. A work-around could be found by sampling the cavity-dumped power, however the feedback would only be valid while cavity dumping was active.

4.7 Conclusions

A formal approach to finding the optimal feedback parameters for OPO wavelength stabilisation was presented. By introducing a valid model of all the components present in the feedback loop, experimentally obtained responses were understood and explained. The presented results showed a 40-fold improvement in wavelength stabilisation as well as a 2-fold improvement of power fluctuations, mainly limited by the existing pump noise. The final section addressed the possibility of dither locking as an alternative stabilisation technique and indicated that it could be suitable for oscillators where the output varied smoothly across a maximum value as the cavity length was tuned.

Chapter 5 - Cavity-dumped ultrafast optical parametric oscillator pumped by a Yb:fibre laser

5.1 Introduction

In Chapter 3, an increase of the extracted pulse-energy by increasing the pump power combined with cavity length extension was reported. This chapter introduces a further stage of pulse energy scaling, namely cavity dumping, allowing the extraction of pulse energies exceeding those of the pump, at the expense of lower repetition rate and lower extracted average power. The development was driven by the demand for high-energy ultrafast lasers with repetition rates in the hundreds of kHz range. Such systems provide superior results in laser waveguide inscription because they can operate in a thermally moderated regime, which is inaccessible to lower-repetition-rate systems [24]. Waveguide inscription in this high-repetition-rate regime is limited by the availability of suitable sources, which are generally restricted to systems operating around 1060 nm, in the form of cavity-dumped solid-state lasers [58] or pulse-picked Yb:fibre master-oscillator power-amplifier systems [59]. The inscription of infrared materials such as Si [60], Ge and certain chalcogenide glasses implies a need for ~ 1-µJ sources operating at wavelengths well above 1060 nm. In this context, this work describes a new class of synchronously pumped optical parametric oscillator (OPO), capable of providing sub-250-fs pulses at repetition frequencies from 101 kHz – 15.3 MHz, and with energies sufficient for waveguide inscription via refractive-index modification [24].

To date, the highest pulse energies from a femtosecond OPO were obtained from a fibre-feedback OPO, based on periodically-poled stoichiometric $LiTaO_3$, producing 339-nJ, 840-fs signal pulses at a wavelength of 1450 nm [8]. Recently, another fibre-feedback OPO based on MgO:PPLN and operating from 1.5 – 1.7 µm produced 490-nJ, 100-ps pulses [9]. Both of these systems realized energy scaling by operating at high average power, however cavity-dumping a synchronously-pumped OPO [10,11] offers an alternative route to high-energy pulses by using a pump laser with significantly lower average output power. In this chapter, a cavity-dumped system exceeding the performance of all previous femtosecond OPOs in both pulse energy and peak power is described.

5.1.1 Cavity-dumping as a resource to higher pulse energies

The term cavity dumping describes a technique employed to extract individual pulses, at rates lower than the fundamental cavity repetition rate f_{rep}, which is in contrast to the classically used continuous output coupling of the resonant pulses in the cavity. This allows us to extract pulse energies up to an order of magnitude higher compared to direct output coupling, since the cavity can be operated in a low-loss regime (all mirrors are high reflectors) and therefore is able to build up much higher intra-cavity powers. The implementation is typically based on an electrically controlled optical switch, employing either a Pockels cell or an acousto-optic modulator, accommodated as an additional intra-cavity optical element, which is used to modify the optical properties of the resonant light in such a way that it is possible to separate it from the otherwise indistinguishable resonant beam. The technique is very flexible, providing both an adjustable extraction of pulse energies from zero up to 95% and variable repetition rates ranging from pulses on demand up to several MHz, dependent on the cavity layout, gain material as well as on the underlying modulator and the drive electronics performance.

A very similar technique to cavity dumping is known as pulse picking, where the modulator is situated extra-cavity (after the output coupler) in order to reduce the fundamental repetition rate of an oscillator. This could be useful, for instance, to reduce the repetition rate (the individual pulse energies are preserved but the average power is reduced) into a subsequent amplifier stage allowing pulses with much higher energy compared to the situation where all pulses would be amplified, assuming that the amplifier maintains its average output power. A benefit of a pulse-picker is its simple implementation because it involves no modification to an existing cavity design. In addition, the stability of the oscillator is not disturbed due to an internal modulation but, at the cost of significantly lower pulse energies in comparison to those accessible through cavity dumping. Therefore, achieving higher pulse energies with pulse picking requires a further amplification stage, which adds to the complexity and costs of a system, and for some wavelengths, such amplifiers are unavailable.

Cavity dumping therefore provides an attractive alternative, however, the implementation of the additional elements as well as the material-dependent dispersion compensation of the additional dumping element has to be carefully considered.

5.1.2 Principles of electro-optic modulators

Today there are two different types of devices, electro-optic modulators (EOM) and acousto-optic modulators (AOM), both of which are commonly used for cavity dumping, but which have noteworthy differences.

An electro-optic modulator can be used to change the polarization state of the light beam while it propagates through the medium. One could describe it as an electrically adjustable wave plate. Such a device exploits the linear electro-optic effect where the refractive index of a material is altered linearly in proportion to the applied electric field strength, preferably along one crystallographic axes, introducing birefringence. This is also known as the Pockels effect (first described by the German physicist Friedrich Pockels) and therefore electro-optic modulators are sometimes called Pockels cells. Only materials that are not inversion- or centro-symmetric show the effect such as potassium titanium oxide phosphate (KTP), potassium (di-) deuterium phosphate (KD(*)P), β-barium borate (BBO), as well as lithium niobate ($LiNbO_3$) or semiconductor based materials like gallium arsenide (GaAs), to name a few common ones.

A typical cavity setup comprising an EOM as cavity-dumper is shown in Figure 5.1(a) where the dumping section consists, besides the cell, of a thin film polarizer (TFP). The TFP is aligned to transmit the horizontally polarized laser light while it is highly reflective for vertically polarized light. Once the intra-cavity pulse has passed the EOM, it is switched on, rotating the purely horizontal polarized light by some degree into elliptical polarized light where all vertical components are reflected out of the cavity by the TFP. After the dumping takes place, the EOM is returned to its relaxed state and the pulse is allowed to undergo several roundtrips to build up again. A rotation by 90°, causing an extraction of the entire light is usually not possible due to parasitic limitations of Pockels-cells. For cavity-dumped mode-locked lasers in particular a depletion of 100% of the intra-cavity power is not desirable since the remaining light is used as a seed, enhancing the build-up of the next pulse, which results in a much higher overall efficiency.

The benefits associated with electro-optical modulators are a broad switching dynamic range, ranging from a few Hz up to frequencies in the GHz-regime, instantaneous

switching, as well as the ability to utilize large active apertures reducing the potential of optical nonlinearities. Drawbacks are the complexity of the required high voltage drivers especially at high switching frequencies where resonances can cause ringing. Moreover, the longer the wavelength, the weaker the Pockels effect leading to a call for higher voltages or longer crystals to achieve the same degree of rotation. Longer crystals in turn introduce a stronger spatial walk-off, more dispersion, as well as nonlinearities into a cavity setup.

Some of the above problems are relaxed by the use of an AOM, but at the cost of switching speed, which can be significantly slower than those available from an EOM. In addition, a tight focus is required for fast switching times, which limits the intracavity power to the damage threshold of the AOM-crystal.

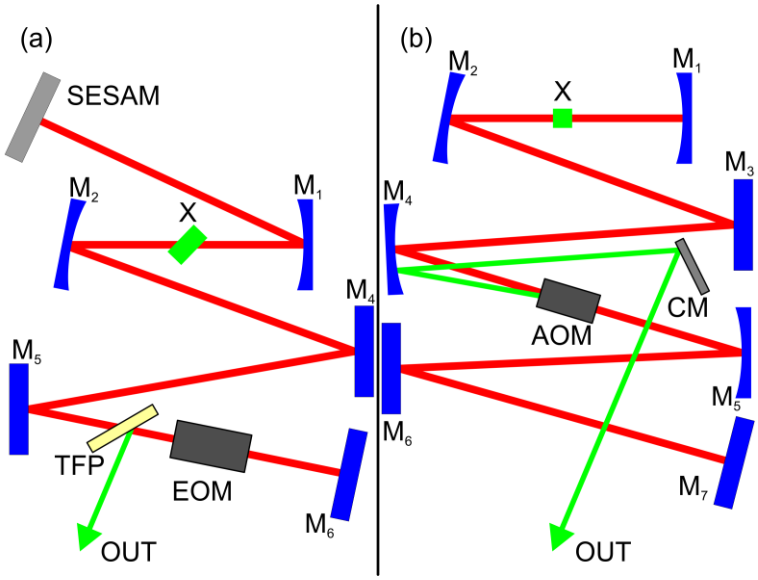

Figure 5.1. a) Typical cavity-dumping mode-locked laser with an EOM where the dumped beam is extracted with a thin film polarizer (TFP); b) cavity-dumping setup based on an AOM. M_4 is used for collimation of the diffracted beam and is then reflected off a collection mirror (CM).

A representative cavity schematic using an AOM as a cavity-dumper is shown in Figure 5.1(b). The cavity was altered to integrate the AOM cell comprised by an additional focusing section. After collimation with one of the focusing mirrors (here M_4), the beam can be readily collected with an additional external mirror (CM). It is important to consider that the beam displacement should be greater than the beam radius to avoid undesired clipping of any of the two parallel beams due to an overlap.

5.1.3 Principles of acousto-optic modulators

5.1.3.1 The photoelastic effect

Acousto-optic (AO) devices exploit the photoelastic or elasto-optic effect. This effect is stimulated by an acoustic wave which, propagating across a medium, forms regions where matter experiences either compression, reaching its maximum at the intensity peak of the acoustic wave or rarefaction, approaching its minimum at the intensity dip respectively. A piezo-electric transducer, physically bonded to the AO medium, allows a controlled injection of an acoustic wave where the introduced strain changes the material density, coinciding with a modification of the refractive index, introducing a phase grating with its periodicity identical to the wavelength of the acoustic wave. Similar to optical gratings is a proportion of the light diffracted. Furthermore, due to the propagation of the phase grating with the speed of sound inside the medium, the diffracted light experiences a Doppler-shift. A formal description of a crystallographic tensor relation, describing the dependency between elastic strain and the photoelastic coefficients, was provided in Goutzoulis [61] as,

$$\Delta\left(\frac{1}{n^2}\right)_{ij} = p_{ijkl}S_{kl}\,. \qquad 5.1$$

S_{kl} represents the strain component where p_{ijkl} is the dimensionless fourth-rank photoelastic tensor connecting the strain with the relative change of the optical index ellipsoid $\left(\frac{1}{\varepsilon}\right)_{ij} = \left(\frac{1}{n^2}\right)_{ij}$ (here neglecting the complex part$-\kappa^2$). A detailed derivation of Δn_{ij} can be found in in Boyd [14] as well as in Yariv [15] and is given as,

$$\Delta n_{ij} = -\frac{1}{2}n_{ij}^3 p_{ijkl}S_{kl}\,. \qquad 5.2$$

Knowing the relation between the strain and the associated change in refractive index and assuming the acoustic stimulus as a sinusoidal traveling wave allows us to quantify the refractive index pattern in time and space as $n(x,t)$ relative to the equilibrium state n_{eq} of an individual material as,

$$n(x,t) = n_{eq} + \Delta n \sin(\Omega_a t - K_a x)\,, \qquad 5.3$$

where Ω_a is the acoustic angular frequency defined as $\Omega_a = 2\pi f_a = 2\pi \frac{v_a}{\Lambda_a}$, and K_a is the acoustic wavenumber $\left(\frac{2\pi}{\Lambda_a}\right)$, with f_a, v_a, and Λ_a being the AO-driver radio frequency, the speed of sound in the AO-material, and the acoustic wavelength, respectively. Δn represents the amplitude of the index modulation of the planar wave as expressed in equation 5.2.

Based on a Cartesian coordinate system, where an optical wave propagates in the x-z-plane (see Figure 5.2(a)) inside a medium that is simultaneously penetrated by an acoustic wave in x-direction, Raman and Nath [62,63] proposed the following wave equation

$$\nabla^2 E = \left[\frac{n(x,t)}{c_0}\right]^2 \frac{\partial^2 E}{\partial t^2}\,, \qquad 5.4$$

with E as the electric field and c_0 being the speed of light in vacuum. Merging equation 5.3 into 5.4, the partial differential equation can be solved by means of a Fourier series [61] describing the amplitude E_m and wave vector k_m of the m^{th}-diffracted order in relation to the incident light beam with frequency ω_i and wave vector k_i as

$$E(x,z) = \sum_{m=-\infty}^{\infty} E_m(z) e^{i[(\omega_i + m\Omega_a)t - k_i(z\cos\theta_i - x\sin\theta_i) + mK_a x]} \qquad 5.5$$

with θ_i as the angle the incident light is propagating through the previously defined x-z-plane (see Figure 5.2(a)). Combining equations 5.3 and 5.5 into equation 5.4 allows one to derive a set of coupled wave equations [61] presenting an individual solution for each diffraction order. These equations were solved by Raman and Nath [62,63] to give,

$$\frac{dE_m}{dz} + \frac{u_1}{2L}(E_{m+1} - E_{m-1}) = i\frac{mK_a}{cos\,\theta_i}\left[\frac{mK_a}{2k_i} - sin\,\theta_i\right]E_m \qquad 5.6$$

with u_1 defined to

$$u_1 = -\frac{k_i \Delta n L}{cos\,\theta_i}, \qquad 5.7$$

where L is the path length at which acousto-optic interaction takes place and k_i is the incident wavenumber (see Figure 5.2(a-c) for more details). Investigating equation 5.6 for geometries where considerable energy is coupled out of the zero order led Klein and Cook to establish a Q-parameter [64] as

$$Q = \frac{K_a^2 L}{k_i\,cos\,\theta_i} = \frac{2\pi\lambda_0 L}{n\Lambda_a^2\,cos\,\theta_i}. \qquad 5.8$$

If $Q \leq 0.3$ [61], the AOM is meant to operate in the Raman-Nath regime, where diffraction occurs simultaneously at multiple orders analogous to the diffraction pattern known from thin gratings. Physically, this can be explained by the way the acoustic wave is traveling through the material. The part of the acoustic wave traveling close to the boundaries of the cell experiences a continuous phase shift due to a coupling into surface waves and the shorter the cell is, the more a plane acoustic wave becomes distorted into a spherical wave. Therefore, the incident light experiences a continuous change of the effective acoustic wavelength, hence diffracting into a multiple orders.

5.1.3.2 Bragg condition

When $Q \geq 7$ [61] the diffraction becomes sensitive to the angle the light is incident, which occurs when crystal length is extended where the phase grating becomes long. This regime is known as Bragg-diffraction or Bragg-scattering and the name is given in analogy for X-ray scattering from atomic planes in a crystal [14].

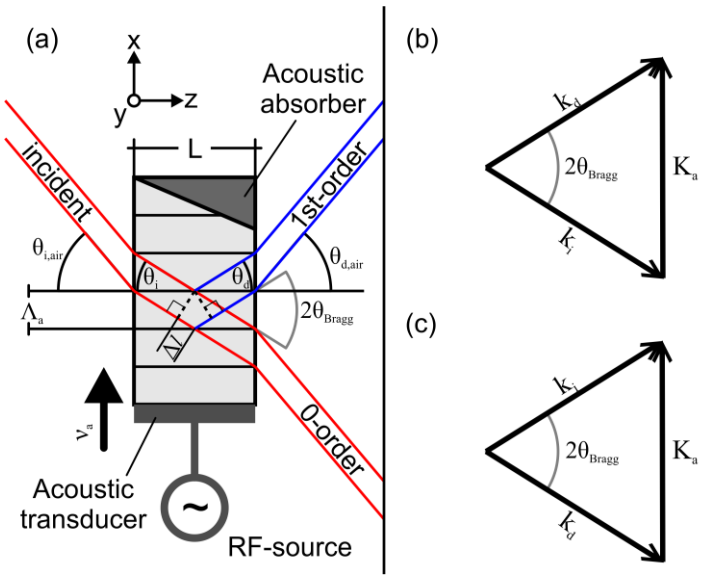

Figure 5.2.(a) Schematic showing acousto-optic scattering of an incident beam (red) partially diffracted into its first order (blue) by a sinusoidal diffraction pattern. The acoustic wavelength Λ is indicted through the black lines inside the crystal where the direction of the acoustic wave v_s is denoted with the black arrow. (b) Shows the wave vector diagram for the situation shown in a) and $\theta_i = \theta_{Bragg}$. (c) The wave vector diagram for the case where the beam is incident at $-\theta_i = -\theta_{Bragg}$.

Figure 5.2(a) shows a schematic of an acousto-optic modulator operating in the Bragg-regime with the red lines implying an incident beam whereas the blue lines represent the portion diffracted by the acoustic wave with wavelength Λ_a, indicated by the black lines across the crystal. In addition, a piezoelectric transducer with RF-source was schematised as the driver of the acoustic wave and an acoustic absorber to prevent reflections, which would compromise the efficiency of the AOM.

Applying the wave theory derived in equation 5.6, with the diffraction order set to $m = 1$ and the aim to maximise E_1, implies that the two terms on the right-hand side must cancel each other by

$$sin\,\theta_i = \frac{K_a}{2k_i} = \frac{\lambda_0}{2n\Lambda_a} = \frac{\lambda_0 f}{2v_a} = sin\,\theta_{Bragg}\,, \qquad 5.9$$

where f is the acoustic modulation frequency, v_a the acoustic velocity and θ_{Bragg} the Bragg angle. The same conclusion could be derived with a geometrical approach, setting the path difference between two scattered portions of an incident beam to the same distance as the optical wavelength inside the medium $2\Delta l = \frac{\lambda_0}{n}$. As indicated in

Figure 5.2(a), the path difference is given by $\Delta l = \Lambda_a \sin\theta_{Bragg}$. Combining these two equations and solving for $\sin\theta_{Bragg}$ leads again to result presented in equation 5.9.

In order to calculate the Bragg angle outside the AOM one can either use Snell's law or more simply change the refractive index of the crystal in equation 5.9 into the refractive index of air. This angle presents a more practical number when it comes to designing the collimation of the deflected beam. The angles with respect to the refractive index of air were presented in Figure 5.2(a) as $\theta_{i,Air}$ and $\theta_{d,Air}$ for the incident and diffracted beam respectively.

Explaining the effect from a quantized view, diffraction of light in an acousto-optic material can be understood as photon-phonon scattering where an exchange of energy from the incident photon to a phonon and back into the diffracted photon, takes place. In fact, the diffraction process may be seen as a nonlinear process where three waves, namely the incident optical wave ω_i, the electrically stimulated acoustic wave Ω_a, and the diffracted optical wave ω_d, interact based either on difference frequency generation (DFG) or sum frequency generation (SFG) depending on the phase matching condition. The parametric processes are based on conservation of energy with the SFG defined as

$$\hbar\omega_i = \hbar\omega_d + \hbar\Omega_a\,, \qquad 5.10$$

and the DFG defined as

$$\hbar\omega_i = \hbar\omega_d - \hbar\Omega_a\,. \qquad 5.11$$

The phase matching and hence the sign of the frequency generation depends on the direction of the acoustic wave relative to the incident beam and obeys the law of angular momentum conservation by

$$k_d = k_i \pm K_a\,. \qquad 5.12$$

The wave vector diagrams for SFG and DFG are depicted in Figure 5.2(b) and Figure 5.2(c) correspondingly.

5.1.3.3 Acousto-optic diffraction efficiency

To calculate the diffraction efficiency of an AOM, we rearrange equation 5.6 with the emphasis to maximise the coupling from the incident beam E_i into the first diffraction order E_d by setting $\theta_i = \theta_{Bragg}$ which yields:

$$\frac{dE_i}{dz} + \frac{u_1}{2L} E_d = 0 \,. \qquad 5.13$$

The solution of the differential equation [61] can be used to derive the normalized intensity of the diffracted beam to be,

$$\eta_{DE} = 1 - I_i = sin^2 \left(\frac{\pi L}{\lambda_0 \, cos \, \theta_i} \sqrt{\frac{n^6 p^2}{2\rho \, v_a^3} I_a} \right), \qquad 5.14$$

with I_a as the acoustic intensity defined by the applied RF-power P_a divided by the acoustic beam cross section A_a (a product of acoustic interaction length L and acoustic beam height H) as,

$$I_a = \frac{P_a}{A_a} = \frac{P_a}{L \, H} \,. \qquad 5.15$$

Figure 5.3 presents the diffraction efficiency versus RF-power for the AOM used in this research. The blue curve represents the normalized diffraction efficiency and the red line links to the absolute efficiency taking into account the finite length of the crystal with a Q-factor of 22.5 limiting the efficiency to maximum 97%, (maximum efficiency value was provided by Jon Ward from Gooch & Housego [65]).

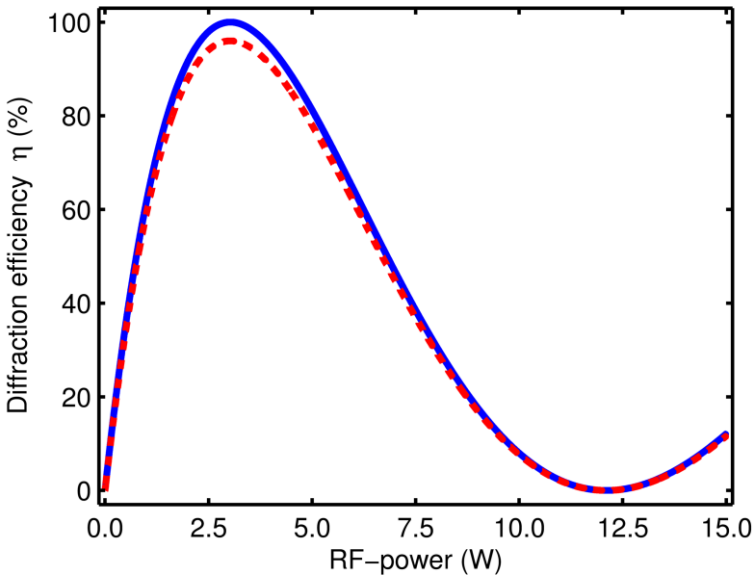

Figure 5.3. Shows normalized diffraction efficiency (solid blue line) and absolute efficiency (dashed red line).

By applying the trigonometric identity $1 = \sin^2(\pi/2)$, it is straightforward to derive the RF-power required at peak diffraction $P_{a,DE_{max}}$ from equation 5.14 as

$$P_{a,DE_{max}} = \frac{\lambda_0^2 v_q^3 \rho H \cos\theta_i^2}{2n^6 p^2 L} \,. \qquad 5.16$$

5.1.3.4 AOM rise time

A further important criterion to be considered in order to achieve a good extinction ratio between dumped and non-dumped pulses is the rise time of the modulator. There are two possible definitions, used to calculate the rise time. The simplest approach to calculate the rise time τ_r, is by calculating the time the acoustic wave inside the AOM to requires traverse the incident optical beam diameter d_0 $(1/e^2)$:

$$\tau_r = \frac{d_0}{v_a} \,. \qquad 5.17$$

There is an alternative definition whereby the rise time the acoustic wave requires to travel across the diffraction-limited Gaussian beam diameter is correlated to the 10% to 90% points of an error-function and is defined as,

$$\tau_{r,10-90\%} = \frac{4}{1.83\pi}\frac{d_0}{v_a}, \qquad 5.18$$

which gives shorter rise times in comparison to the previous definition. In Figure 5.4 rise times for a TeO_2-AOM with beam diameters ranging from 140 - 200 µm were plotted for a visual comparison of the two definitions. For an expected beam diameter of 150 µm inside a TeO_2-crystal, a rise time of 35 ns or 24 ns was returned respectively.

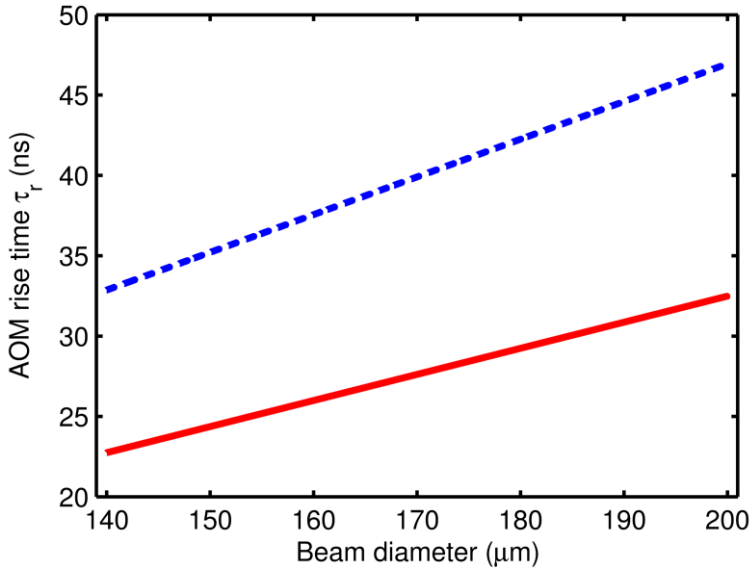

Figure 5.4. Rise times over beam diameter for the definition in Eq (5.17) (dashed blue line) and the definition in Eq (5.18) (solid red line).

The OPO presented in the previous chapter exhibits a fundamental repetition rate of 15.3 MHz, providing a timing window between consecutive pulses of 65 ns that needs to be divided by two for the standing wave cavity design in order to prevent the returning pulse from being dumped. With about 35 ns to establish diffraction over the full $1/e^2$-beam diameter this is just enough to operate the AOM with good efficiency. For a ring cavity, the timing constraints relax back by a factor of two since propagation occurs only in one direction.

Table 1 contains all material specific constants and their dimensions used to investigate the TeO_2-acousto-optic modulator with additional results for various calculations, and plots performed above.

Table 1: Material specific constants required to perform the calculations for the TeO_2-acousto-optic modulator. The material constants were either provided by Gooch & Housego [65] or taken from [66].

Material constants for TeO_2:	**Symbol:**	**Value:**	**Dimension:**
Optical wavelength	λ_0	1.55 x 10^6	m
Refractive index@λ_0	n	2.1898	
Photoelastic constant	p_{13}	0.34	
Density	ρ	6000	kg/m^3
speed of sound TeO_2	v_a	4260	m/s
Crystal length	L	7.60 x 10^{-3}	m
acoustic beam cross section	A_a	4.00 x 10^{-6}	m^2
acoustic modulation frequency	f	110 x 10^6	Hz
Calculated values:			
Quality factor	Q	22.5	
Bragg angle (inside crystal)	θ_{Bragg}	1.147	°
Bragg angle (in air)	$\theta_{d,Air}$	2.512	°
RF-power for max diffraction	$P_{a,DE_{max}}$	3.03	W
Rise time (full beam)@d_0=150 µm	τ_r	35.2	ns
Rise time (10-90%)@d_0=150 µm	$\tau_{r,10-90\%}$	24.4	ns

5.2 Designing a cavity-dumped optical parametric oscillator

5.2.1 Cavity design of the cavity-dumped OPO

The design was based on an extension of the OPO design introduced in Chapter 3, using the identical 10-W Yb:fibre laser to synchronously pump an MgO:PPLN crystal. The pump laser was a commercial system (Fianium FP1060-1uJ) producing chirped 15.3-MHz pulses. After an optimization of the grating compressor, a pulse train with 6.6 W average power and sub-400-fs durations was available for pumping the OPO. The OPO was resonant at 1.535 µm, using a 30-µm grating period of the temperature stabilized MgO:PPLN crystal with a length of 1.04 mm at 80°C.

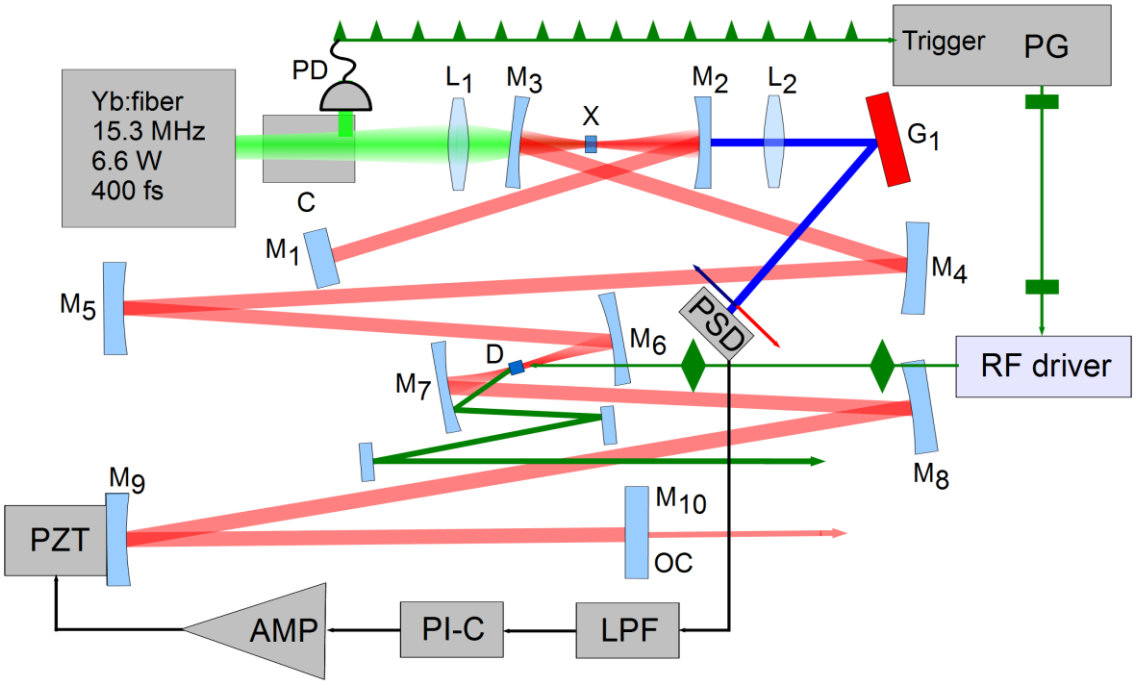

Figure 5.5. Cavity layout of the OPO comprising the AO-cell D, the focusing section with M_6 and M_7. PG, pulse generator in trigger mode; LPF, low-pass filter; C, compressor; PD, photodiode; X, MgO:PPLN crystal; OC output coupler. See text for other definitions.

Due to a significant pump laser instability experienced with the previous system, partially caused by back reflections of the layout, a modification from an asymmetric "V-cavity" design (see Figure 3.6 on page 50) to an asymmetric “X-cavity” layout (see Figure 5.5) was implemented. The additional fold in the short cavity arm decreased the back reflection considerably. In addition to this modification, a second AOM focusing section was required, enabling a focal spot radius of ~75 µm in order to achieve high dumping efficiencies with the additional constraint to maintain the previously approved 40 µm spot radius in the PPLN-crystal. The accommodation of the plane-plane TeO_2 acousto-optic modulator into the longer arm was achieved using the mirror pair M_6 and M_7. The resonant signal pulses were dumped as they propagated from mirror M_6 to M_7, and the dumped pulses were collimated by M_7 and finally collected by an extra-cavity mirror. The dumper was situated approximately in the middle of the cavity to maximize the available switching time before the residual intra-cavity pulse returned after a reflection from the plain output coupler (OC, M_{10}). Mirror-pairs $M_{4/5}$ and $M_{8/9}$ formed a 4f-relay system, which achieved a stable 9.8-m long cavity that was insensitive to misalignment.

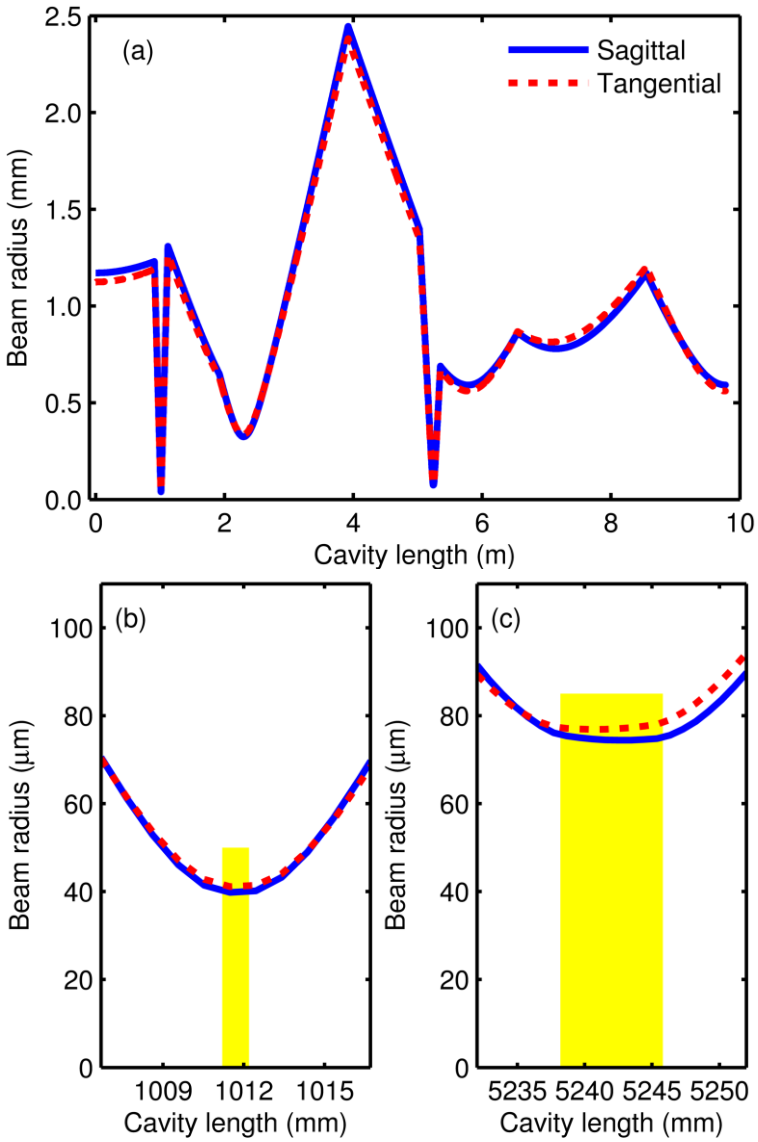

Figure 5.6. (a) Beam profile of the redesigned asymmetric cavity in order to accommodate the AOM. (b) and (c) show the first focusing section for the 1 mm long MgO:PPLN crystal and the second for the 7.6 mm long TeO_2 crystal respectively. The yellow patches were used to represent the crystal positions in proportion.

In Figure 5.6(a), the entire beam profile for the redesigned cavity is plotted. The $1/e^2$ diameter of the simulated cavity never exceeds 5 mm and the spherical aberrations, the mode-difference for sagittal and tangential beams, were kept to small values by maintaining folding angles close to normal incidence. The required radii as well as the confocal length were achieved in order to guarantee good performance of the OPO and dumper. This is illustrated in Figure 5.6 (b) and (c) showing a close-up into the focusing sections of the MgO:PPLN-crystal and the TeO_2-crystal crystals (indicated as yellow patches) respectively. All details necessary for the cavity model, including mirror radii, angles of incidence, the free space distances between the individual

components as well as the dimensions and refractive indices of the crystals, are provided in Table 2 along with the identifiers used in Figure 5.5.

Table 2: This table shows all optical elements and their separation used for the simulation of the cavity beam profile. The shaded rows indicate the elements used for the two 4f-relay sections.

Identifier	Optical element	Radius of curvature (mm)	Angle of incidence (°)	Free space after element (mm)
M_1	Plane mirror	∞	0	910.5
M_2	Spherical mirror	-200	1.8	101
X	OPO-crystal	MgO:PPLN of 1 mm length	and n=2.133 @1522 nm	107
M_3	Spherical mirror	-200	1.8	800
M_4	Spherical mirror	-2000	2.8	1998
M_5	Spherical mirror	-2000	2.85	1108.5
M_6	Spherical mirror	-500	1.85	212
D	AOM-crystal	TeO_2-crystal of 7.6 mm length	and n=2.190 @1522 nm	104
M_7	Spherical mirror	-200	1.5	1200
M_8	Spherical mirror	-2000	1.2	1998
M_9	Spherical mirror	-2000	0.9	1231.75
M_{10}	Plane mirror	∞	0	0 (end of cavity)

5.2.2 Dumping electronics

Cavity dumping was implemented by synchronising the entire dumping electronics to the pump laser repetition rate. The 15.3 MHz signal (f_{REP}) was detected with a fast photodiode which was connected to a frequency divider (Pulse Research Lab, PRL-

260ANT), used to divide f_{REP} down by a factor of four to 3.8 MHz. This signal was connected to the trigger input (limited to a maximum frequency of 5 MHz) of a pulse generator (Berkeley Nucleonics Corporation, BNC 575 Digital Delay / Pulse Generator) to produce electrical pulses at a sub-harmonic of f_{REP}. These pulses entered the digital modulation input of a radio-frequency (RF) driver (Gooch & Housego, A35110) which supplied a 110-MHz carrier to the AOM (Gooch & Housego, M110-2H/GJ), and their delay (65.2 ns) and duration (35.4 ns) were optimized to ensure complete dumping of a single resonant pulse. To confirm that the AOM was only active on a single pulse traveling towards the OC, a pair of photodiodes was employed. One monitored the beam dumped as it travelled from M_6 to M_7, while the second was aligned to detect accidental dumping of light traveling from M_7 to M_6, which occurred if the arrival time or duration of the electrical pulse activating the AOM was wrong. This approach guaranteed the most efficient energy extraction.

5.2.3 Pulse characterization

The OPO produced pulses, which were centred in wavelength around 1.535 µm, and barely tunable because of constraints associated with the reflectivity profile of the available mirrors. Tuning to longer wavelengths caused excessive losses while tuning to a shorter wavelength forced the OPO to tune rapidly through its zero-dispersion causing the pulses to break up. The OPO dispersion was strongly influenced by operating at the long wavelength edge of the mirror coating, involving a balancing act between losses and dispersion.

An example of an autocorrelation measured at a dumping frequency of 0.957 MHz (f_{REP} / 16) is shown in Figure 5.7(a) and its corresponding spectrum appears in Figure 5.7(b). The pulse duration was estimated by adding quadratic, cubic, and quartic spectral phase to the measured spectrum to find a pulse whose autocorrelation corresponded best with the experimental measurement. The red line in Figure 5.7(a) shows the resulting fit produced by the pulse shown in Figure 5.7(c), whose FWHM duration was 410 fs. It has been difficult to get the fit with good agreement. None of the three measurements taken from the cavity-dumped beam led to a satisfying fit. We believe this was due to the instability caused by the coating constrains mentioned earlier and possible a nonlinear phase introduced through self-phase modulation by the focused beam into the TeO_2-crystal.

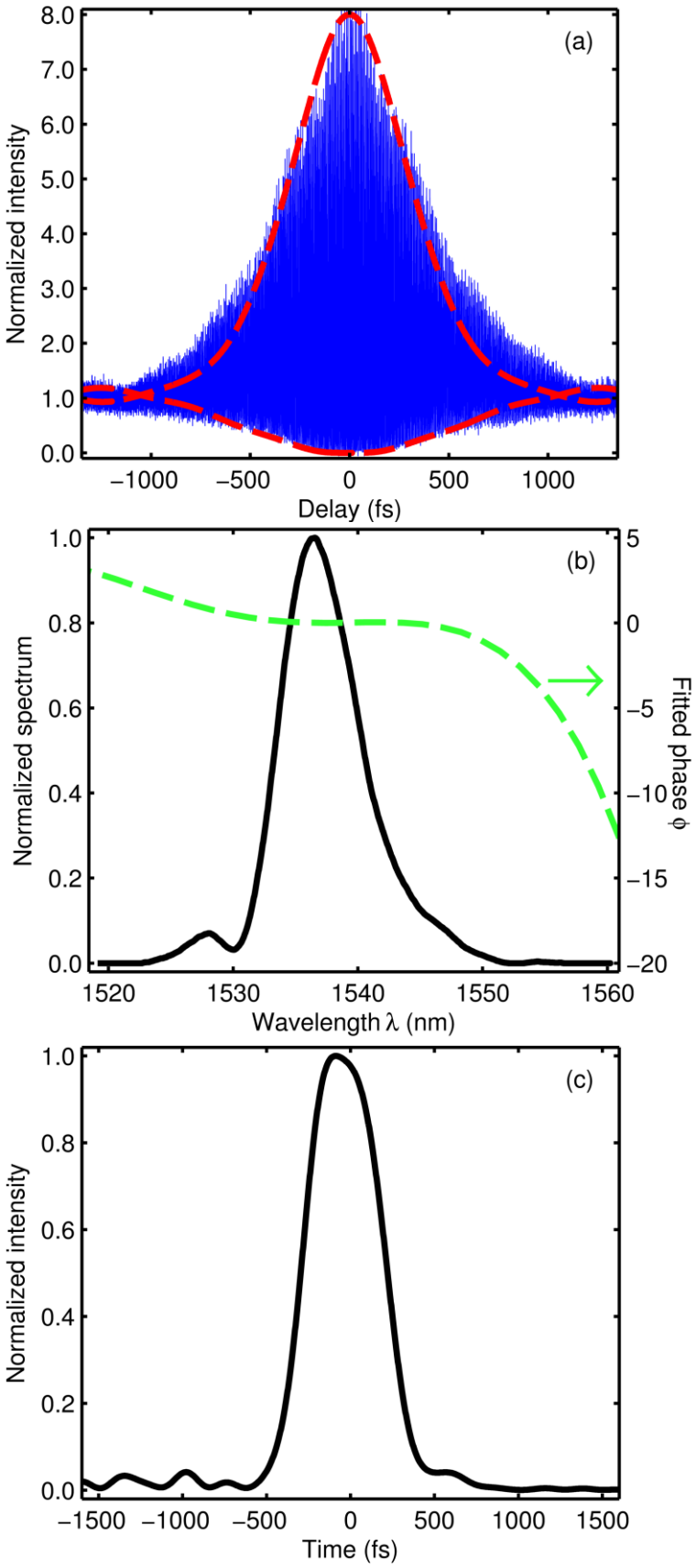

Figure 5.7. (a) Autocorrelation and (b) corresponding spectrum of the cavity-dumped signal pulses, recorded at a dumping frequency of 0.957 MHz. The best-fit autocorrelation envelope, shown as the dashed red line in (a), corresponds to the intensity (solid black lines) and phase (dashed green line) profiles shown in (b) and (c).

5.2.4 Cavity-dumping performance

The maximum average power extracted in the cavity-dumped beam was 1.05 W at a frequency of 3.8 MHz. This power is only slightly lower than the highest obtained through the OPO output coupler (1.09 W), implying that the cavity dumper introduced only minor parasitic losses. The calculated pulse energies were corrected to a lower value than that inferred directly from the diffracted average power because any pulse traveling from M_7 to M_6 experiences parasitic reflections from both faces of the AOM that contribute to the power measured in the diffraction direction. Acquiring simultaneously the power transmitted through the output coupler in steady state $P_{OC,SS}$ as well as the back-reflected power from the AOM in steady $P_{AMOref,SS}$ allowed us to calculate a steady state calibration factor κ_{SS} using the relation:

$$\kappa_{SS} = \frac{P_{AMOref,SS}}{P_{OC,SS}}. \qquad 5.19$$

For each cavity-dumped power measurement $P_{\text{measured},CD}$ a synchronous measurement of the output-coupled power $P_{OC,CD}$ was performed. This enabled us to calculate the real cavity dumped power $P_{real,CD}$ by subtracting the inferred reflected power applying the previously obtained calibration factor as following:

$$P_{real,CD} = P_{measured,CD} - \kappa_{SS} P_{OC,CD}. \qquad 5.20$$

All presented results shown here, represent solely corrected values and therefore represent the real single-pulse energies and peak powers respectively. This correction is only necessary if a standing-wave resonator is employed since a ring cavity, where the light propagates unidirectionally, would not show any residual power while the AOM remained inactive.

Power extraction with the cavity-dumper was achieved for dumping frequencies from 101 kHz (f_{REP} / 151) to 3.83 MHz (f_{REP} / 4). Figure 5.8 shows the average output power and pulse energy for the cavity-dumped pulses. The highest cavity-dumped pulse energy was 650 nJ, representing the current record pulse energy extracted from any ultrafast OPO.

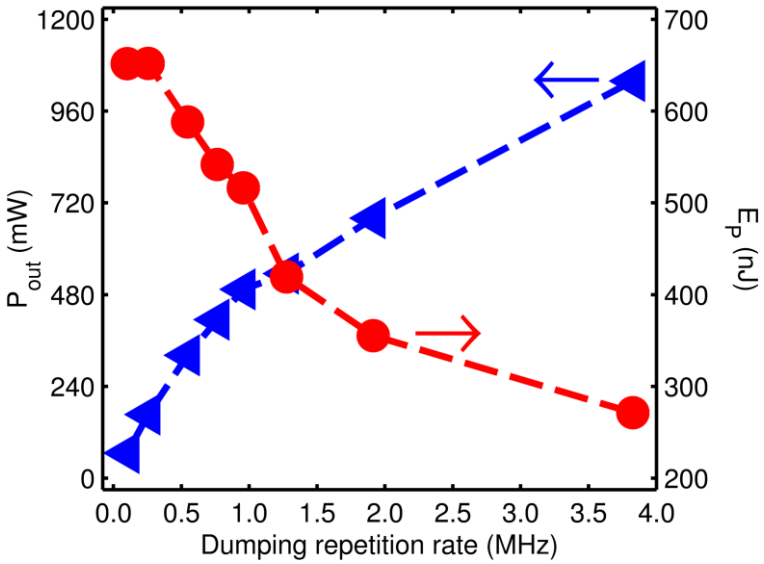

Figure 5.8. Extracted power (left ordinate) and energy (right ordinate) from the cavity dumped system over a range dumping rate from 100 kHz to 3.8 MHz.

5.3 Dispersion-compensated cavity-dumped optical parametric oscillator

5.3.1 Dispersion compensation

In order to address the problems of dispersion compensation an intracavity prism-pair was considered. Due to the very limited tuning range of the OPO, a measurement of the cavity net dispersion was not feasible. Instead, an investigative approach was taken in order to gain some insight of the individual contributions of each element to the net dispersion of the OPO to allow us to estimate the required amount of additional negative dispersion requirements for compensation.

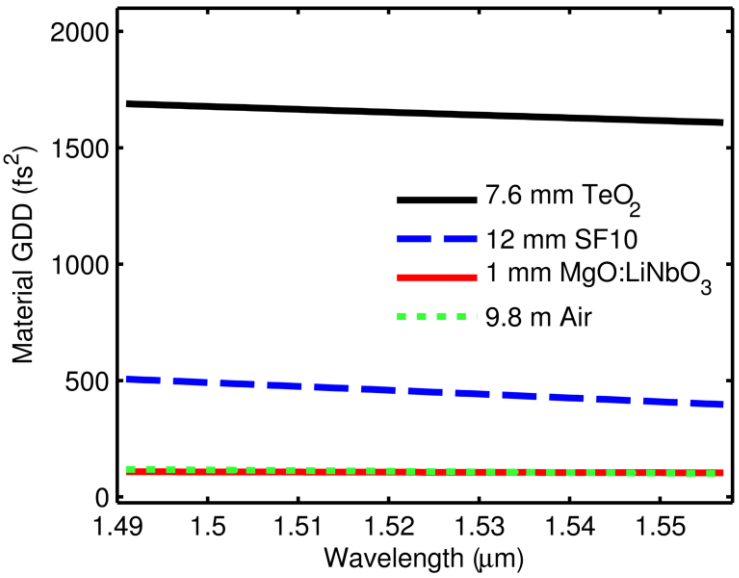

Figure 5.9. Calculation of the individual single pass dispersion (GDD) which contribute to the net dispersion of the cavity consisting of the 7.6 mm TeO_2 crystal, an approximated 12 mm pass length trough SF10 glass introduced by the additional prism pair, the 1 mm long MgO:$LiNbO_3$ crystal, and 9.8 m of Air.

5.3.1.1 Dispersive elements

Each element inside the resonator was investigated for its group delay dispersion (GDD). The GDD for a single pass was calculated from the refractive indices assessed through Sellmeier coefficients for the 9.8 m in free space air [67], the 1 mm 5%MgO:PPLN-crystal [68] at 80°C, for the TeO_2-crystal with 7.6 mm path length [69]. The individual GDDs over a wavelength range from 1490 to 1560 nm are plotted in Figure 5.9 along with the GDD for an additional path through 12 mm SF10 glass [70], introduced with a pair of prisms used for active dispersion compensation.

The dispersion contributed by the mirror coating was not known, however at 1530 nm it was sufficient to compensate for the dispersion introduced by the air path, MgO:PPLN-, and TeO_2-crystal of about -1900 fs^2. Since the measured transmission for the coating of the OPO mirrors was available, we tried to estimate the GDD contribution of the 10 mirrors by fitting the number of layer pairs and their refractive index and extracting the phase returned from the complex reflectivity [71]. In Figure 5.10(a), an overlay of the measured and fitted curve is presented, showing very good overlap in the high reflectivity range from 1250 to 1550 nm. In Figure 5.10(b), the group-delay dispersion was plotted and a close-up in Figure 5.10(c), covering the interesting range from 1500 to 1560 nm.

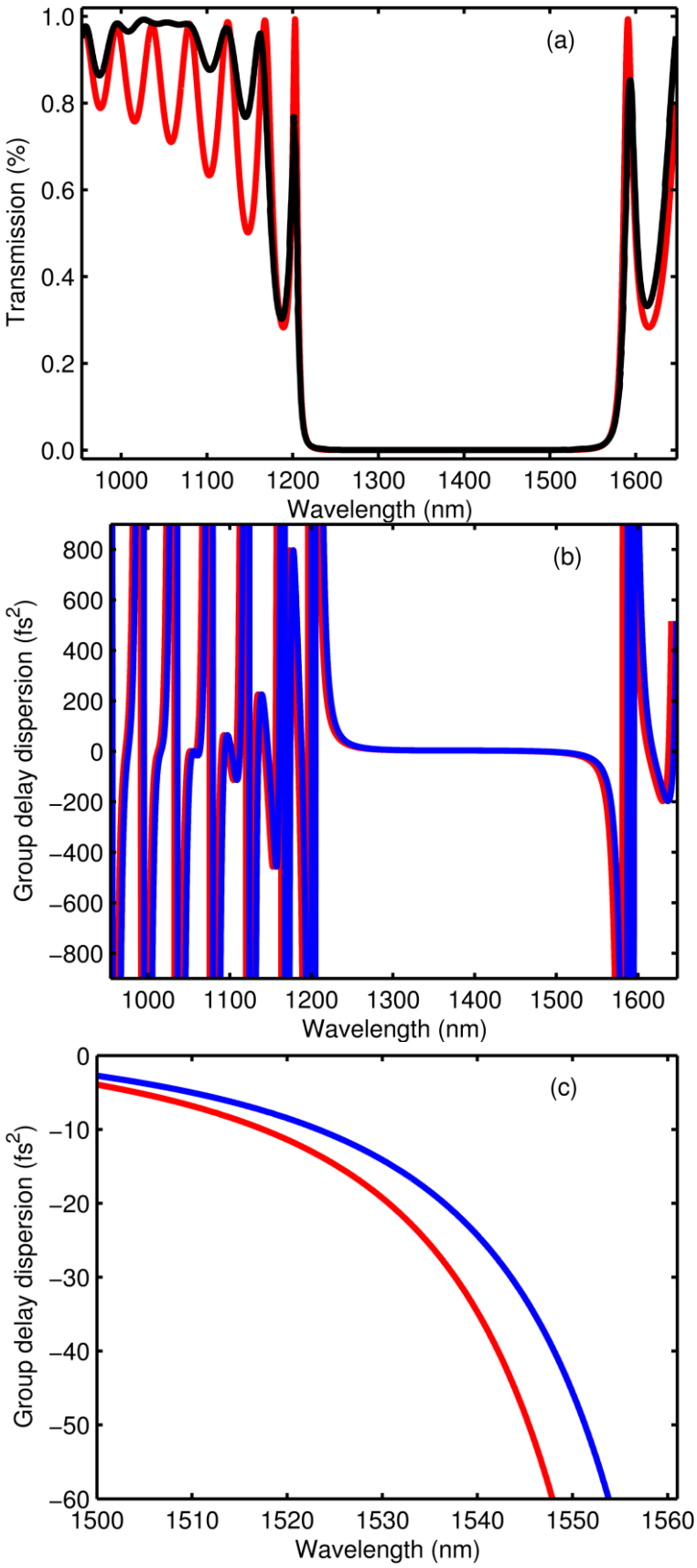

Figure 5.10. (a) Measured (black) and fitted (red) mirror reflection based on an estimate of the coating layers thickness and numbers. (b) Estimated dispersion of a single mirror based on the reflection curve in (a). (c) A close up in the region from 1500 to 1560 nm. For (b) and (c) blue line represents normal incidence, red line was at 5° angle of incidence, respectively.

In Figure 5.10(b) Figure 5.10(c) the red lines indicate the contribution for a beam incident with 5° rather than at normal incidence presented by the blue lines.

The GDD estimated in this way only provides a contribution of -150 to -200 fs^2 for the 10 mirrors at 1530 nm. The result differs by more than a factor of 10 to what was predicted by the calculations of the individual GDD contributions. Estimating the mirror dispersion by fitting the phase contribution of the stacked layers did not correspond well with the experimental observations.

A further influence that limits the tunability at the current wavelength is the atmospheric transmission window with a strongly increasing absorption below 1540 nm. The absorption at 1525 nm reaches already 1%, rapidly increases above 5% at 1500 nm. Figure 5.11 shows the atmospheric transmission at ground level from 1475 nm to 1800 nm, revelling very strong modulation (blue line was the raw data) with an overlaid plot of the data averaged (red line) on top.

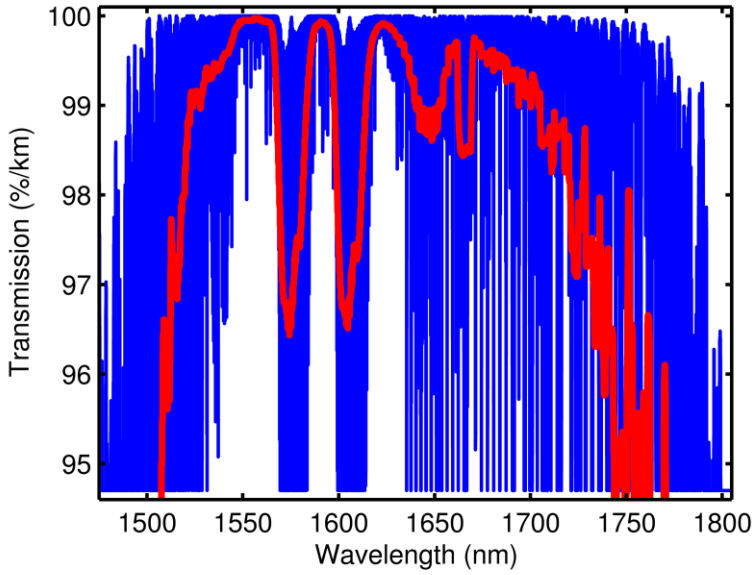

Figure 5.11. Atmospheric transmission at ground level (blue line) and averaged over 350 points (red line). Raw data were provided with courtesy to the Gemini Observatory [72] and NASAs ATRAN project.

The constraints introduced by the mirror coating at the long wavelength edge on one hand and the absorption losses at short wavelengths on the other hand, narrow the tunability of the presented OPO substantially. However, providing a mirror coating with good reflectivity could enable one to access the wavelength from just above 1500 nm to almost 1750 nm.

5.3.1.2 *Intracavity prism-pair for dispersion management*

Following the approach presented by Fork *et al.* [17] the required separation of a prism pair, based on SF10 glass, was calculated in order to introduce an additional negative dispersion of -1000 fs^2 with consideration of the extra dispersion introduced by the prisms themselves. A separation of 490 mm was calculated to generate -1000 fs^2 with the contribution of 12 mm added glass per pass.

To evaluate the single pass net dispersion of the compensated OPO cavity a measurement of the centre wavelength λ_c against cavity length l (used to measure the roundtrip time τ) was performed. The relation

$$GDD = \frac{d\tau}{d\omega_c} = \frac{d\frac{l}{c_0}}{d\frac{2\pi c_0}{\lambda_c}}, \qquad 5.21$$

was used to generate the plots shown in Figure 5.12 for 3 individual measurements. The separation of the prism was found to be approximately correct and allowed the OPO to operate at a more efficient wavelength away from the reflectivity edge of the mirror coating.

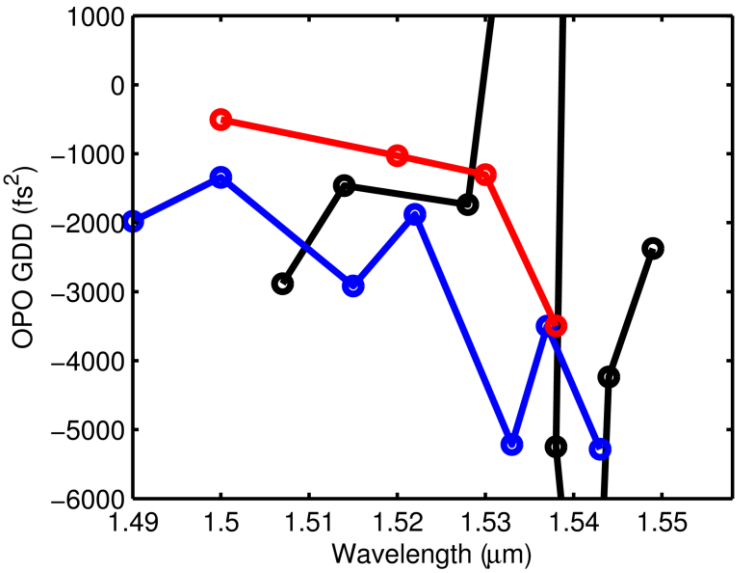

Figure 5.12. Results of three measurements to determine the cavity net dispersion after the prisms were introduced into the cavity.

5.3.2 *Cavity layout of the dispersion compensated cavity-dumped OPO*

The changes made to introduce the intra-cavity prism-compressor are outlined in Figure 5.13. Between mirror M_2 and M_{1a}, a pair of prisms (P_1 and P_2) was aligned at Brewster's angle and minimum deviation [73] and 480 mm separation, redirecting the beam to mirror M_{1b} as the new end mirror. Prism P_1 was introduced iteratively into the oscillating cavity, sampling only a small portion of the beam in order to find the position of minimum deviation as well as to align the second prism and the new end mirror. This allowed us to keep both arms synchronous being able to switch between compensated and uncompensated cavity setup only by moving prism P_1. The long arm, holding the AOM, remained unchanged and complies with the description given in section 5.2.1.

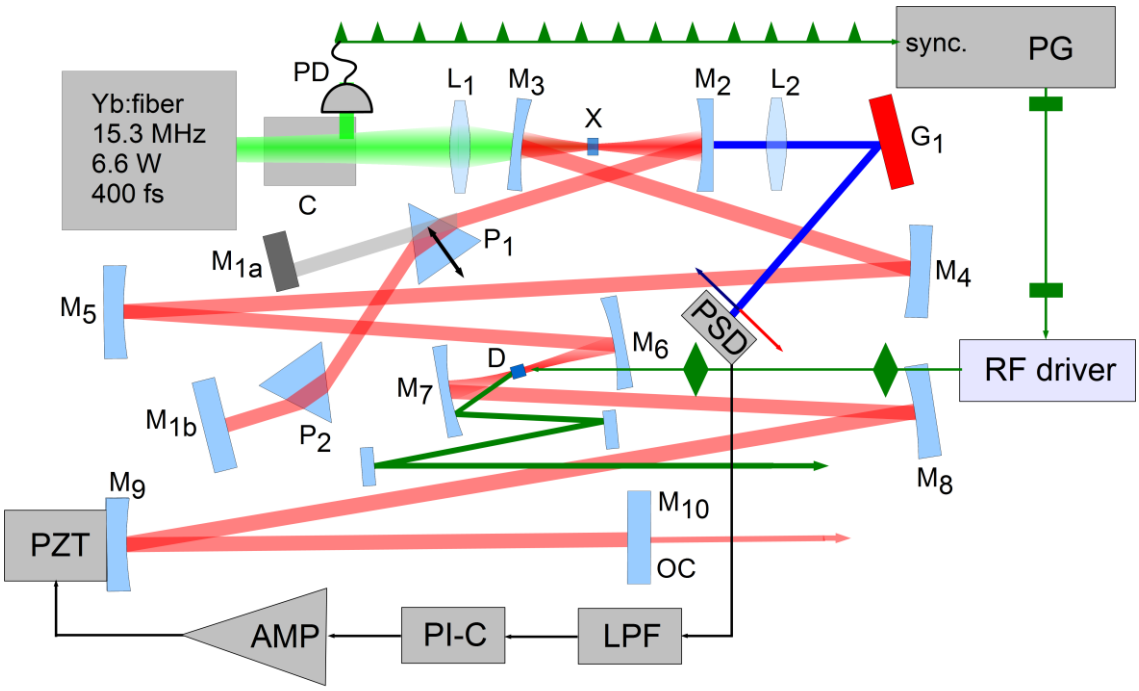

Figure 5.13. Cavity layout: PG, pulse generator; LPF, low-pass filter; C, compressor; PD, photodiode; X, MgO:PPLN crystal; D, AOM cavity-dumper. See text for other definitions.

5.3.3 *Improved dumping electronics*

The implementation of the cavity-dumping electronics was improved by replacing the pulse generator triggered by the frequency-divided signal of the laser repetition rate with a pulse generator (Quantum Composers, 9534-TZ50-DT15-EU) with the capability

to phase-lock its internal clock-frequency directly to the signal delivered from a fast photodiode.

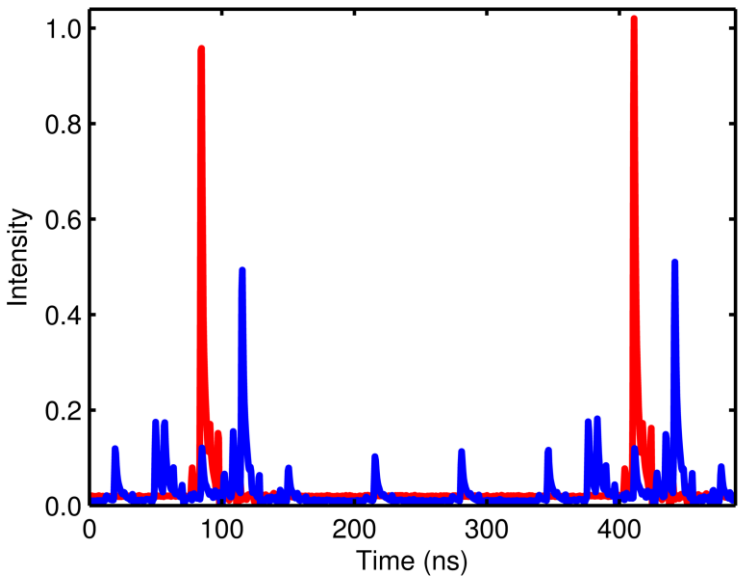

Figure 5.14. Pulse monitoring at 3 MHz of the forward traveling dumped pulse (red) and the unintentionally dumped returning pulse superimposed with the reflected pulses (smaller peaks) form the AOM facet (blue).

This approach provided a much more reliable source of pulses with a nominal decrease in timing jitter by a factor 20. Pulses from the new pulse generator followed the identical path of the previous setup, where they were fed into the analogue-modulation input of a radio-frequency (RF) driver (Gooch and Housego, A35110) which supplied a 110-MHz carrier signal to the AOM (Gooch and Housego, M110-2H/GJ). The delay (65.2 ns) and duration (35.4 ns) were optimized to ensure complete temporal dumping of a single resonant pulse. The confirmation that the AOM was only active on a single pulse traveling towards the OC, a pair of photodiodes was employed for monitoring. One photodiode observed the beam dumped as it travelled from M_6 to M_7, while the second was aligned to detect accidental dumping of light traveling from M_7 to M_6, which occurred if the arrival time or duration of the electrical pulse activating the AOM was wrong. Figure 5.14 illustrates the signals observed in this way.

The OPO included active wavelength stabilization as described in Chapter 4, enabling stable long-term operation and achieving a relative intensity noise (RIN) for the output-coupled pulses approaching that of the Yb:fibre pump laser. The feedback loop sensed the OPO wavelength by detecting the non-phase-matched second-harmonic signal light ($\lambda \sim 760$ nm) leaking through mirror M_2. This beam was then dispersed by grating G_1

and focused by lens L_2 onto a position-sensitive detector (PSD) to derive an error signal which was low-pass filtered (LPF) at 15 Hz before entering a proportional-integral controller (PI-C) and a high voltage amplifier (AMP), whose output displaced mirror M_9 via a piezoelectric transducer (PZT) accordingly. The setup of the cavity feedback is almost identical to what was presented in Chapter 3. The amplifier for the piezo transducer was replaced by a low noise, DC to 50 Hz high voltage active feedback amplifier (Falco Systems, WMA-01LF). Furthermore, between the error signal from the position-sensitive detector and the PI-controller a first-order LPF was employed which greatly suppressed supressed noise in the higher frequency range.

5.3.4 Cavity-dumping performance

5.3.4.1 Pulse characterization

The cavity-dumped OPO produced pulses centred in wavelength around 1.52 µm. The tunability was improved due to the prism-pair relaxing the constraints slightly, nevertheless, only a limited range was accessible because of opposing constraints associated with the reflectivity profile of the available mirrors and the periods of the gratings on the MgO:PPLN crystal. The OPO, dispersion-compensated by a SF10 prism pair, operated with a net cavity group-delay dispersion (GDD) at about ~ -1000 fs^2, which ensured the generation of clean, near-transform-limited pulses.

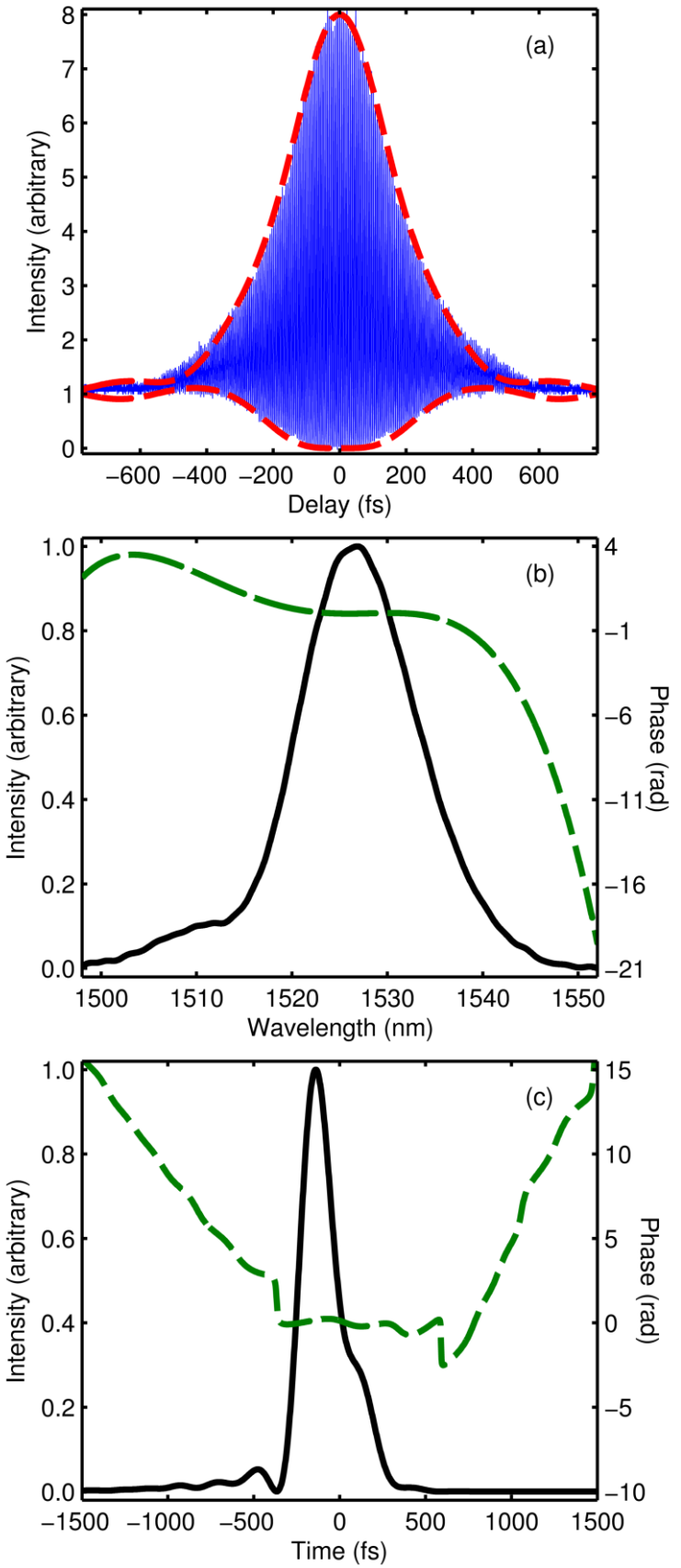

Figure 5.15. (a) Autocorrelation and (b) corresponding spectrum of the cavity-dumped signal pulses, recorded at a dumping frequency of 3.06 MHz. The best-fit autocorrelation envelope, shown as the dashed red line in (a), corresponds to the intensity (solid black lines) and phase (dashed green lines) profiles shown in (b) and (c). The results shown here were acquired from the dispersion-compensated OPO.

An example of an autocorrelation measured at a dumping frequency of 3.06 MHz (f_{REP} / 5) is shown in Figure 5.15(a), and its corresponding spectrum appears in Figure 5.15(b). The pulse duration was estimated by adding quadratic, cubic, and quartic spectral phase to the measured spectrum to find a pulse whose autocorrelation corresponded best with the experimental measurement. The red line in Figure 5.15(a) shows the resulting fit produced by the pulse shown in Figure 5.15(c), whose FWHM duration is 228 fs. The results shown were obtained for a pulse energy of 280 nJ, which implies a peak power of 0.94 MW.

5.3.4.2 Beam quality measurements

Diffraction from an AOM occurs throughout the bulk of the modulator, not at a single plane as in a conventional diffraction grating. For this reason, it is important to quantify the effect of cavity dumping on the beam quality of the dumped pulses. We measured the beam-quality parameters of the output-coupled and cavity-dumped beams in both the horizontal (X) and vertical (Y) directions. The horizontal direction corresponds to the diffraction direction and was therefore expected to be more severely affected by cavity dumping. For the output-coupled beam we recorded beam quality factors of $M_x^2 = 1.12$ and $M_y^2 = 1.06$, while for the cavity-dumped output we measured slightly higher values of $M_x^2 = 1.26$ and $M_y^2 = 1.16$. In each case, the data were acquired by using the scanning knife-edge technique to measure the $1/e^2$ beam radius at regular intervals after a 50-mm focal-length lens. The beam radius at each position was determined from the average of three independent knife-edge scans, and Figure 5.16 and Figure 5.17 presents the experimental data fitted for output coupled and cavity-dumping measurements respectively, using a procedure similar to that described in [74]. The measurements were recorded at a dumping rate of 3.06 MHz and correspond to pulse energies of 280 nJ.

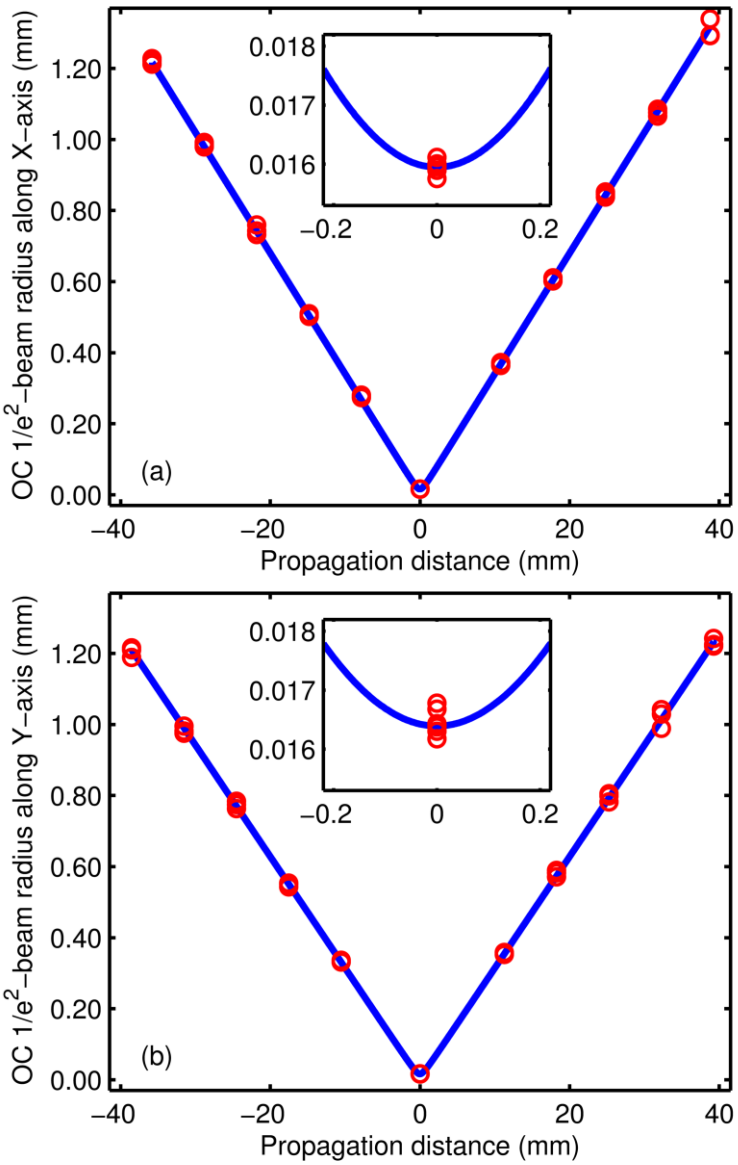

Figure 5.16. (a) Horizontal and (b) vertical beam radius measurements (circles) and fit to an M^2-corrected Gaussian-beam propagation equation (solid lines), with M^2 = 1.12 (horizontal) and M^2 = 1.06 (vertical) for the output coupled (OC) beam. The insets show horizontal and vertical waist radii of 16.39 µm and 16.40 µm respectively.

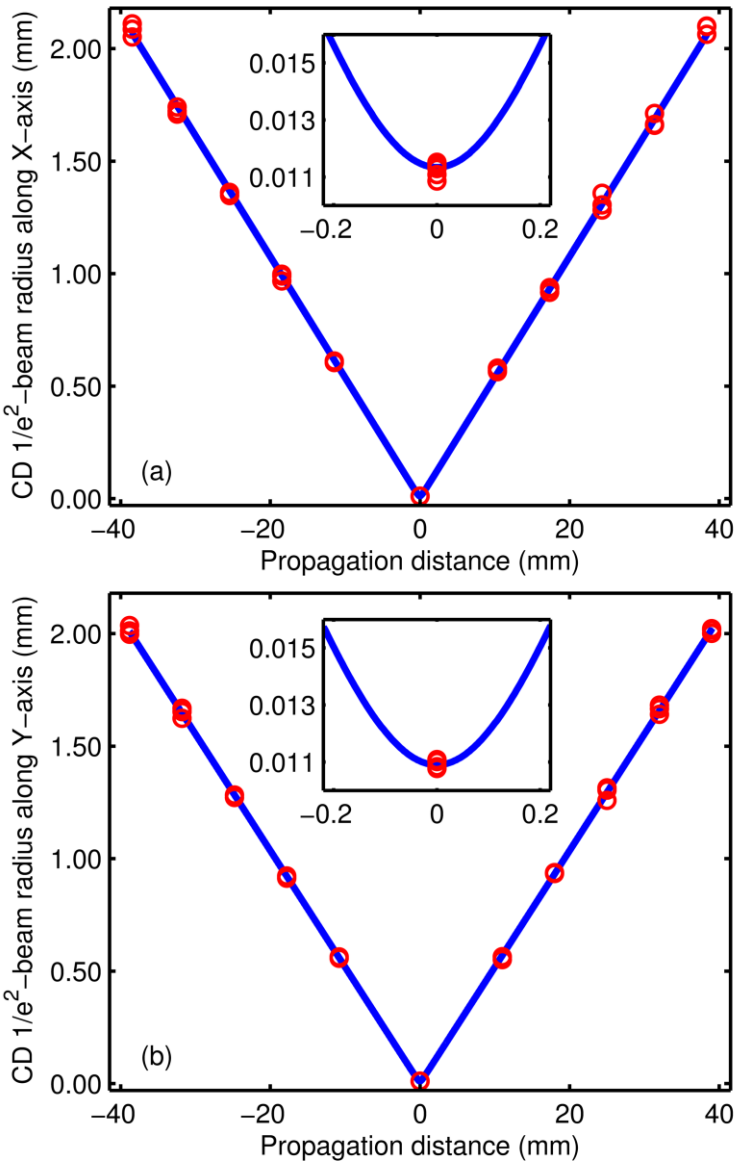

Figure 5.17. (a) Horizontal and (b) vertical beam radius measurements (circles) and fit to an M^2-corrected Gaussian-beam propagation equation (solid lines), with M^2 = 1.26 (horizontal) and M^2 = 1.16 (vertical) for the cavity dumped beam. The insets show horizontal and vertical waist radii of 11.3 µm and 10.9 µm respectively.

5.3.4.3 Relative intensity noise measurements

We recorded RIN performance over a frequency range of 4 mHz - 500 Hz for the pump laser, the output-coupled OPO signal pulses (cavity-dumper turned off) and the cavity-dumped OPO signal pulses at a dumping frequency of 3.06 MHz (f_{REP} / 5). For each case, Figure 5.18 shows the RIN data (left ordinate) and the total noise power integrated from high to low frequencies (right ordinate), whose maximum value is equivalent to the time-domain root-mean squared (RMS) noise. The acquisition time for each measurement was 250 seconds, which provided sensitivity to medium- and long-term variations of the kind associated with acoustic and thermal noise. Comparing the

measurements, we found that the RMS noise on the output-coupled OPO pulses was 1.11 times the pump RMS noise, while the RMS noise of the cavity-dumped pulses was 2.13 times the RMS noise of the pump. In absolute terms, the RMS noise of the cavity-dumped OPO was still very low, with a value of 8 mdBc^2 corresponding to 0.2% RMS noise.

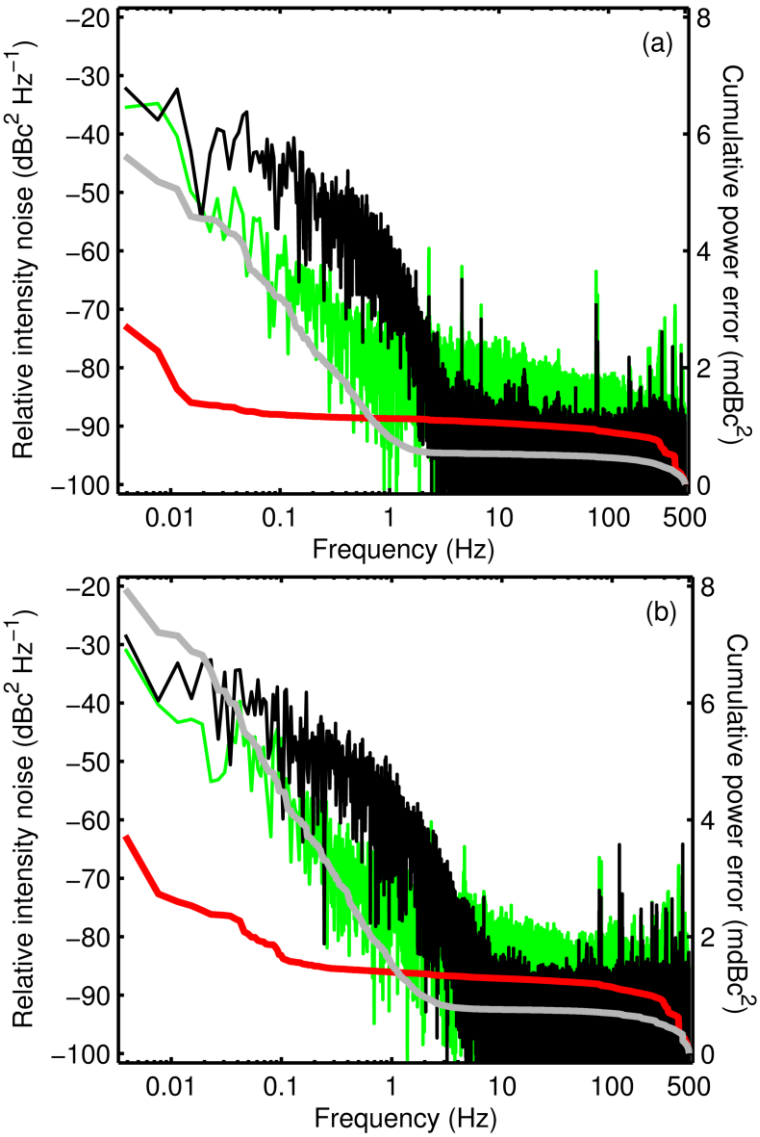

Figure 5.18. (a) Comparison of the RIN measured for the pump laser (green) and the output coupled (T=22%) OPO signal pulses (black) at the maximum average output power of 1.26 W. (b) Independent RIN measurement of the pump laser (green) and comparison with the cavity-dumped (3.06 MHz) OPO signal pulses (black) at the maximum average output power of 1.1 W. On both graphs, the right axis shows the cumulative power error integrated from high to low frequencies for the pump laser (red) and OPO (grey).

A comparison between these RIN results and the one presented in Figure 4.11 on page 80, shows, that the low-pass filter is quite effective down to a frequency of 7 Hz.

5.3.4.4 *Dumping efficiency and pulse build-up*

Figure 5.19 shows the signal pulse sequence detected after the output-coupler (T = 1.75%) with an InGaAs photodiode (Thorlabs, DET10C/M). The blue pulses are the fundamental pulses at f_{REP} and the cavity was dumped at a frequency of 154 kHz (f_{REP} / 99). The data indicate a dumping efficiency of 83%, and the red solid line shows an exponential fit corresponding to time of 1.38 µs for the intracavity pulses to recover to 90% of their steady-state energy. The data in Figure 5.19 provide a convenient estimate for the unsaturated gain, implying a value of ~1.5, consistent with results from an earlier Rigrod analysis [74] presented in section 3.4.1.

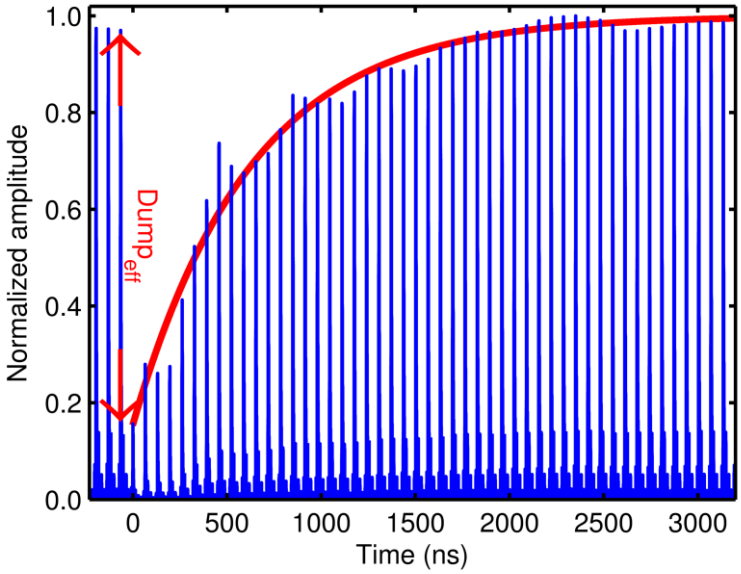

Figure 5.19. Signal pulse sequence measured after the output coupler at a dumping frequency of 154 kHz. The dumping efficiency is determined from the change in the signal before and after dumping (indicated by the red arrows).

5.3.4.5 *Power, energy and efficiency measurements*

Cavity dumping was studied for dumping frequencies from 101 kHz (f_{REP} / 151) to 3.83 MHz (f_{REP} / 4) and data were recorded corresponding to the OPO operating with and without the dispersion-compensating SF10 prism pair. Figure 5.20(a) shows the average output power and pulse energy from the system, and Figure 5.20(b) shows the same data re-plotted to illustrate the individual peak power of the cavity-dumped pulses. Peak powers were derived in a rigorous way from the estimated pulse profile (Figure 5.15(c)) in proportion to their individual pulse energies for the OPO with SF10 prisms. The peak powers for the uncompensated cavity were derived from an estimated pulse duration of 410 fs (assuming a transform-limited $\mathrm{sech}^2(t)$ temporal shape),

inferred from the 775 fs FWHM of their interferometric autocorrelation shown in Figure 5.7(a). Results with and without dispersion control are not directly comparable since the data from the OPO without prisms were obtained using a different pulse generator which was operated in trigger mode. Operated with the SF10 prisms the highest cavity-dumped pulse energy was 617 nJ, slightly lower than the highest energy of 650 nJ recorded from the OPO operated without the SF10 prisms. Pulse break-up in the absence of dispersion management meant that without prisms the OPO produced longer pulses with lower peak powers. The data in Figure 5.20(b) show that including dispersion control resulted in substantially higher peak powers (2.07 MW) than the best that could be obtained without prisms (1.4 MW).

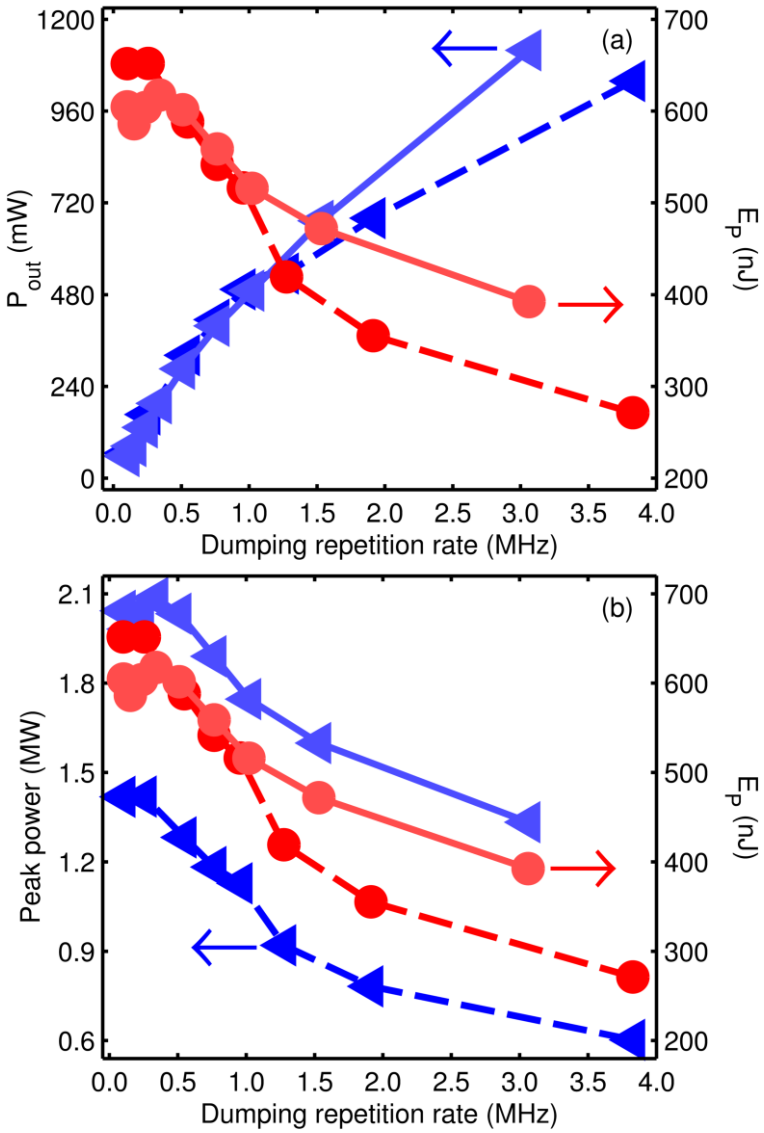

Figure 5.20. (a) Cavity dumped average power (blue triangles) and pulse energies (red circles) for dumping frequencies from 101 kHz – 3.83 MHz. (b) Cavity dumped peak power (blue triangles) and pulse energies (red circles) for the same dumping frequencies. In both figures, the solid and dashed lines indicate results obtained from the OPO operated with and without SF10 prisms for dispersion control respectively.

The maximum average power extracted in the cavity-dumped beam was 1.1 W at a rate of 3.06 MHz. This is only slightly lower than the highest obtained signal power extracted through a 22% output coupler resulting in 1.26 W while the AOM was left inactive in the cavity beam. With the previously gained dumping efficiency of 83% and the maximal available extraction of every fifth pulse (3.06 MHz) a maximum effective output of 83% / 5 = 16.6% is achievable. Considering the Rigrod curve presented in section 3.4.1, the extraction of 1.1 W at 16.6% this is within the tolerance of the presented results. For maximum power, extraction of every third pulse (83% / 22% > 3.77) would be necessary. With an improved pulse generator, dumping

rates at the fundamental repetition rate would be feasible, presenting the possibility of using the dumper effectively as a variable output coupler. The presented powers, pulse energies, and peak powers, were corrected to a lower value than that measured directly from the diffracted average power according to the principles explained in paragraph 5.2.4.

5.4 Conclusions

Sub-250-fs pulses with energies of up to 650 nJ and peak powers up to 2.07 MW were generated from a cavity-dumped optical parametric oscillator, synchronously pumped at 15.3 MHz with sub-400-fs pulses from a commercial Yb:fibre laser. The system maintained pulse energies ≥ 392 nJ and peak powers ≥ 1.3 MW over a repetition range from 101 kHz – 3.06 MHz. The average beam quality factor of the dumped output was $M^2 \sim 1.2$ and the total relative-intensity noise was 8 mdBc^2, making the system a promising ultrafast laser source for scientific applications.

Chapter 6 - Modelling of a cavity-dumped ultrafast optical parametric oscillator

6.1 Introduction

In this chapter a more analytic approach is presented in order to gain an insight of the possibilities and limitations associated with cavity dumping of ultrafast synchronously pump optical parametric oscillators. Cavity dumping is employed to extract individual pulses with much high energies at a sub-harmonic of the fundamental laser repetition rate, at the expense of average power and repetition rate, where usually the cavity is operated in a low-loss regime allowing a build-up of very high intracavity powers. In the last 20 years, cavity-dumping has turned into a widely used technique in ultrafast lasers developed for scientific applications [75–78] and commercial products [58] equally. From the mid-1990s, the technique was applied to Ti:sapphire lasers, readily increasing the extracted pulse energies by an order of magnitude [75,76,79,80]. More recent developments include the successful dumping of Yb:KYW ultrafast oscillators [77,81], including a passively mode-locked femtosecond thin-disk oscillator extracting up to 3-µJ pulses [82]. Furthermore, oscillators based on Cr:fosterite [83], Nd:YVO_4 [84] and, in 2010, Cr:LiSAF [78] have been reported.

Despite the broad implementation in many different laser systems, cavity dumping of OPOs was only reported for three systems until now. The first cavity-dumped OPO was reported by Potma in 1998 [10], delivering 13 nJ at a wavelength of 630 nm and a dumping rate of 400 kHz. In 2005, Min and Joo reported an OPO based on a PPLN-crystal which was pumped with 9.8 nJ pulses from a Ti:sapphire laser. They were able to extract pulses at 1.2 µm wavelength with up to 80 nJ (single pumping) and 90 nJ (double pumping) for dumping-rates of 500 kHz and below. In 2011, we reported the cavity-dumped OPO described in Chapter 5, pumped by a high-power Yb:fibre laser and delivering pulses up to 625 nJ with a wavelength of 1.53 µm at dumping-rates of 255 kHz and below [85].

Cavity dumping promises great potential for OPOs because it offers pulse energies that are a magnitude higher than available with conventional output-coupling and still provides a broad tuning range for instance from 1.0 to 1.5 µm [11]. Cavity-dumped

OPOs therefore possess unique qualifications, which are not accessible with any other laser system, while dumping repetition rates are adjustable over ranges from Hz to MHz.

Passively mode-locked laser systems in particular are very sensitive against perturbations of the intracavity power. The balance between mode-locking and gain is controlled by the intracavity energies and the nonlinearity of the underlying mode-locking technique. The temporal interactions are therefore complex and ultimately limit how forcefully an individual system can be disturbed through cavity-dumping in terms of modulation depth and dumping rate. The temporal pulse shaping dynamics for a SESAM mode-locked cavity-dumped Yb:glass laser was extensively investigated by Killi and Morgner [86].

6.2 Simulation of cavity dumped OPOs

In 2001, Sevruk [87] investigated the dynamics of cavity-dumped OPOs with a numerical model. This paper investigated a pseudo Q-switching regime because the pump pulses were of several nanosecond length and therefore longer than the effective length of the investigated cavity of 6 cm (roundtrip time of 0.24ns). The simulation presented numerical results for OPOs operating in an intermediate CW-regime with output pulses in the nanosecond time domain. Therefore, the presented results are not suitable to predict the evolution of ultrafast pulses and the energies obtainable from a cavity-dumped synchronously pumped OPO. A more fundamental approach is therefore described next.

6.2.1 Introduction to the nonlinear envelope equation

Traditional modelling of optical parametric oscillators was based on a formal description of the exchange of energy between the pump, signal, and idler waves based on the second-order nonlinearity $\chi^{(2)}$, linked together with the three coupled-amplitude equations [88]. Although calculations can only be performed to calculate the energy exchange between three monochromatic waves, they were successfully applied to calculate nonlinear interaction between ultrafast pulses [89,90]. Any $\chi^{(2)}$-interaction with ultra-broad pulses or where more than three waves are interacting, which applies if effects such as frequency doubling, sum-frequency generation, or difference-frequency

generation occurs in parallel with the modelled parametric amplification, remain beyond the capabilities of the couple-amplitude equations and therefore do not provide a satisfying agreement with experimental results [91,92].

In 2010, Conforti and co-workers derived a nonlinear envelope equation (NEE) that describes the propagation of broadband optical pulses in media that exhibit $\chi^{(2)}$ nonlinearity. The equation was proved to be valid for arbitrarily wide pulse bandwidths and provides an accurate model of the evolution of ultra-broadband pulses, beyond the limitations of the conventional coupled wave description. Besides being able to simulate the separation into different coupled frequency components at the same time, a further key benefit of the nonlinear envelope equations is, that it takes much less computational effort than a rigorous simulation of Maxwell's equations.

Very recently, the the $\chi^{(2)}$ NEE was successfully exploited for studying the ultra-broadband pulse evolution in optical parametric oscillators, synchronously-pumped by a femtosecond laser [92]. The gain materials used in the simulations were QPM media, where the polarity of $\chi^{(2)}$ was modulated along the propagation direction with a period twice the coherence length of the intended $\chi^{(2)}$ process. However, under these circumstances, the underling grating can also quasi-phasematch any higher-order process whose coherence length is an odd divider of the grating period. This effect led to multiple simultaneous nonlinear processes, showing significant interaction across the intense fields that were present inside the simulated high-finesse OPO cavity and the obtained results correlated well with experimental results for the first time.

Now, we report an extension of the numerical SPOPO model, providing an insight to the dynamics of a cavity-dumped synchronously pumped optical parametric oscillator. Due to the accumulation of intra-cavity power over several cavity roundtrips, the field intensities inside a cavity-dumped OPO exceed those of a conventional output-coupled system by more than an order of magnitude if the intrinsic losses are kept at a minimum [11,85]. This motivated us to utilise the NEE in order to obtain accurate results despite the strong interaction that takes place during the build-up of the intracavity power of a cavity-dumped OPO. Therefore, we present for the first time simulated results of the dynamics of a cavity-dumped OPO and investigate the extractable energies for an extensive range of conditions by modifying the modulation

depth, dumping-rate, and the intrinsic losses of the cavity due to reflection and coating losses.

6.3 OPO simulation model

We started with the previous synchronously-pumped OPO model [92], where gain and dispersive propagation of the resonant pulses inside the nonlinear medium was addressed by the NEE, and was then followed by a complex spectral band-pass filter used to represent output coupling, parasitic losses, mirror reflectivity and cavity delay.

While parasitic losses and mirror reflectivity were evaluated as before, continuous output coupling was augmented with the modulation depth of an acousto-optic or electro-optic modulator activated every N^{th} round trip. At times when the modulator was inactive, the cavity experienced only the much smaller output coupling, intrinsic, and coating losses. The contribution of the Author was the implementation of a sequential alteration of the various parameters in a loop while maintaining the number of execution loops to a required minimum. The credits for the core of the simulation belong solely to my supervisor Derryck Reid.

The complex electric field envelope used for the simulation was defined by

$$A(z,t) = \tilde{E}(z,t)e^{-i\omega_0 t + i\beta_0 z}\,, \qquad 6.1$$

where $\tilde{E}(z,t)$ represents the inverse Fourier transform of the positive frequency components of the physical electric field, with ω_0 being an arbitrary reference frequency and β_0 the related wavevector. Propagation inside the nonlinear medium was modelled by [93],

$$\frac{\partial A}{\partial z} + iDA = -i\frac{\chi^{(2)}\omega_0^2}{4\beta_0 c^2}\left(1 - \frac{1}{\omega_0}\frac{\partial}{\partial \tau}\right)B\,, \qquad 6.2$$

with B defined by

$$B = A^2 e^{i\omega_0\tau - i(\beta_0 - \beta_1\omega_0)z} + 2|A|^2 e^{-i\omega_0\tau + i(\beta_0 - \beta_1\omega_0)z},$$

where $D = \sum_{m\geq 2}^{\infty} \frac{i^{m+1}}{m!}\beta_m \frac{\partial^m}{\partial t^m}$, $\beta_m = \frac{\partial^m k}{\partial \omega^m}\Big|_{\omega_0}$, and $\tau = t - \beta_1 z$, were used respectively for a transformation of the simulation coordinate, where the group velocity β_1^{-1} served as the reference. This co-moving frame enables us to appreciate the temporal walk-off between the individual dispersed waves while supressing the much bigger absolute change in position during a propagation roundtrip. The QPM patterning of the nonlinear medium, based on a MgO-doped periodically poled $LiNbO_3$ (MgO:PPLN) crystal, was represented by a position-dependent susceptibility of the form,

$$\chi^{(2)}(z) = \chi_{eff}^{(2)} \frac{sin\left(\frac{2\pi z}{\Lambda}\right)}{\left|sin\left(\frac{2\pi z}{\Lambda}\right)\right|}, \qquad 6.3$$

where $\chi_{eff}^{(2)}$ was the effective nonlinear susceptibility of the medium which is two times the effective nonlinear coefficient.

In order to solve equation 6.2, the linear part on the left-hand side was solved in the frequency domain and for the right-hand side a Runge-Kutta algorithm [94] was used to solve the second-order nonlinear differential equation in the time domain. Treating the linear part in the time domain and the nonlinear part in the frequency domain in small steps is known as the split-step Fourier method [95].

In order to provide optical feedback a complex spectral amplitude filter was implemented in the form of

$$H(\omega) = \sqrt{R}\, e^{-\ln 2[2(\omega-\omega_0)/\Delta\omega]^{10} - i(\omega-\omega_0)T}, \qquad 6.4$$

where the magnitude follows a super-Gaussian of full-width at half-maximum (FWHM) $\Delta\omega$, with a peak cavity reflectivity of R. This reflectivity represents the effective cavity reflectivity and balances out all the losses experienced during one roundtrip in the cavity. The time T determines the delay the cavity introduces and is

added to the resonant pulse once every cavity roundtrip. This delay is generally not equal to the delay between the pump and signal pulses because it is referenced to the centre of the co-moving frame (chosen to be static at λ =1.4 μm). Applying the complex spectral filter to the field, once it left the nonlinear medium, was simply done by multiplying it by the incident field amplitude:

$$A'(z,\omega) = H(\omega)A(z,\omega)\,. \qquad 6.5$$

In order to complete a full cavity roundtrip, the filtered field $A'(z,\omega)$ was then added to the previous input in equation 6.2 to form a new input field ready for the next propagation through the nonlinear QPM medium.

To implement cavity dumping, the reflectivity of the output coupler within the amplitude reflection coefficient R, was set to unity, leaving parasitic losses and mirror reflectivity as the remaining losses applied after each roundtrip. Output losses were only subtracted from the intracavity field every N^{th} round-trip by a proportion equal to the depth of the simulated modulator, M_{depth} , according to

$$A'_{out}(z,\omega) = M_{depth}\, A'^{(z,\omega)}\big|_{i_{roundtrip}=N^{th}}\,, \qquad 6.6$$

and

$$A''(z,\omega) = \left(1 - M_{depth}\right) A'^{(z,\omega)}\big|_{i_{roundtrip}=N^{th}}\,, \qquad 6.7$$

where $A''(z,\omega)$ represents the remaining amplitude for optical feedback after the cavity was dumped.

It is worth mentioning that the numerical model is self-starting by providing a broadband, low-intensity signal pulse centred at a wavelength phasematched by the chosen grating. This quasi-quantum noise seed allows the model to rech a steady state within about 40 roundtrips. The pump field for the presented results was a transform-limited Gaussian pulse with FWHM duration of 400 fs and the pulse energy set to

100 nJ corresponding to the pump field amplitude of $\sqrt{2I/n_p c\varepsilon_0}$ where I is the pulse intensity averaged across its beam radius and n_p is the refractive index at the pump wavelength inside the nonlinear crystal.

6.4 Results and discussion

We employed the model to simulate an OPO pumped with a pulse energy of 100 nJ, a centre wavelength of 1060 nm and a transform-limited Gaussian pulse duration of 400 fs (FWHM). The phasematching grating periodicity was set to 29.9 µm to ensure a conversion of the signal wavelength to 1500 nm and idler to 3600 nm. The results are presented in cavity roundtrips rather than absolute dumping frequency to provide more generalised, repetition rate independent results, useful across systems with similar pump pulse and QPM-conditions.

Each individual run was based on an initial build-up of either at least 40 roundtrips or the number of undumped roundtrips, whichever was greater. Once the initial build-up was passed, the cavity was dumped at the appropriate rate. The number of dumping-cycles was adjusted for each choice of dumping frequency to allow each simulation to reach a steady state, such that consecutive dumps yielded the same energies, while maintaining the simulation time at the necessary minimum.

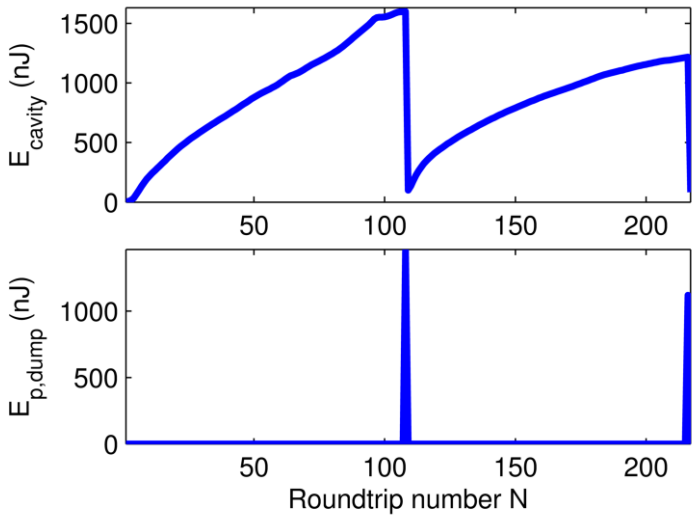

Figure 6.1. Example of the intracavity pulse build-up (top) for the case where $R = 97\%$ and the cavity is dumped at every 108th roundtrip. The bottom graph shows the first and second dumping event.

In Figure 6.1, the sequence for dumping every 108th roundtrip is shown, and for all the results shown afterwards, only the energy of the final dumped pulse was recorded. Based on that procedure, numerous simulations were performed while individual parameters were altered. These results were used to generate parameter maps comparing extracted energies for variations of modulation depths, dumping rates, and cavity losses.

Figure 6.2 shows the extracted energies for a variation of the dumper modulation depth over cavity roundtrips containing data from 180 individual simulations. The maximum energy, available at 108 roundtrips and 95% dumping efficiency was 417.5 nJ assuming intrinsic cavity losses of 8%.

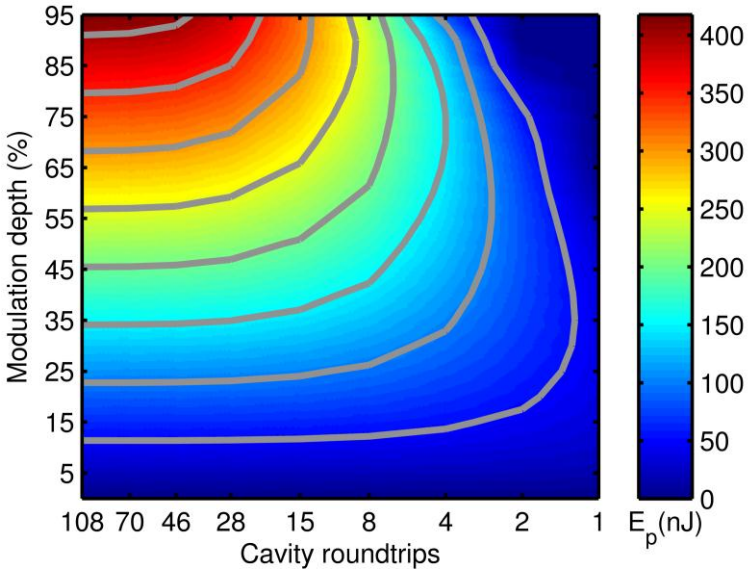

Figure 6.2. Cavity-dumped pulse energy dependence on modulation depth and cavity roundtrips. Here a roundtrip of 1 corresponds to the classical case of output coupling where each roundtrip pulse is extracted.

The grey lines indicate levels of equal energy with a separation of 50 nJ. The region where the isoenergy lines become horizontal means that, despite the increased number of cavity roundtrips, no more energy was extractable. This region is dominated by the intrinsic losses of the cavity. By increasing the modulation depth or increasing the dumping rate, the extractable energies become increasingly dictated by the modulator.

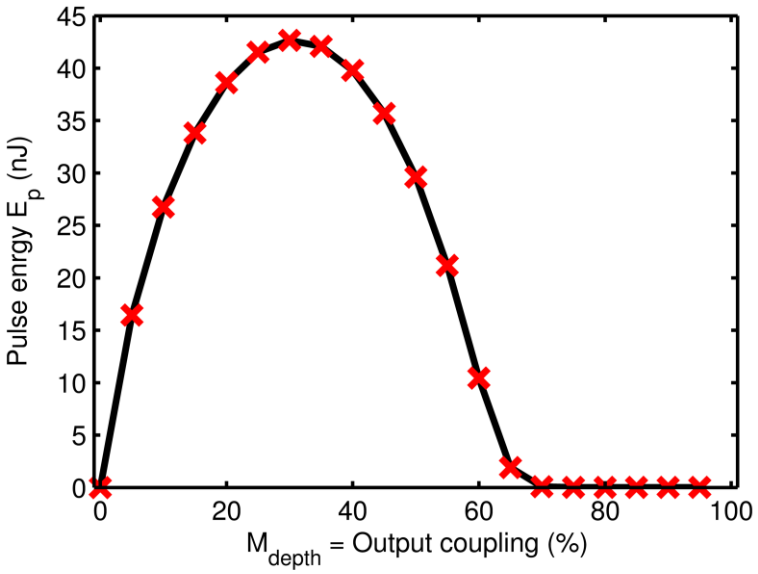

Figure 6.3. Rigrod plot of the pulses dumped at the fundamental repetition rate.

Increasing the modulation depth beyond the point where the maximum gain efficiency of the OPO lies, results in decreasing energy equal to over-coupling. The results taken for various modulation depth at every roundtrip ($N = 1$), represents the classical case of output coupling. The extracted energies in this instance are plotted in Figure 6.3 and embody a classic Rigrod [35] output-coupling plot. The maximum pulse energy extracted with cavity dumping was 417.5 nJ and the situation comparable to output coupling retuning 42.7 nJ, presents an energy extraction increase of 9.8.

In a next set of simulations, we investigated the influence of the intrinsic cavity losses, which was kept at constant value of 8% in the previous set of simulations. In Figure 6.4 results of 90 different simulations, varying the cavity losses and the dumping rate are shown.

The isoenergy lines indicate a separation of 100 nJ and again became horizontal where longer build-up times do not increase the extractable energy further, limited only by the intrinsic losses of the cavity.

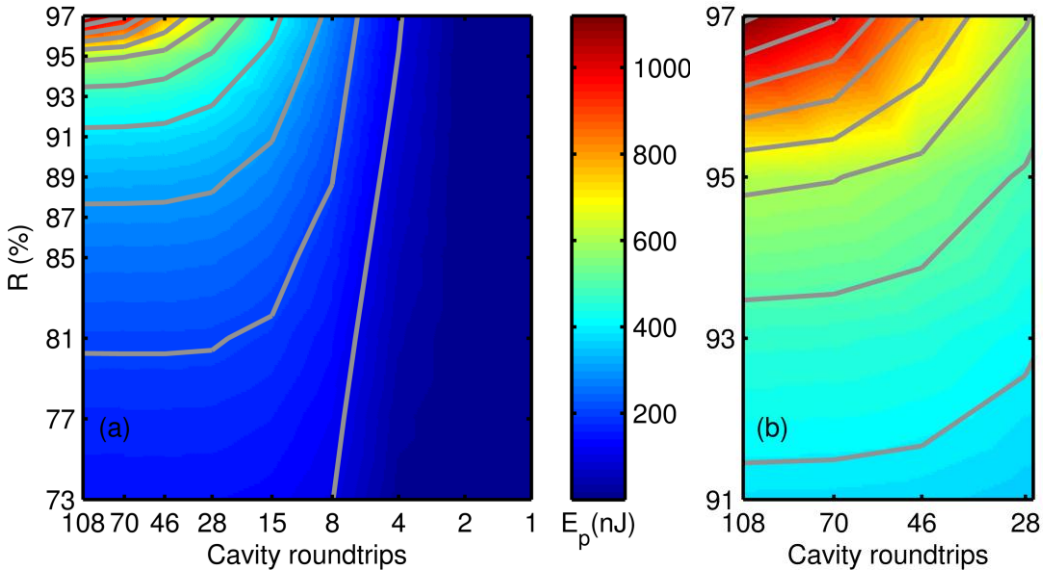

Figure 6.4. (a) Cavity-dumped pulse energy dependence on cavity reflectivity and cavity roundtrips. (b) Shows a close-up of the top-left corner where the highest energies were extracted.

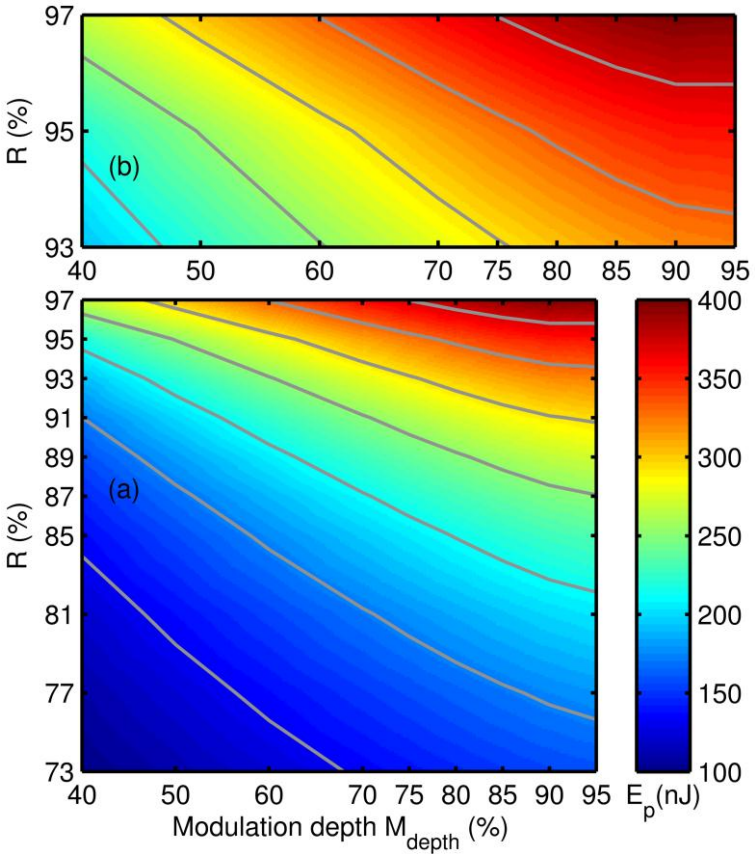

Figure 6.5. (a) Cavity-dumped pulse energy dependence on cavity reflectivity and modulation depth. The maximum Energy, available with 15 roundtrips was 432.8 nJ. (b) A close-up into the last four per cent of cavity reflectivity.

However, increasing the reflectivity to 97% returned a maximum extractable energy of 1120 nJ with a dumping modulation of 95%. In Figure 6.4(b) the transition into the dumping-dominated regime is occurring for the lowest rate at about 5% intrinsic losses. At low dumping rates, the final 2% in loss reduction provided an increase of energy of 500 nJ.

Presented in Figure 6.5 are cavity-dumped pulse energies available at 15 roundtrips with a variation of cavity reflectivity against modulation depth. The isoenergy lines particularly in the region of lower losses are nearly straight lines. The isoline of identical energy taken in the yellow area (about 2/3 of the maximum) returned a gradient of $\Delta M_{depth}/\Delta R = 91 - 97/95 - 40 = -0.11$. Hence, a decrease of the cavity losses by 1% is equal to an increase in modulation efficiency by a factor 9.2. Therefore, even at comparatively high dumping rates the cavity losses are a significant influence.

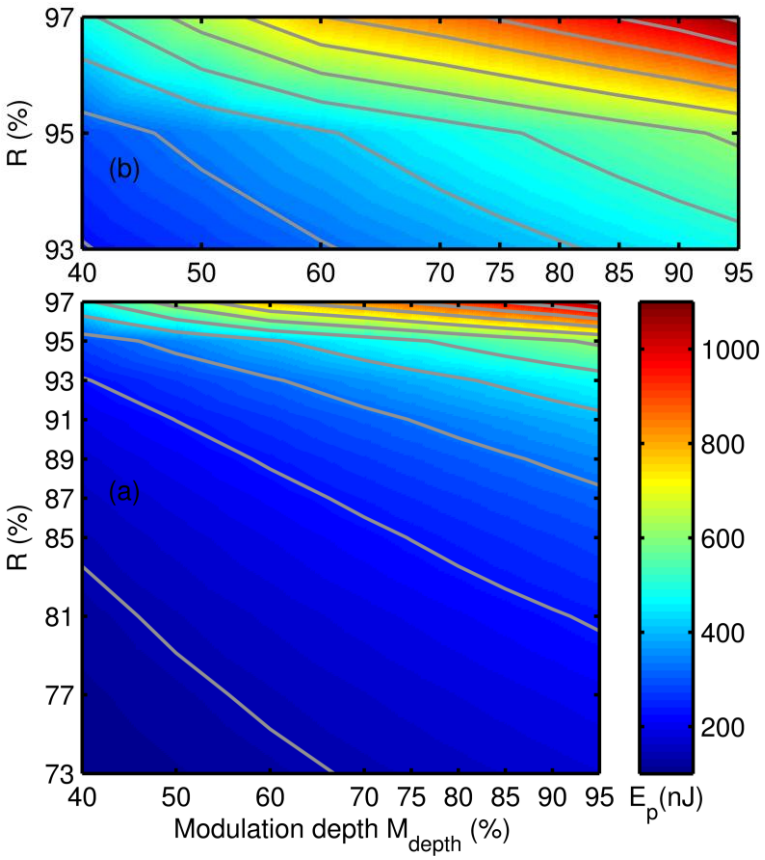

Figure 6.6. (a) Cavity-dumped pulse energy depending on cavity reflectivity and modulation depth. The maximum Energy, available with 108 roundtrips was 1120 nJ. (b) A close-up into the last four per cent of cavity reflectivity.

We repeated the previous analysis with a cavity-dumping cycle of 108 roundtrips. As with the previous graph, in Figure 6.6 we have taken again the gradient of the iso-energy-line in the yellow section returning a gradient of $\Delta M_{depth}/\Delta R = 95 - 97/95 - 50 = -0.044$. As expected, the effect is more severe and a decrease of the cavity losses by 1% in this region equals an increase in modulation efficiency by a factor 22.5 showing a vast dominance of cavity losses over dumper efficiency.

The output of the OPO is comprised by strong components at its signal wavelength and weaker idler and DFG wavelengths. An insight into the origin of these outputs is given by Figure 6.7, which presents a logarithmic plot of the spectral evolution of the field in the OPO crystal once steady-state has been reached. Inside the crystal, the pump pulse is visible at 1060 nm, converted into a strong signal pulse at 1.5 µm and an idler pulse at 3.61 µm as well as the DFG between signal and idler at 2.56 µm. Weak second-harmonic traces of the idler (1.8 µm) and of the frequency-doubled DFG at 1.28 µm are visible too.

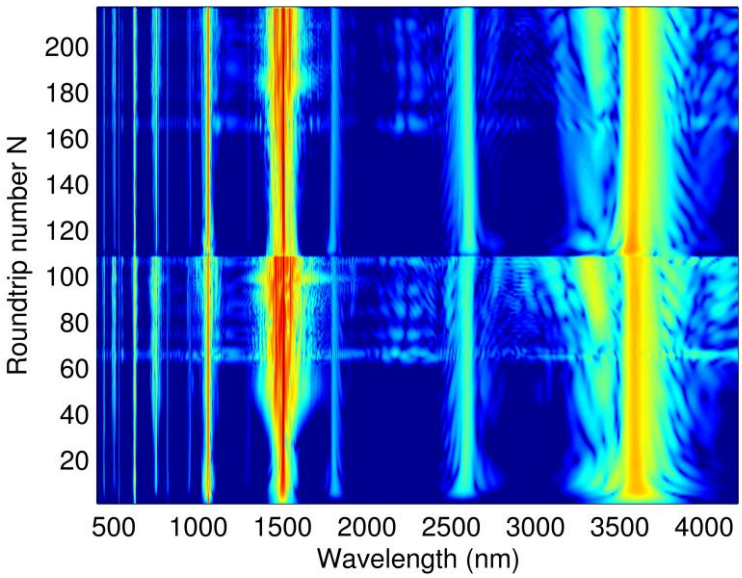

Figure 6.7. Intracavity spectrum of the cavity-dumped OPO, where the spectral density is expressed with a logarithmic colour scale, showing the evolution of the signal pulse, centred at 1.5 µm until it is dumped after 108 roundtrips.

6.5 Conclusions

Due to the good agreement between the underling model and experimental results shown in a previous simulation [92], we are confident that the presented results are reliable. Furthermore, the simulated energies are in good agreement with results

reported from an experiment which used the output of a transform limited Ti:sapphire source with a pulse energy of 9.8 nJ to pump a cavity-dumped OPO and extract 80 nJ pulses in the single pump arrangement [11]. The experimental results correspond to a pump-to-extraction pulse energy ratio of 8.2, where we showed with our simulation that under ideal conditions (assuming only 3% intrinsic losses and a modulation depth of 95%) extraction ratios up to a factor 11 are feasible.

We found that at low dumping rates (long build-up) the extraction is solely cavity-loss-dominated, where in contrast to at high dumping rates the regime for energy extraction is modulator dominated. The results suggest that the limit of maximum extractable energy is greatly dictated by the intrinsic cavity losses and only minor effects are contributed by the dumping efficiency. The design of a system, targeted for maximum energy extraction, should therefore be focused on minimizing the intrinsic losses.

A comparison of experimental and simulated results between cavity-dumped ultrafast laser systems [82,86] and ultrafast optical parametric oscillators [10,11,85] reveals that OPOs do not suffer from the instabilities which are intrinsic in lasers due to the disturbance of their modelocking performance. Therefore, pulse extraction from inside an OPO is far more flexible in terms of dumping rates and modulation depth. In addition, one of the main advantages of OPOs, their tunability, remains unaffected by cavity-dumping [11].

Chapter 7 - Outlook and conclusions

7.1 Summary

A high-energy extended-cavity MgO:PPLN optical parametric oscillator, synchronously pumped by a femtosecond Yb:fibre laser was demonstrated in Chapter 3. The oscillator operated at a signal wavelength of 1530 nm with a repetition-frequency of 15.3 MHz, which was achieved by using intracavity relay-imaging optics. With 1.0 W average power for the extracted signal pulses and durations of around 1.5 ps and energies greater than 70 nJ, this produced the highest directly output coupled pulse energy from an OPO at this time. A novel aspect of the OPO is the incorporation of relay imaging, enabling a stable resonator with very low repetition rates, which opens up the use of very high pump pulse energies for energy and power scaling.

In Chapter 4 an intermediate step was taken where a formal approach for wavelength-stabilisation of OPOs was presented. By introducing a valid model of all the components present in the feedback loop, experimentally obtained responses were understood and explained. The presented results showed a 40-fold improvement in wavelength stabilisation as well as a 2-fold improvement of power fluctuations, mainly limited by the existing pump noise.

The combination of the pump-source and the cavity design presented in Chapter 3, and the stabilisation-technique of Chapter 4, were the basis for a re-design of the OPO cavity introduced in Chapter 5. The design was altered to implement efficient cavity-dumping based on a TeO_2 acousto-optic modulator.

Sub-250-fs pulses with energies of up to 650 nJ and peak powers up to 2.07 MW were generated from a cavity-dumped optical parametric oscillator, synchronously pumped at 15.3 MHz with sub-400-fs pulses from a commercial Yb:fibre laser. The system maintained pulse energies ≥ 392 nJ and peak powers ≥ 1.3 MW over a repetition range from 101 kHz – 3.06 MHz. The average beam quality factor of the dumped output was $M^2 \sim 1.2$ and the total relative-intensity noise was 8 mdBc[2], making the system a promising ultrafast laser source for the scientific applications given in the introduction.

In Chapter 6 cavity-dumping dynamics where numerically investigated and showed good agreement between the simulated results and the results reported from an experiment which used the output of a transform limited Ti:sapphire source [11]. We demonstrated with our simulation that under ideal conditions with only 3% intrinsic losses and a modulation depth of 95%, energy extraction ratios up to a factor 11 are feasible.

We found that at low dumping rates (long build-up) the extraction is solely cavity-loss-dominated, where in contrast to at high dumping rates the regime for energy extraction is modulator dominated. The results suggest that the limit of maximum extractable energy is greatly dictated by the intrinsic cavity losses and only minor effects are contributed by the dumping efficiency. The design of a system, targeted for maximum energy extraction, should therefore be focused on minimizing the intrinsic losses.

7.2 Future Outlook

With the experience gathered during the development of the presented system, a follow-on project was motivated in order to extract even higher energies at higher repetition rates. To achieve this we must overcome the rather low pump conversion efficiency which we found was mainly caused by the pure spectral and temporal output shape of the Yb:fibre laser. Therefore, the design a modelocked Yb:KYW pump will be investigated to produce transform limited pulses with at 20 MHz repetition rate and pulse energies >500nJ. The output of the pump will be used to synchronously pump a cavity-dumped ring OPO. The move to a ring OPO reduces the losses introduce per roundtrip by a factor of two. The combination of reduced cavity losses and the transform limited pump pulses make the extraction of 1 µJ pulses at about 500 kHz and below possible.

7.3 Conclusions

The presented system was able to advance deep into the performance gap outlined in the introduction. This is shown by the red dots in Figure 7.1 representing the results from the cavity-dumped system.

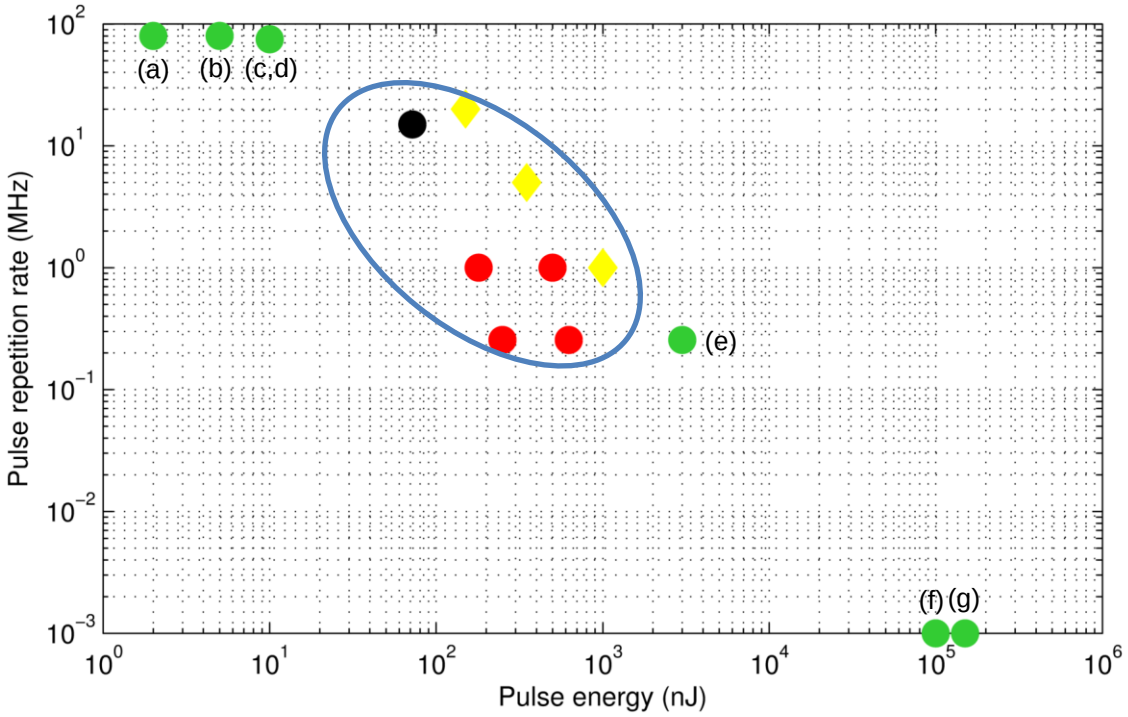

Figure 7.1. Shows the existing gap between low-energy, high-repetition-rate OPOs and high-energy, low-repetition-rate optical parametric amplifiers OPAs. The green markers correspond to: (a) [1], (b) [2], (c) [3], (d) [4], (e) [5], (f) [6], (g) [7]. The black dot shows the direct output coupled enrgy obtained in chapter 3. The red dots show the energies extracted with the cavity dumped OPO presented in chapter 5. The yellow markers represent the target for the next generation cavity-dumped ring OPO.

The simple cavity layout, the presented power and wavelength stabilities and the intrinsic tunability of the system represent a very powerful candidate for demanding high-energy ultrafast applications like optical waveguide writing, free-space spectroscopy for environmental monitoring and chemical detection, 3D ranging, multiphoton imaging, nonlinear spectroscopy, as well as for various medical applications. In this thesis we showed it is possible to overcome the present energy limitations associated with synchronously pumped ultrafast OPOs by demonstrating an increase in pulse energy over existing ultrafast OPOs by a factor of more than 400 times while providing a scientifically and commercially attractive solution with the potential to fill the existing performance gap.

References

1. Radiantis, "OPIUM," (2009).
2. S. Physics, "OPAL," (2009).
3. Coherent, "Mira-OPO," (2009).
4. APE, "APE-OPO," (2009).
5. Coherent, "RegA," (2009).
6. S. Physics, "OPA-800C," (2009).
7. Coherent, "TOPAS-800-FS," (2009).
8. T. Südmeyer, E. Innerhofer, F. Brunner, R. Paschotta, T. Usami, H. Ito, S. Kurimura, K. Kitamura, D. Hanna, and U. Keller, "High-power femtosecond fiber-feedback optical parametric oscillator based on periodically poled stoichiometric LiTaO_3," Optics Letters **29**, 1111-1113 (2004).
9. F. Kienle, P. Siong Teh, S. U. Alam, C. B. E. Gawith, D. C. Hanna, D. J. Richardson, and D. P. Shepherd, "Compact, high-pulse-energy, picosecond optical parametric oscillator," Optics Letters **35**, 3580-3582 (2010).
10. E. O. Potma, W. P. de Boeij, M. S. Pshenichnikov, and D. A. Wiersma, "30-fs, cavity-dumped optical parametric oscillator," Optics Letters **23**, 1763-1765 (1998).
11. C. K. Min and T. Joo, "Near-infrared cavity-dumped femtosecond optical parametric oscillator," Optics Letters **30**, 1855-1857 (2005).
12. C. B. Schaffer, A. Brodeur, J. F. García, and E. Mazur, "Micromachining bulk glass by use of femtosecond laser pulses with nanojoule energy," Optics Letters **26**, 93-95 (2001).
13. E. Wachman, D. Edelstein, and C. Tang, "Continuous-wave mode-locked and dispersion-compensated femtosecond optical parametric oscillator," Optics Letters **15**, 136-138 (1990).
14. R. W. Boyd, *Nonlinear Optics*, 3rd ed. (Academic Press, 2008).
15. A. Yariv, *Quantum Electronics*, 3rd ed. (John Wiley & Sons, 1988).
16. D. T. Reid, *Nonlinear Optics and Modulators* (Heriot-Watt University lecture notes, 2011).
17. R. Fork, O. Martinez, and J. Gordon, "Negative dispersion using pairs of prisms," Optics Letters **9**, 150-152 (1984).

18. E. Treacy, "Compression of picosecond light pulses," Physics Letters A **28**, 34-35 (1968).

19. E. Treacy, "Optical pulse compression with diffraction gratings," Quantum Electronics, IEEE Journal of **5**, 454-458 (1969).

20. M. Yamashita, M. Ishikawa, K. Torizuka, and T. Sato, "Femtosecond-pulse laser chirp compensated by cavity-mirror dispersion," Optics letters **11**, 504-506 (1986).

21. R. Szipöcs, K. Ferencz, C. Spielmann, and F. Krausz, "Chirped multilayer coatings for broadband dispersion control in femtosecond lasers," Optics Letters **19**, 201-203 (1994).

22. P. T. F. Gires, "Interféromètre utilisable pour la compression d'impulsions lumineuses modulés en fréquence," C. R. Acad. Sci. Paris **258**, 6112 (1964).

23. J. C. M. Diels, J. J. Fontaine, I. C. McMichael, and F. Simoni, "Control and measurement of ultrashort pulse shapes (in amplitude and phase) with femtosecond accuracy," Applied Optics **24**, 1270-1282 (1985).

24. S. M. Eaton, H. Zhang, M. L. Ng, J. Li, W. J. Chen, S. Ho, and P. R. Herman, "Transition from thermal diffusion to heat accumulation in high repetition rate femtosecond laser writing of buried optical waveguides," Optics Express **16**, 9443-9458 (2008).

25. A. Killi, U. Morgner, M. Lederer, and D. Kopf, "Diode-pumped femtosecond laser oscillator with cavity dumping.," Optics Letters **29**, 1288 (2004).

26. S. Cho, B. Bouma, E. Ippen, and J. Fujimoto, "Low-repetition-rate high-peak-power Kerr-lens mode-locked Ti:Al_2O_3 laser with a multiple-pass cavity," Optics Letters **24**, 417-419 (1999).

27. S. Cho, F. Kärtner, U. Morgner, E. Ippen, J. Fujimoto, J. Cunningham, and W. Knox, "Generation of 90-nJ pulses with a 4-MHz repetition-rate Kerr-lens mode-locked Ti:Al_2O_3 laser operating with net positive and negative intracavity dispersion," Optics Letters **26**, 560-562 (2001).

28. V. Shcheslavskiy, V. Yakovlev, and A. Ivanov, "High-energy self-starting femtosecond Cr^{4+}: Mg_2SiO_4 oscillator operating at a low repetition rate," Optics Letters **26**, 1999-2001 (2001).

29. D. N. Papadopoulos, M. Delaigue, F. Druon, F. Balembois, P. Georges, and others, "Passively mode-locked diode-pumped Nd: YVO_4 oscillator operating at an ultralow repetition rate," Optics Letters **28**, 1838-1840 (2003).

30. M. O'Connor, M. Watson, D. Shepherd, D. Hanna, J. Price, A. Malinowski, J. Nilsson, N. Broderick, D. Richardson, and L. Lefort, "Synchronously pumped optical parametric oscillator driven by a femtosecond mode-locked fiber laser," Optics Letters **27**, 1052-1054 (2002).

31. J. Kim, P. Dupriez, D. Soh, J. Nilsson, and J. Sahu, "Core area scaling of Nd:Al-doped silica depressed clad hollow optical fiber and Q-switched laser operation at

0.9 μm," Optics Letters **31**, 2833-2835 (2006).

32. J. Kim, P. Dupriez, C. Codemard, J. Nilsson, and J. Sahu, "Suppression of stimulated Raman scattering in a high power Yb-doped fiber amplifier using a W-type core with fundamental mode cut-off," Optics Express **14**, 5103-5113 (2006).

33. D. Reid, W. Sibbett, J. Dudley, L. Barry, B. Thomsen, and J. Harvey, "Commercial semiconductor devices for two photon absorption autocorrelation of ultrashort light pulses," Applied optics **37**, 8142-8144 (1998).

34. G. Boyd and D. Kleinman, "Parametric interaction of focused Gaussian light beams," Journal of Applied Physics **39**, 3597-3639 (1968).

35. W. W. Rigrod, "Saturation Effects in High-Gain Lasers," Journal of Applied Physics **36**, 2487-2490 (1965).

36. A. E. Siegman, *Lasers* (University Science Books, 1986).

37. J. C. Lagarias, J. A. Reeds, M. H. Wright, and P. E. Wright, "Convergence properties of the Nelder-Mead simplex method in low dimensions," SIAM Journal of Optimization **9**, 112-147 (1998).

38. D. Butterworth, S. Girard, and D. Hanna, "A simple technique to achieve active cavity-length stabilisation in a synchronously pumped optical parametric oscillator," Optics communications **123**, 577-582 (1996).

39. G. Baxter, M. Payne, B. Austin, C. Halloway, J. Haub, Y. He, A. Milce, J. Nibler, and B. Orr, "Spectroscopic diagnostics of chemical processes: applications of tunable optical parametric oscillators," Applied Physics B: Lasers and Optics **71**, 651-663 (2000).

40. A. Zumbusch, G. R. Holtom, and X. S. Xie, "Three-dimensional vibrational imaging by coherent anti-Stokes Raman scattering," Physical Review Letters **82**, 4142-4145 (1999).

41. G. Ehret, A. Fix, V. Weiss, G. Poberaj, and T. Baumert, "Diode-laser-seeded optical parametric oscillator for airborne water vapor DIAL application in the upper troposphere and lower stratosphere," Applied Physics B: Lasers and Optics **67**, 427-431 (1998).

42. Y. Barad, H. Eisenberg, M. Horowitz, and Y. Silberberg, "Nonlinear scanning laser microscopy by third harmonic generation," Applied Physics Letters **70**, 922 (1997).

43. M. Dinu, F. Quochi, and H. Garcia, "Third-order nonlinearities in silicon at telecom wavelengths," Applied Physics Letters **82**, 2954-2956 (2003).

44. M. Rodwell, K. Weingarten, D. Bloom, T. Baer, and B. Kolner, "Reduction of timing fluctuations in a mode-locked Nd: YAG laser by electronic feedback," Optics Letters **11**, 638-640 (1986).

45. M. J. W. Rodwell, D. M. Bloom, and K. J. Weingarten, "Subpicosecond laser timing stabilization," Quantum Electronics, IEEE Journal of **25**, 817-827 (1989).

46. G. Kennedy, R. Grant, W. E. Sleat, and W. Sibbett, "Amplitude noise reduction of a coupled-cavity mode-locked NaCl:OH^- color-center laser by active synchronization," Optics Letters **18**, 208-210 (1993).

47. J. Chesnoy and L. Fini, "Stabilization of a femtosecond dye laser synchronously pumped by a frequency-doubled mode-locked YAG laser," Optics Letters **11**, 635-637 (1986).

48. M. D. Dawson, D. Maxson, T. F. Boggess, and A. L. Smirl, "Cavity-length detuning effects and stabilization of a synchronously pumped femtosecond linear dye laser," Optics Letters **13**, 126-128 (1988).

49. H. Photonics, "Hamamatsu Photonics, One-dimensional PSD (S3932), http://jp.hamamatsu.com/products/division/ssd/pd123/pd124/S3932/index_en.html ," (2009).

50. D. Reid, Z. Penman, M. Ebrahimzadeh, W. Sibbett, H. Karlsson, and F. Laurell, "Broadly tunable infrared femtosecond optical parametric oscillator based on periodically poled $RbTiOAsO_4$," Optics Letters **22**, 1397-1399 (1997).

51. ANSI/IEEE, "Std 176-1987, 176th ed.," (1988).

52. A. J. Stubberud, I. J. Williams, and J. J. Distefano, *Schaum's Outline of Feedback and Control Systems, Second Edition (Schaum's Outline Series)*, 2nd ed. (Schaum's Outlines, 1995).

53. P. Gascoyne and H. Rutt, "An opto-acoustic frequency lock system for pulsed lasers," Journal of Physics E: Scientific Instruments **16**, 31 (1983).

54. K. Vodopyanov, W. Hurlbut, and V. Kozlov, "Photonic THz generation in GaAs via resonantly enhanced intracavity multispectral mixing," Applied Physics Letters **99**, 041104 (2011).

55. J. E. Schaar, J. S. Pelc, K. L. Vodopyanov, and M. M. Fejer, "Characterization and control of pulse shapes in a doubly resonant synchronously pumped optical parametric oscillator," Applied optics **49**, 4489-4493 (2010).

56. J. Schaar, K. Vodopyanov, and M. Fejer, "Intracavity terahertz-wave generation in a synchronously pumped optical parametric oscillator using quasi-phase-matched GaAs," Optics Letters **32**, 1284-1286 (2007).

57. T. I. Ferreiro, J. Sun, and D. T. Reid, "Frequency stability of a femtosecond optical parametric oscillator frequency comb," Optics Express **19**, 24159-24164 (2011).

58. "For example: High-Q Laser, femtoNOVA^{TM} SC-1040-500 product," (n.d.).

59. "For example: IMRA, FCPA μJewel product, and Fianium, High-Energy HE1060-fs products," (n.d.).

60. A. H. Nejadmalayeri, P. R. Herman, J. Burghoff, M. Will, S. Nolte, and A. Tünnermann, "Inscription of optical waveguides in crystalline silicon by mid-infrared femtosecond laser pulses," Optics Letters **30**, 964-966 (2005).

61. Goutzoulis, *Design and Fabrication of Acousto-optic Devices (Optical Engineering)*, 1st ed. (CRC Press, 1994).

62. C. Raman and N. S. N. Nath, "The diffraction of light by high frequency sound waves: Part I. ," Proceedings of the Indian Academy of Sciences, Section A **2**, 406-412 (1935).

63. C. Raman and N. S. N. Nath, "The diffraction of light by high frequency sound waves: Part II.," Proceedings of the Indian Academy of Sciences **2**, 413-465 (1935).

64. W. Klein and B. D. Cook, "Unified approach to ultrasonic light diffraction," Sonics and Ultrasonics, IEEE Transactions on **14**, 123-134 (1967).

65. J. D. Ward, "The Design of Pigtailed Acousto-Optic Modulators and Frequency-Shifters, GOOCH & HOUSEGO PLC," (2011).

66. "TeO_2 material constants: http://www.sciner.com/Acousto-Optics/TeO2.htm," (2004).

67. P. E. Ciddor, "Refractive index of air: new equations for the visible and near infrared," Applied Optics **35**, 1566-1573 (1996).

68. O. Paul, A. Quosig, T. Bauer, M. Nittmann, J. Bartschke, G. Anstett, and J. L'huillier, "Temperature-dependent Sellmeier equation in the MIR for the extraordinary refractive index of 5% MgO doped congruent $LiNbO_3$," Applied Physics B: Lasers and Optics **86**, 111-115 (2007).

69. W. Martienssen and H. Warlimont, *Springer Handbook of Condensed Matter and Materials Data*, Har/Cdr (Springer, 2005).

70. SCHOTT_AG, "Sellmeier coefficients for refractive index calculation from "schott_optical_glass_catalogue_excel_2009.xls," (2009).

71. E. Hecht, *Optics (International Edition)*, 4th ed. (Pearson, 2003).

72. S. D. Lord, "Technical Memorandum 103957, NASA," (1992).

73. M. C. Simon and P. A. Larocca, "Minimum deviation for uniaxial prisms," Applied optics **34**, 709-715 (1995).

74. P. Bélanger, "Beam propagation and the ABCD ray matrices," Optics Letters **16**, 196-198 (1991).

75. G. Gibson, R. Klank, F. Gibson, and B. Bouma, "Electro-optically cavity-dumped ultrashort-pulse Ti:sapphire oscillator," Optics Letters **21**, 1055-1057 (1996).

76. A. Baltuška, Z. Wei, M. S. Pshenichnikov, D. A. Wiersma, and R. Szipőcs, "All-solid-state cavity-dumped sub-5-fs laser," Applied Physics B: Lasers and Optics **65**, 175-188 (1997).

77. A. Killi, A. Steinmann, J. Dörring, U. Morgner, M. J. Lederer, D. Kopf, and C. Fallnich, "High-peak-power pulses from a cavity-dumped Yb:$KY(WO_4)_2$ oscillator," Optics Letters **30**, 1891-1893 (2005).

78. U. Demirbas, K. H. Hong, J. G. Fujimoto, A. Sennaroglu, and F. X. Kärtner, "Low-cost cavity-dumped femtosecond Cr:LiSAF laser producing >100 nJ pulses," Optics Letters **35**, 607-609 (2010).

79. M. Ramaswamy, M. Ulman, J. Paye, and J. Fujimoto, "Cavity-dumped femtosecond Kerr-lens mode-locked Ti:Al_2O_3 laser," Optics Letters **18**, 1822-1824 (1993).

80. M. S. Pshenichnikov, W. P. de Boeij, and D. A. Wiersma, "Generation of 13-fs, 5-MW pulses from a cavity-dumped Ti:sapphire laser," Optics Letters **19**, 572-574 (1994).

81. G. Palmer, M. Emons, M. Siegel, A. Steinmann, M. Schultze, M. Lederer, and U. Morgner, "Passively mode-locked and cavity-dumped Yb: $KY(WO_4)_2$ oscillator with positive dispersion," Optics Express **15**, 16017-16021 (2007).

82. G. Palmer, M. Siegel, A. Steinmann, and U. Morgner, "Microjoule pulses from a passively mode-locked Yb:KY $(WO_4)_2$ thin-disk oscillator with cavity dumping," Optics Letters **32**, 1593-1595 (2007).

83. Y. Nagasawa, Y. Ando, A. Watanabe, and T. Okada, "Generation of 30 fs pulses at 635 nm by frequency doubling of cavity-dumped chromium-doped forsterite laser, and its application to spectroscopy," Applied Physics B: Lasers and Optics **70**, 33-36 (2000).

84. U. Wegner, J. Meier, and M. Lederer, "Compact picosecond mode-locked and cavity-dumped Nd:YVO_4 laser," Optics Express **17**, 23098-23103 (2009).

85. T. Lamour and D. Reid, "650-nJ pulses from a cavity-dumped Yb: fiber-pumped ultrafast optical parametric oscillator.," Optics Express **19**, 17557-62 (2011).

86. A. Killi and U. Morgner, "Solitary pulse shaping dynamics in cavity-dumped laser oscillators," Opt. Express **12**, 3397-3407 (2004).

87. B. Sevruk, "Numerical Modeling of an Optical Parametric Oscillator in the Cavity-Dumping Mode," Journal of Applied Spectroscopy **68**, 101-109 (2001).

88. J. Armstrong, N. Bloembergen, J. Ducuing, and P. Pershan, "Interactions between light waves in a nonlinear dielectric," Physical Review **127**, 1918 (1962).

89. M. Becker, D. Kuizenga, D. Phillion, and A. Siegman, "Analytic expressions for ultrashort pulse generation in mode-locked optical parametric oscillators," Journal of Applied Physics **45**, 3996-4005 (1974).

90. E. Cheung and J. Liu, "Theory of a synchronously pumped optical parametric oscillator in steady-state operation," J. Opt. Soc. Am. B **7**, 1385-1401 (1990).

91. K. A. Tillman, D. T. Reid, D. Artigas, and T. Jiang, "Idler-resonant femtosecond tandem optical parametric oscillator tuning from 2.1 μm to 4.2 μm," JOSA B **21**, 1551-1558 (2004).

92. D. T. Reid, "Ultra-broadband pulse evolution in optical parametric oscillators," Optics Express **19**, 17979-17984 (2011).

93. M. Conforti, F. Baronio, and C. De Angelis, "Nonlinear envelope equation for broadband optical pulses in quadratic media," Physical Review A **81**, 053841 (2010).

94. W. H. Press, S. A. Teukolsky, W. T. Vetterling, and B. P. Flannery, *Numerical Recipes 3rd Edition: The Art of Scientific Computing*, 3rd ed. (Cambridge University Press, 2007).

95. G. Agrawal, *Nonlinear Fiber Optics (Optics and Photonics)*, 4th ed. (Academic Press, 2006).